Matthias Gritzner, BSc

# Femtosecond Velocity Map Imaging of Iodine Dynamics in a Quantum Solvent

**MASTER'S THESIS**

to achieve the university degree of

Diplom-Ingenieur

Master's degree programme: Technical Physics

submitted to

**Graz University of Technology**

**Supervisor**

Assoc.Prof. Dipl.-Ing. Dr.Techn. Markus Koch

Institute of Experimental Physics

Graz, May 2023

## AFFIDAVIT

I declare that I have authored this thesis independently, that I have not used other than the declared sources/resources, and that I have explicitly indicated all material which has been quoted either literally or by content from the sources used. The text document uploaded to TUGRAZonline is identical to the present master's thesis.

24.05.2023,

Date, Signature

# Abstract

The use of ultrafast laser techniques, specifically pump-probe spectroscopy employing femtosecond laser pulses, enables the observation of chemical reactions on their natural timescales. When combined with superfluid helium nanodroplets as a spectroscopy matrix, the observation of reactions in aggregates which are often not accessible with other techniques becomes possible. While the superfluid helium environment seems to have little impact on nuclear dynamics, its effect on electronic processes remains unexplored. This study investigates the photoexcitation dynamics of molecular iodine ($I_2$) in superfluid helium nanodroplets, revealing the predissociation of the B-state due to internal conversion to a dissociative state. This has been observed before for $I_2$ in other solvents and attributed to solvent-iodine collisions, the molecule is thus a good candidate to study the influence of the helium environment on electronic dynamics. To track the dissociation fragments, a velocity map imaging (VMI) spectrometer was integrated into the existing setup, and its operation was verified by measuring the ions generated by photodissociation from the A-state of the iodine molecule. In gas phase, the molecule dissociates within 1 ps, showing no dynamics for larger timedelays between pump and probe. Molecules inside helium droplets show photodissociation dynamics between 5 and 300 ps due to different internuclear separations upon Coulomb explosion by the probe pulse. The observed ion velocities are higher than for effusive molecules - leading to the conclusion that the fragments are spatially confined in the droplets for longer times, which leads to higher Coulomb energies. When solvated inside helium nanodroplets, immediate fragmentation of $I_2$ molecules in the B-state is observed. This is in strong contrast to the B-state dynamics in the gas phase, where no sign of decay on picosecond timescales could be observed, therefore revealing a strong influence from the principally low-interacting helium environment. The generated ions appear at higher velocities when compared to the A-state measurements, stemming from a higher initial velocity due to the initial starting point in the electronic potential. Further measurements with the Velocity Map Imaging spectrometer will deepen the understanding of electron dynamics in the quantum solvent and the exact process of predissociation of the iodine molecule in superfluid helium nanodroplets.

# Kurzfassung

Der Einsatz ultraschneller Lasertechniken, insbesondere der Pump-Probe-Spektroskopie mit Femtosekunden-Laserpulsen, ermöglicht die Beobachtung chemischer Reaktionen in ihren natürlichen Zeitskalen. In Kombination mit supraflüssigen Helium-Nanotröpfchen als Spektroskopiematrix wird die Beobachtung von Reaktionen in Aggregaten möglich, die mit anderen Techniken oft nicht zugänglich sind. Während die supraflüssige Heliumumgebung nur geringe Auswirkungen auf die Kerndynamik zu haben scheint, sind ihre Auswirkungen auf elektronische Prozesse noch unerforscht. In dieser Studie wird die Photoanregungsdynamik von molekularem Iod ($I_2$) in suprafluiden Helium-Nanotröpfchen untersucht, im Speziellen die Prädissoziation des B-Zustands aufgrund einer internen Umwandlung in einen dissoziativen Zustand. Dies wurde bereits für $I_2$ in anderen Lösungsmitteln beobachtet und auf Kollisionen zwischen dem Lösungsmittel und dem Molekül zurückgeführt. Daher ist $I_2$ ein guter Kandidat für die Untersuchung des Einflusses der Heliumumgebung auf elektronische Dynamiken. Um die Dissoziationsfragmente zu detektieren, wurde ein Velocity Map Imaging (VMI) Spektrometer in den bestehenden Aufbau integriert und die Ionen-Detektion durch Messungen der Photodissoziation aus dem A-Zustand des Iodmoleküls verifiziert. In der Gasphase dissoziiert das Molekül im A-Zustand innerhalb von 1 ps und zeigt keine Dynamik bei größeren Zeitabständen zwischen Pump und Probe. Moleküle in Heliumtröpfchen zeigen eine Photodissoziationsdynamik zwischen 5 und 300 ps aufgrund unterschiedlicher Kernabstände bei der Coulomb-Explosion durch den Probe Puls. Die beobachteten Ionengeschwindigkeiten sind höher als bei effusiven Molekülen, was darauf schließen lässt, dass die Fragmente in den Tröpfchen räumlich länger eingeschlossen sind, was zu höheren Coulombenergien führt. Bei Anregung in den B-Zustand wird eine sofortige Fragmentierung der Moleküle beobachtet wenn sie in Helium-Nanotröpfchen gelöst werden. Dies steht in starkem Kontrast zur Dynamik des B-Zustands in der Gasphase, wo keine Anzeichen eines Zerfalls auf Pikosekunden-Zeitskalen beobachtet werden konnte, was auf einen starken Einfluss der Heliumumgebung hindeutet. Die erzeugten Ionen erscheinen im Vergleich zu den Messungen im A-Zustand mit höheren Geschwindigkeiten, was auf eine höhere Anfangsgeschwindigkeit aufgrund des anfänglichen Startpunkts im elektronischen Potential zurückzuführen ist. Weitere Messungen mit dem Velocity Map Imaging Spektrometer werden das Verständnis von Elektronendynamiken in suprafluiden Helium-Nanotropfen und des genauen Prozesses der Prädissoziation des Iodmoleküls vertiefen.

# Contents


**1 Introduction** **11**
- 1.1 Iodine states and pump-probe spectroscopy . . . 12
- 1.2 Gas phase . . . 13
- 1.3 Solution studies . . . 14
- 1.4 Superfluid helium droplets as cryomatrix . . . 17
- 1.5 Molecular dynamics in helium droplets . . . 18
  - 1.5.1 He solvation shell dynamics . . . 18
  - 1.5.2 $In_2$ wavepacket motion . . . 19
- 1.6 Indication for predissociation in superfluid helium nanodroplets . . . 20

**2 Experimental Setup** **23**
- 2.1 Optical setup and laser system . . . 23
  - 2.1.1 Laser characterization and focus optimization . . . 24
- 2.2 Vacuum setup . . . 27
- 2.3 Velocity map imaging spectrometer . . . 28
  - 2.3.1 Characterization of the detector . . . 31
  - 2.3.2 Energy calibration ion mode . . . 33
  - 2.3.3 Abel inversion . . . 35
  - 2.3.4 Energy calibration electron mode . . . 36
  - 2.3.5 VMI Parameters . . . 37
  - 2.3.6 Pump-probe experiments . . . 41

**3 Results** **43**
- 3.1 Isolated $I_2$ molecules . . . 43
  - 3.1.1 A-state photodissociation . . . 43
  - 3.1.2 B-state Coulomb peak shift . . . 47
  - 3.1.3 B-state electrons . . . 48
- 3.2 $I_2$ molecules inside helium nanodroplets . . . 49
  - 3.2.1 A-state photodissociation . . . 49
  - 3.2.2 B-state predissociation . . . 52
- 3.3 Comparison . . . 54
  - 3.3.1 A-state for $I_2$ molecules in gas phase and inside helium nanodroplets . . . 54
  - 3.3.2 A-state and B-state inside helium nanodroplets . . . 55

**4 Discussion** **57**
- 4.1 Isolated $I_2$ molecules . . . 57
- 4.2 $I_2$ molecules in helium nanodroplets . . . 58

**5 Conclusion** **61**
- 5.1 Outlook . . . 61

**6 Appendix** **63**
- 6.1 Iodine pickup conditions . . . 63
- 6.2 B state coulomb peak shift . . . 64
- 6.3 B state electrons . . . 65

6.4 VMI goldplating . . . . . 67

# 1 Introduction

Photochemistry governs the world around us, it is the basis of photosynthesis, and as far as we know influenced, if not caused the origin of life itself. With the sun as the central power source in the solar system molecules like water, ammonia, methane, and carbon dioxide could have reacted photochemically to form complex organic molecules - the building blocks of life. [1] The dynamics of chemical bonds take place on the femtosecond timescale and have eluded researchers for decades since the necessary time resolution was not available. The development of ultrafast laser techniques essentially allowed to freeze time at the molecular scale and probe the dynamics that dictate so many processes that shape the world as we know it, and ultimately resulted in the Nobel Price in Chemistry for Ahmed Zewail who pioneered this new branch of femtosecond spectroscopy.[2]
Since then ultrafast laser techniques have been integrated into many different areas of research and opened up completely new possibilities. The combination with Scanning Tunneling Microscopy (STM) allows imaging with nanometer spatial resolution and subpicosecond time resolution and further shortening of laser pulses to the attosecond regime offers glimpses into electron movement and even made the mapping of $N_2$ molecular orbitals possible. [3, 4]
A tool to transition from gas phase studies to isolated atoms, molecules, radicals, and reactions are spectroscopy matrices. The suspension in a superfluid helium nanodroplet - which are transparent to electromagnetic radiation (up to 20 eV) and due to the superfluid state show little influence on species of interest, allows cryogenic matrix isolation at 0.38 K. They have been extensively studied and show promising capabilities for static as well as time-resolved spectroscopy. [5, 6, 7, 8] Experiments on microsolvation show new developments like the "smallest drop of acid".[9]
Being an ideal model system to study intramolecular perturbations of diatomic molecules the free iodine molecule $I_2$ serves as an ideal system to continue the time-resolved femtosecond studies of molecular dynamics in superfluid helium droplets and to further deepen our knowledge on the influence of the solvation environment. $I_2$ has been studied deeply in gas phase [10, 11] as well as in different solutions [12, 13, 14] What is more, the bound B-state of iodine exhibits a crossing with the potential surface of the unbound a-state - leading to the possibility of predissociation by internal conversion. In gas phase, the probability for this is extremely low, but in solution, collisions can induce electronic coupling and accelerate the depopulation of the excited state by magnitudes. Initial experiments in superfluid helium nanodroplets show evidence that a fast dissociation is induced as well, with the implication of the principally low-interacting environment interacting more with the solved particles as previously thought. In order to understand this, time-of-flight measurements are not sufficient, more information on the dissociation is necessary. To achieve this, a new Velocity Map Imaging (VMI) spectrometer was integrated into the existing setup, to allow for time-resolved ion spectroscopy via photofragment translational spectroscopy [15] and Coulomb explosion imaging [16]. Tracking the dissociated fragments then allows a far deeper insight into the dynamics of this process.

## 1.1 Iodine states and pump-probe spectroscopy

The $I_2$ molecule has been studied extensively both in gas phase [10, 11, 17] and in different solutions [12, 18, 14, 19, 20]. The electronic and vibrational structure is therefore very well known - as shown in figure 1.1. To gain insight into the molecular dynamics and decipher the different photochemical processes a pump-probe scheme [21] can be used. An initial spectrally broad pump pulse excites the molecule from the ground state X into an excited bound state B and generates a superposition of several vibrational states - a wavepacket (WP). The WP evolves in the excited state and disperses over time. After some time delay $\Delta$t, a second laser pulse (probe) supplies the system with enough energy to reach one of the ionic states and generates one or two ionized iodine atoms. By varying $\Delta$t a snapshot of each step of the dynamics can be taken and gives the evolution of the excited state population. The information being carried by the yield and kinetic energy of the ions and electrons $E_{kin}$:

$$E_{kin} = E_{photon} + E_t - IP \tag{1.1}$$

Where $E_{photon}$ is the energy of the probe photon (or the sum of the energies of several probe photons) $E_t$ is the energy of the excited state at a given time and IP is the ionization potential.

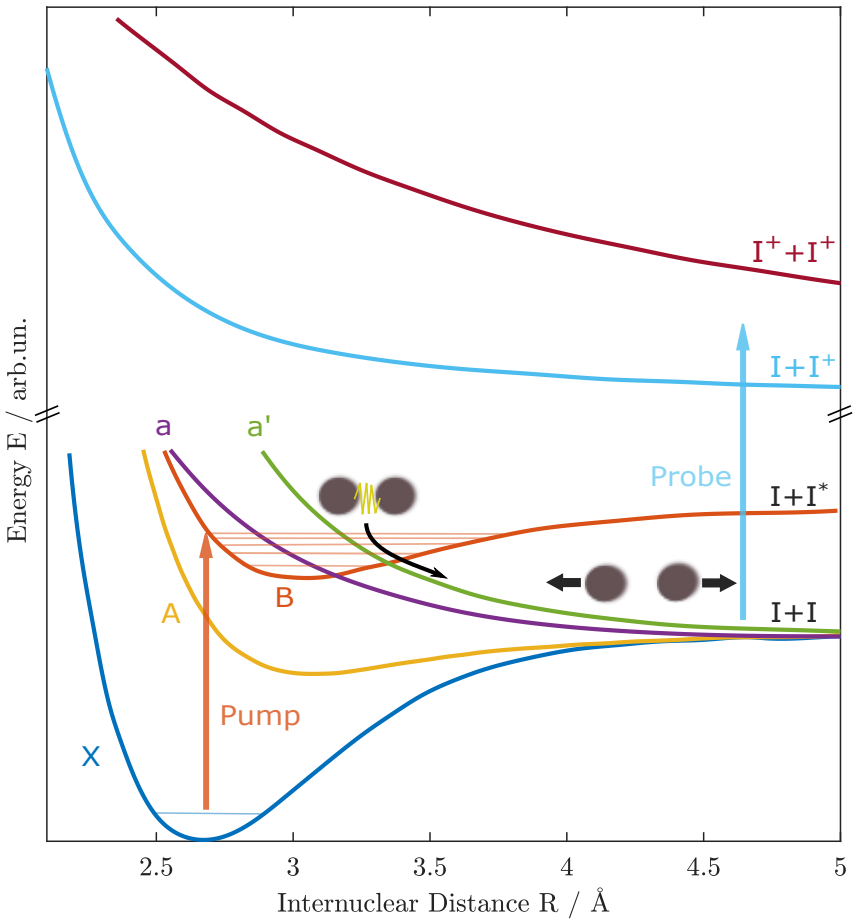


Figure 1.1: Relevant Electronic potentials of $I_2$ [22],[23] and schematic representation of a pump-probe experiment during predissociation. Possible process channel: A pump pulse excites the molecule from the ground state X to the excited bound state B, where a vibrational wavepacket (WP) evolves - and couples to the dissociative state a' which leads to predissociation of the molecule. After a time delay a second laser pulse (probe) ionizes the iodine atoms. Also shown are the weakly bound state A, the dissociative state a, and two ionic states.

As shown in figure 1.1, several dissociative states cross the bound B-state. Therefore a population of the B-state can internally convert to one of the other states. The quenching of the B-state via collision-induced predissociation with various collision partners M (M being a molecule that is not $I_2$ in its ground state X) follows the channel [22]:

$$I_2\,(B) \overset{M}{\rightarrow} I_2(RS) \rightarrow I\left(^2P_{3/2}\right) + I\left(^2P_{3/2}\right) \tag{1.2}$$

Where RS denotes a repulsive potential, very likely of gerade symmetry - therefore the predissociation occurs probably via either the a ($a1_g$) or the a' ($a'0_g^+$) states, resulting in two ground state iodine atoms. Also intersecting the B-state is C ($C1_u$), which is of ungerade symmetry and cannot be the cause for the predissociation because the Franck-Condon density of B-C does not match the measurements. [22]

## 1.2 Gas phase

Before delving into the dynamics of $I_2$ in various solutions, especially (superfluid) helium, it is important to note its properties in the gas phase. These have been studied very well, due to $I_2$ being an ideal model system for spectroscopic investigations of intramolecular perturbations of diatomic molecules. It exhibits many different ion-pair states, all with different properties and close-lying rovibronic levels. Accidental resonances between these dense energy levels lead to the possibility of studying perturbations. [22]

Especially the bound B-state has been the focus of various investigations, because of the possibility of preparing a WP which can disperse and revive in this potential well. The WP motion of gas phase iodine prepared in the B-state has been extensively studied by Bowman et al. Probe-induced fluorescence as a function of time delay between pump and probe showed long-lived oscillations with no sign of decay in the femtosecond timescale studied, although with a faster decaying envelope - which relates to the spread of WP. This is shown in figure 1.2.

When exciting into repulsive states below B rapid dissociation of the molecules - shown in an off-resonance behavior with decay to zero amplitude was detected. Lower pump wavelengths corresponding to excitation of the B-state above the dissociation limit gave a large signal followed by damped oscillations. [10]
The lifetimes of excitations into B in the gas phase are on the timescale of $\mu$s and play a negligible role in the femtosecond to picosecond timescales of the WP dynamics. [17, 11]

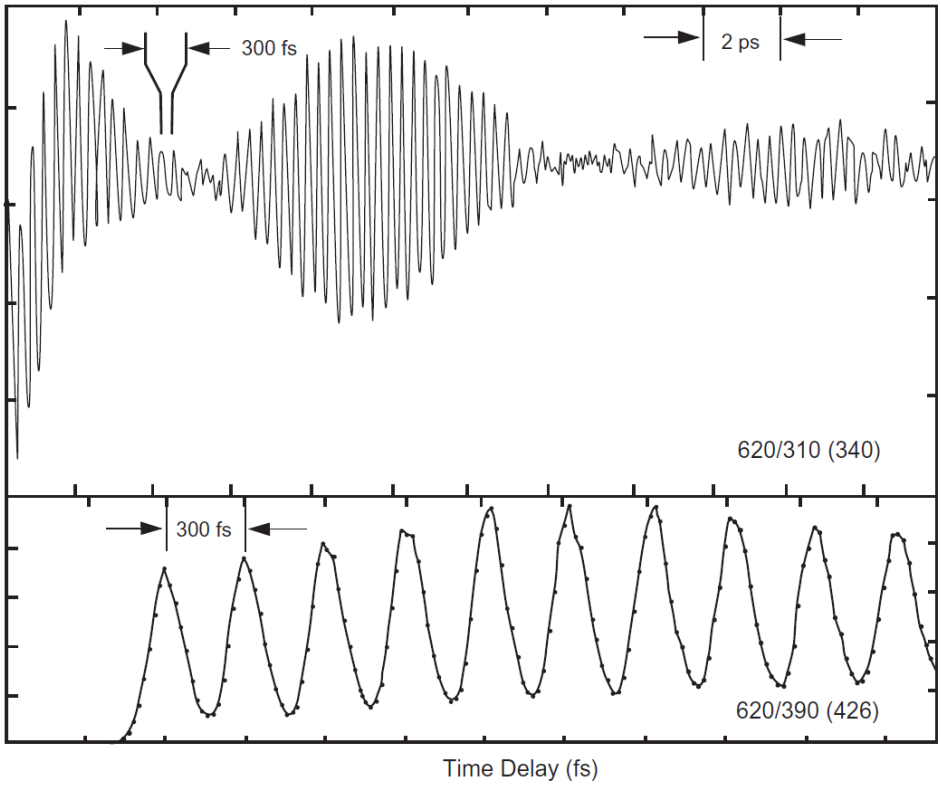


Figure 1.2: Femtosecond transition-state transients of $I_2$ in gas phase. Top: Pump wavelength 620 nm and probe wavelength 310 nm, showing oscillations on a large timescale with visible decay of the envelope. Bottom: pump wavelength 620 nm and probe wavelength 390 nm, smaller timescale depicting the individual WP oscillations with a period of 300 fs. [10]

## 1.3 Solution studies

In addition to understanding a molecule in the gas phase, the study of reactions and mechanisms in solvents is of course a topic of interest, especially because most chemical reactions take place in a solution environment. Here the collision of $I_2$ with solvent molecules can lead to the quenching effects caused by collision-induced predissociation. This can mean either dissociation of a van-der-Waals Cluster formed by the $I_2$ molecule and solvent atoms/molecules [24, 25, 26, 27, 28, 29] or dissociation of the $I_2$ molecule itself, which is the focus of this work.

**Theoretical approaches**
This can be first looked at theoretically [12]: Considering an excited state formed by an ultrashort excitation, one can assume a percentage P of the total population evolving on an excited potential surface, and the other 100-P % further evolves in the ground state. During vibration, excited molecules approach the crossing to a dissociative state (e.g. a or a'), and the coupling between B and the repulsive state dictated by the Franck-Conden overlap increases. This generates a population in a dissociative state which evolves with positive momentum to larger interatomic separation. The coupling then decreases to zero after the potential surface crossing due to the loss of Franck-Conden overlap. After some time the B-state molecules reverse the sign of their momentum, either by reaching the turning point of the potential or by a solvent atom preventing further stretching. The crossing is again approached and further predissociation is possible - leading to two predissociation events in every vibrational period, one during the stretch and one during contraction. Due to the non-centered position of the crossing and different atomic velocities, this is asymmetric in time.

Theoretical studies using a quantum mechanical hybrid strategy calculated the properties of two other diatomic molecules, namely $Cl_2$ and $Br_2$ in superfluid He nanodroplets of varying sizes. [19],[20] Similar to $I_2$, the excitation from the ground state to the bound state X of $Cl_2$ was studied. The excited molecule undergoes confinement by the He environment. Upon photodissociation of the $Cl_2$ molecule, confinement quantum interferences produce oscillations in the molecular wavefunction -with the velocity distribution of the Cl atoms as the main observable. For increasing droplet sizes the final velocities decrease due to increased helium interaction. The results for $Br_2$ in He nanodroplets show similar oscillations and velocity shifts, with the key difference that a high probability (100% for nanodroplets of 1000 He atoms) of recombination of the fragments was obtained. This is owed to the lower excitation energy if the $Br_2$ X to B transition and a higher reduced mass in comparison to $Cl_2$.

**Experimental evidence**
The dissociation and subsequent recombination of iodine in rare gas solvents can be deduced experimentally by taking a look at ion pair state fluorescence, as a measure of the B-state population as done by Lienau and Zewail [14]. This showed the dissociation and recombination dynamics of iodine in He, Ne, Ar, and Kr at pressures between 0 and 2000 bar, to change the solvent properties from gas to liquidlike fluids. The B-state shows a coherent wavepacket motion that decays over time. This can happen by four processes:

1. Predissociation without collision
2. Radiative decay
3. iodine-iodine collision induced nonradiative decay
4. iodine-solvent collision induced nonradiative decay

The latter is much faster than the first three, so this effect prevails - therefore the B-state mostly decays by collision-induced predissociation after coupling onto a repulsive potential and recombination onto A/A' states with subsequent vibrational relaxation. The predissociation is perceivable in an initial signal decay, with decay time decreasing with pressure and increasing with the mass of the solvent. This is slightly more complicated for very high pressures, where a rise in intensity is detectable due to geminate recombination. When taking a closer look at the PES of iodine one can observe several dissociative states crossing the B-state, but some may be ruled out due to symmetry arguments. Since the B-state is of ungerade symmetry, and this symmetry is destroyed during collision [18] the repulsive state that is responsible for the dissociation needs to be of gerade symmetry.

Pump-probe measurements of iodine in liquid $CCl_4$ showed decay of the B-state again within 200-700 fs, with the population loss attributed to predissociation. [13] The curve crossing was determined by the probe window at $\nu = 0$ and at (3.05-3.8) $\mathring{A}$. What is more, the electronic coupling between surfaces depends on the vibrational amplitude. The dynamics are characterized by a collision of the molecule with the solvent case, with a large energy transfer and scrambling of vibrational phases. Following this, the cage is more relaxed and the dynamics continue in the more harmonic part of the potential. The molecule not only dissociates in liquid $CCl_4$ but also shows geminate recombination due to the caging effect, as well as vibrational relaxation.[30] This has been shown in cyclohexane as well. Rates of relaxation and separation distances vary with the solvent - as shown by X-ray liquidography in real-time.

Similar results were obtained for argon clusters as a solvent, containing 40-150 atoms produced in a molecular beam. [31] For excitation into the weakly bound A-state, the laser-induced fluorescence showed a coherent motion within femtosecond timescales. With a dissociation at 300 fs, then a rebound from the solvent cage, and recombination at 600 fs. Preparation of the system in the B-state (figure 1.3) led to slower decay and recombination, both on the ps timescale.

This happened even for excitation below the dissociation threshold, due to the predissociation by crossing to one of the repulsive potentials.

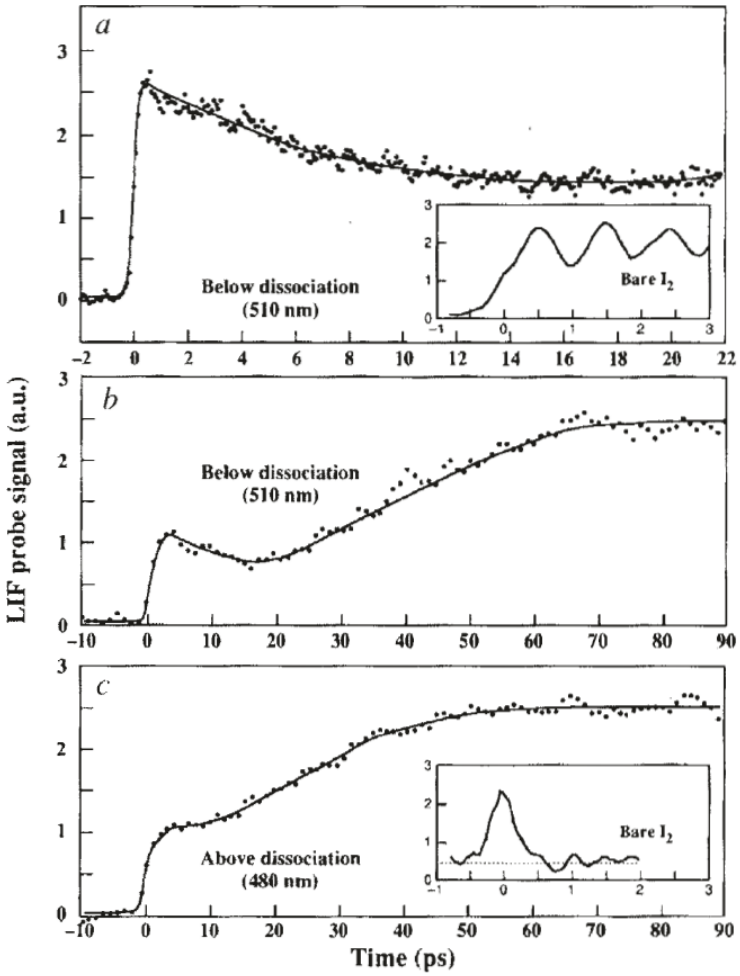


Figure 1.3: Laser induced fluorescence signal for excitation below (top and center) and above (bottom) the dissociation limit of the iodine B-state. Insets show measurements of effusive iodine, image taken from [31].

## 1.4 Superfluid helium droplets as cryomatrix

From a spectroscopic viewpoint, there is a huge gap between the investigation of isolated gas-phase molecules and species in a solution. As the example of predissociation of iodine shows, these two cases can lead to completely different physical properties. The study of isolated molecules is often complicated by fragmentation or the inability to produce weakly bound systems. A solution to these problems is the suspension in a buffer gas [14] or a solid cryogenic matrix. [32] This on the other hand often introduces complicated environmental effects sometimes impossible to entangle from the intramolecular dynamics. A way to bridge this gap are superfluid helium nanodroplets, which are exceptionally useful as cryogenic spectroscopy matrices. He nanodroplets promise cryogenic isolation with very little influence on the dynamics of embedded species - the droplet acting as a thermal bath absorbing the vibrational energy and providing spatial confinement for any reaction happening within. Moreover, since helium is transparent to photons of up to 20 eV, photoionization of dopants inside the droplets is possible.

The nanodroplets are made up of $10^3$ to $10^8$ He atoms and at temperatures of 0.37 K the otherwise nearly impossible isolation of atoms and molecules comes into reach. This is mostly owed to the superfluid phase transition to HeII at 2.18 K, where the He atoms undergo Bose condensation to the superfluid state - leading to the exotic property of zero viscosity. The nanodroplets are produced by the free jet expansion of cooled (5-20 K) and pressurized (20-100 bar) He through a micrometer-sized nozzle. The following supersonic expansion leads to cluster growth, droplet condensation, and most importantly - cooling. [5] Figure 1.4 gives an overview of the mean number size $\bar{N}_4$ depending on temperature and gas pressure.

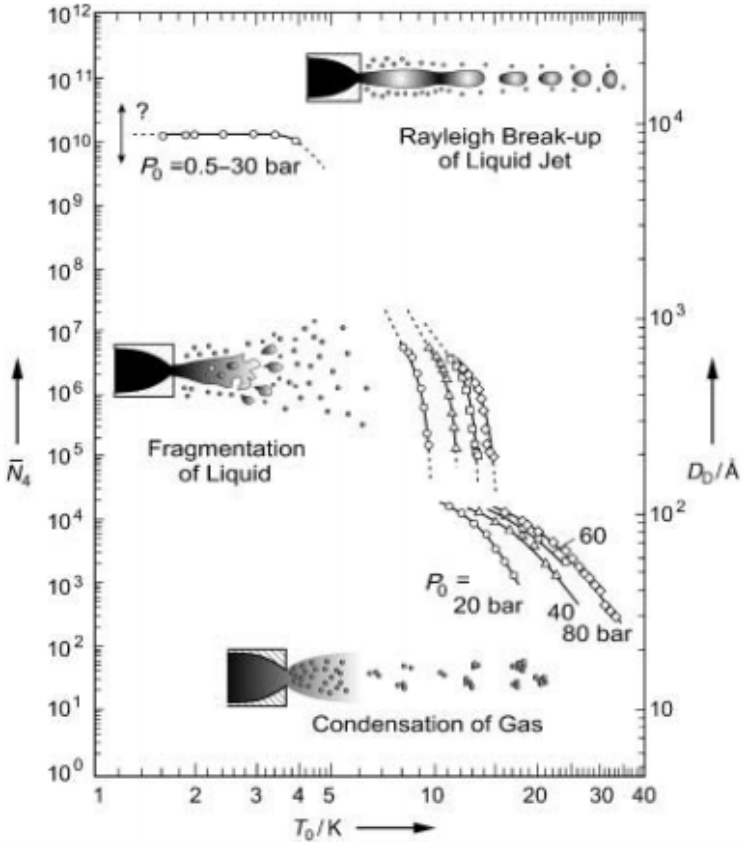


Figure 1.4: Different properties of helium nanodropelets droplets formed by jet expansion. Depending on the nozzle temperature different regimes form, influencing size and properties of the droplets. [5]

Subcritical expansion (bottom) leads to the smallest droplet sizes, by adiabatic gas expansion and condensation. At supercritical expansion (center) larger clusters are generated. To get to larger droplets expansion of the fluid at temperatures smaller than 4.2 K (top) can be used. [5]

## 1.5 Molecular dynamics in helium droplets

The influence of the He droplet environment on $I_2$ dynamics is still unclear, especially on the electronic coupling mechanism, which is the subject of this thesis. However, it has been shown that the superfluid helium has little influence on nuclear dynamics - both the dynamics of the He solvation shell for a single indium atom as a dopant and the motion of an $In_2$ wavepacket were investigated. [6, 7].

### 1.5.1 He solvation shell dynamics

After decades of static spectroscopy, the first time-resolved electronic excitation of dopants inside He nanodroplets were done by Thaler et al [6], laying the groundwork for completely new possibilities in matrix-isolated dynamic measurements. The photoexcitation dynamics of In inside the quantum solvent were studied by time-resolved photoelectron spectroscopy (TRPES) proving the possibility to study coupled electronic and nuclear dynamics of a particle in a superfluid helium droplet on an ultrafast timescale. Upon photoexcitation by a femtosecond pump pulse a delayed photoionization probes the time evolution of the excited state. The measurements were supported theoretically by time-dependent density functional theory (DFT).

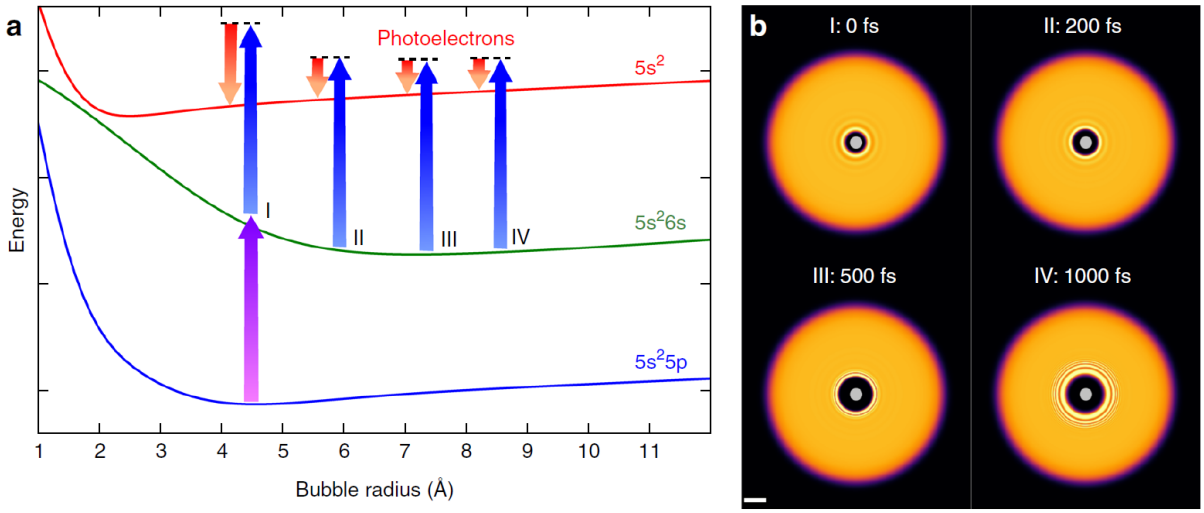


Figure 1.5: **a** In-$He_N$ PES as function of the bubble radius and pump (violet) probe (blue) scheme depicted schematically. **b** DFT calculations for an In atom inside a $He_{4000}$ droplet showing density distributions for different times. [6]

In Figure 1.5a, the PES as a function of the bubble radius are depicted. The pump pulse excites from the ground state $2s^2 5p(^2P_{1/2})$ to the first excited state $5s^2 6s(^2S_{1/2})$, the probe then ionizes to the ionic ground state $5s^2(^1S_0)$. As shown in figure 1.5b, the expansion of the valence electron wave function leads to a disturbance of the solvation shell manifested as an oscillating bubble inside the droplet. Pauli repulsion is responsible for the expanding electron orbitals pushing away the closed He shell. This was concluded through a transient shift in the pump-probe photoelectron spectrum during the first picosecond of measurements. The transient shift can be explained by temporal shift of the ionic state energy.

The bubble enclosing the excited dopant atom of In increases its radius from 4.5 $\AA$ to 8.1 $\AA$. This being a violent stimulus, the He bubble undergoes an oscillation measurable with a period of 30 ps by an increase in the kinetic energy of the photoelectrons. After a time of about 60 ps, the dopant is ejected from the helium droplet due to the repulsive In-He pair potential of the excited indium atom.

### 1.5.2 $In_2$ wavepacket motion

The next step for the time-resolved study of dynamics in He nanodroplets was the observation of vibrational wave packets of indium dimers ($In_2$). [7] Photoexcitation of the complex consisting of the He droplet and the solvated $In_2$ results response of the He solvation shell and a vibrational wavepacket in $In_2$. The two effects take place on a similar timescale and manifest themselves in the transient photoelectron spectra. The shell dynamics can only be isolated by comparison with In atom transients. The excited dimer $In_2^*$ is then ejected from the He nanodroplet upon photoexcitation. This is schematically shown in figure 1.6a, and a sketch of the PES as a function of intramolecular In-In distance in 1.6b. The wavepacket generated by exciting with the pump pulse is then probed with a second pulse, with a changing photoelectron/photo-ion yield caused by a different ionization probability depending on the position of the wavepacket. After an initial bubble expansion at about 1 ps, the dopant is ejected between 50 ps and 150 ps after the excitation.

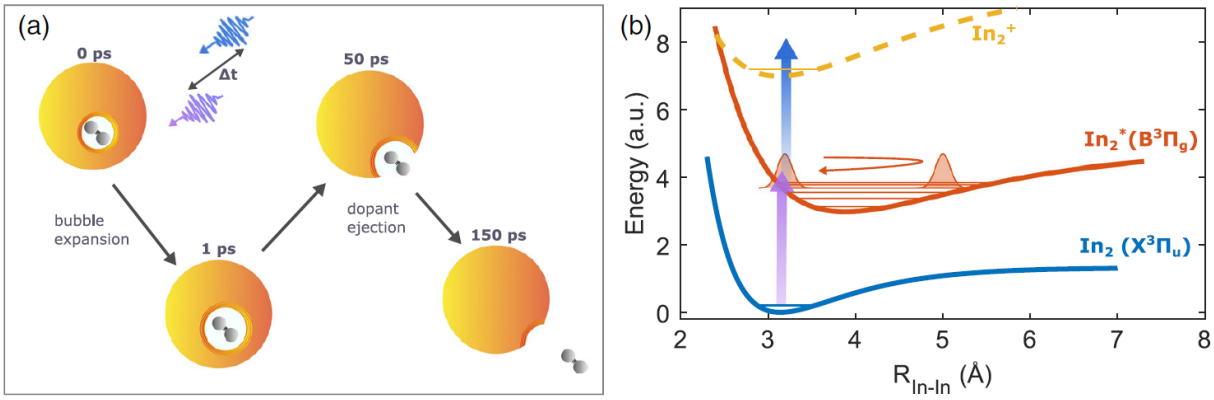


Figure 1.6: **a** Dynamics of $In_2$ in He nanodroplets - bubble expansion and dopant ejection, **b** Schematic of the PES showing a wavepacket motion of $In_2$ after photoexitation and subsequent ionization. Image taken from [7]

A superposition of several vibrational $In_2$ states is generated by the spectrally broad femtosecond laser pulse - the wavepacket motion being measurable in a modulation of the photoelectron signal with a periodicity of 420 fs. As the potential is anharmonic, the wavepacket disperses after time - with specific revival times where the individual states are in phase again. The first revival was measured at 290 ps. A reduced amplitude in the revival signal was measured, due to the decoherence of the wavepacket as a result of interactions of the $In_2$ molecule with He atoms. This is a purely elastic dephasing - concluded by the absence of a WP frequency increase that would be expected for inelastic dephasing. Strong initial decoherence shows the influence of the helium atoms seems to be stronger at the beginning, most probable as a result of the bubble expansion creating helium density waves, which are then reflected by the surface of the droplets. The later interaction and decoherence during the propagation of the $In_2$ molecule through the droplet showed to be much weaker.

What is notable here is that the full revival takes place after the molecule has been ejected from

the He droplet. This offers the possibility to study the oscillation signal in solution as well as for free molecules. From this, a decoherence half-life directly related to the interaction with the He environment of  10 ps was estimated. Moreover, a lower limit of 20 ps for the ejection of the $In_2$ molecule out of the droplet could be derived.

## 1.6 Indication for predissociation in superfluid helium nanodroplets

Time-of-flight measurements of iodine in the gas phase showed the expected behavior discussed in section 1.2. An initial oscillation with a period of 300 fs decays in intensity due to dephasing and revives again when the individual modes are in phase again. This is shown in figure 1.7.

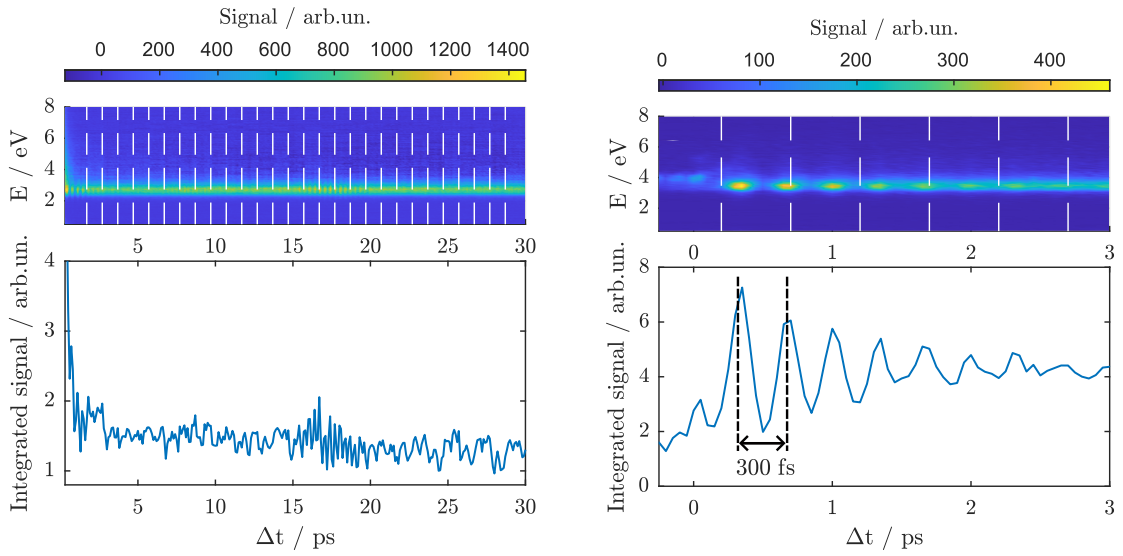


(a) Long timescale with revival

(b) Short timescale

Figure 1.7: Time-of-flight pump-probe measurement of $I_2$ in the gas phase, 600 nm excitation into the B-state. Photoelectron signal and kinetic energy depending on pump-probe time-delay. Surface plot (top) shows the energy of PEs over a time delay, and the colorbar indicates PE yield. The bottom shows signals integrated over all energies, oscillation duration of 300 fs.

First measurements of iodine solvated in $He_N$ indicated a very fast and efficient predissociation, the oscillation seen in the gas phase completely vanishes and a sudden drop in PE yield can be measured, as can be seen in figure 1.8. This could be an indication of a previously unknown strong electronic interaction of the superfluid helium environment with dopants contained by it.

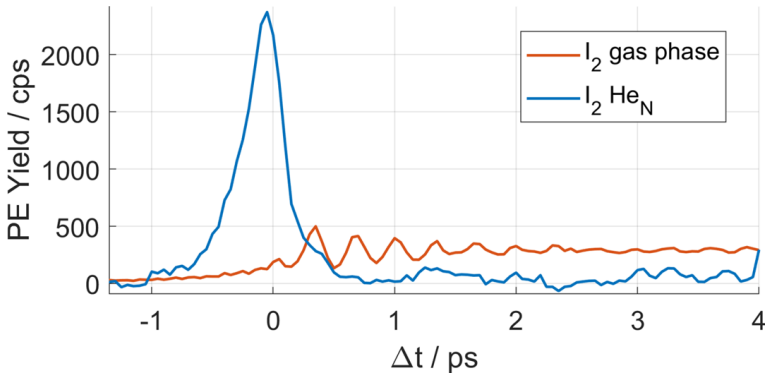


Figure 1.8: Time-of-flight pump-probe measurement of $I_2$ in the gas phase, 600 nm excitation into the B-state. Comparison of PE yield of effusive iodine (orange) with iodine solvated in $He_N$ (blue) as a function of pump-probe time-delay $\Delta t$.

# 2 Experimental Setup

The experimental setup used to study the dynamics of $I_2$ in superfluid He nanodroplets already existed before and is described in detail in the master's theses of Michael Stadlhofer [33] and Kerstin Absenger [34] and the PhD thesis of Bernhard Thaler [35]. For this thesis, has been expanded and adjusted for specific experiments, most notably by the velocity map imaging (VMI) detection system. A short overview of the optical and vacuum setup will be given, followed by a detailed description of the detection system - including measurement parameters, reference measurements, and general information on its operation.

## 2.1 Optical setup and laser system

The ultrashort laser pulses used for all the experiments are generated in a Ti:sapphire system composed of a Coherent Vitara Oscillator and a Legend Elite Duo Amplifier. This gives output pulses with a pulse duration of 25 fs at a repetition rate of 3 kHz, amounting to a total output power of 12.6 W. Spectrally the beam shows a center wavelength of 800 nm and roughly 60 nm FWHM bandwidth. It is then further manipulated in the optical setup, shown in figure 2.1.

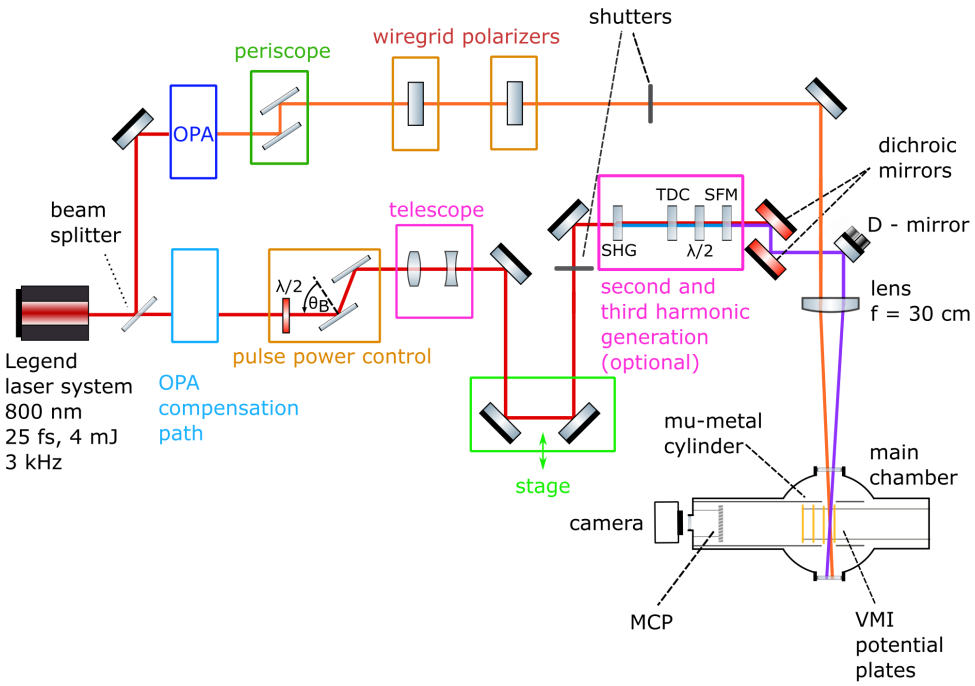


Figure 2.1: Optical Setup of Femtolab, the Legend laser system gives pulses of 25 fs with a wavelength of 800 nm. The beam is split in two, both pump and probe receive further manipulation before entering the vacuum chamber. Image adapted from [33]

Right after the Legend output a beam splitter divides the beam into two paths with an 80:20 ratio, the more intense part used for the Optical Parametric Amplifier (OPA) - which allows wavelength manipulation required for the pump pulse. Used for this work were 600 nm and 690 nm pump pulse wavelength. The polarization is then rotated (if needed) with a periscope, and two wire-grid polarizers enable the reduction of the pulse power. The beam path at the bottom of figure 2.1 is the path of the other 20 % of the Legend output, used for the probe pulse. The path lengths of both beams need to be the same for temporal overlap, so the path length of the probe pulse is adjusted in the OPA compensation path, to match the path length through the OPA. The temporal shift is then achieved with a movable stage. A $\lambda/2$ plate and two Brewster windows allow pulse power control - after this the beam width is reduced with a telescope.

Depending on the experiment the fundamental 800 nm output, the second harmonic, or the third harmonic is used to probe the molecular system. To generate 400 nm wavelengths, a Barium Borate (BBO) crystal allows for Second Harmonic Generation (SHG). To lower the wavelength further to 266 nm, Third Harmonic Generation (THG) is achieved by inserting a Sum Frequency Mixing (SFM) crystal. A Time Delay Compensator (TDC) and a $\lambda/2$ plate before the SFM compensate for the time delay of the 400 nm pulse with respect to the 800 nm puls and rotate the polarization of the 800 nm pulse.

Selection of the desired wavelength (if SHG or THG is used) is made by removing the unwanted fundamental wavelength with dichroic mirrors. Both pulses are then focused into the chamber with a lens focal length of f = 30 cm. Rough temporal overlap is set with a photodiode and an oscilloscope. Spatial overlap of the two pulses is set by inserting a mirror in front of the chamber and overlapping the two pulses on a camera -this can then be finetuned by exciting into the bound B state of iodine and moving one of the beams until the maximal signal is reached. By moving the stage the exact temporal overlap can be found, due to a vast increase in photoion-or electron signal when both pulses overlap spatially and temporally.

### 2.1.1 Laser characterization and focus optimization

The lenses used for all measurements are achromatic doublets (*THORLABS Near IR Achromate*) with a focal length of $f = 250$ mm or $f = 300$ mm. Figure 2.2 shows the focus of pump and probe beam on a camera (*ARTCAM-UV-WOM CMOS Camera*) with Gaussian fits to calculate the FWHM. One pixel corresponds to 10 $\mu$m. The telescope showed in the laser setup (see figure 2.1) was adjusted so that the pump focus was much larger at the point where the probe focus is the smallest - to allow for pumping a large volume and probing only a fraction of that.

The laser peak intensity $I$ can be obtained by the following relation:

$$I = \frac{4\sqrt{\ln 2}}{\pi^{3/2}} \frac{E_{\text{pulse}}}{d_{focus}^2 t_{FWHM}}. \tag{2.1}$$

With the energy of the laser pulse $E_{pulse}$ in Joule, the temporal width of the pulse $t_{FWHM}$ (roughly 25 fs $\pm$ 5 fs for the probe and 50 fs $\pm$ 10 fs for the pump), and the beam waist in the focus $d_{focus}$ given by the FWHM of the Gaussian fits.

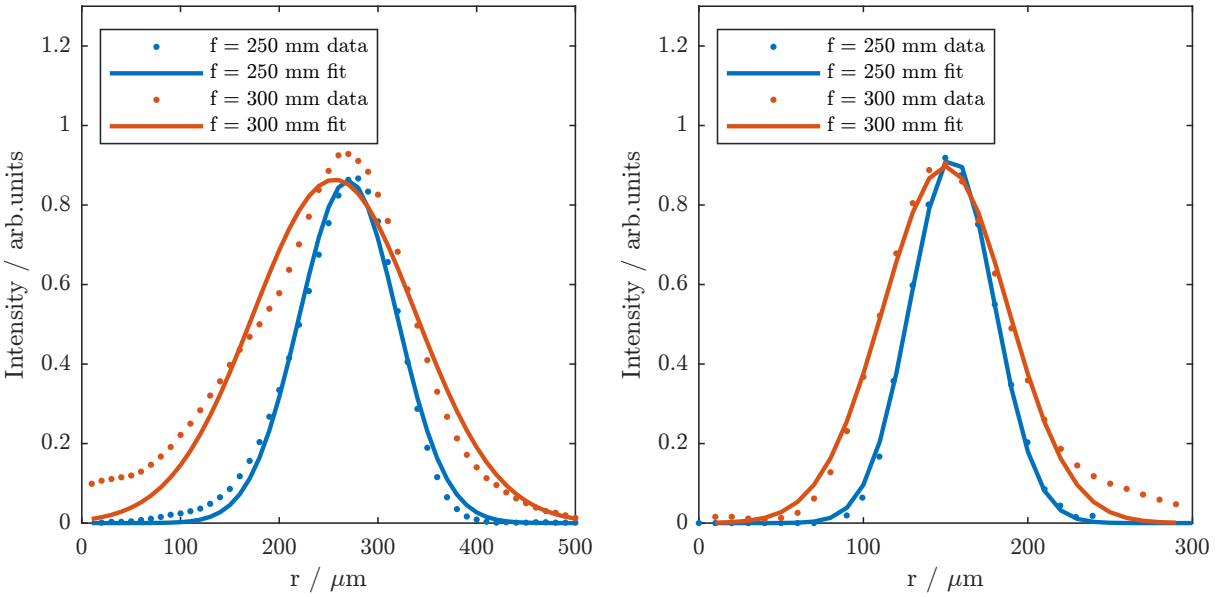


(a) Pump beam focus




(b) Probe beam focus

Figure 2.2: Laser beam foci with Gaussian fits as measured on *ARTCAM-UV-WOM CMOS Camera*, pixels have been calculated to $\mu$m (1 px = 10 $\mu$m ). For the FWHM values see table 2.1

The FWHM in $\mu$m for pump and probe for both lenses, as well as an example calculation for the corresponding peak intensities can be found in table 2.1. The exact laser intensities for every measurement is also noted.

Table 2.1: FWHMs of the Gaussian fits for pump and probe pulse, each with two different lenses with focal lengths f and the calculated peak intensity $I$ for a pump laser power of 150 mW and a probe laser power of 500 mW (repetition rate 3000 Hz)

| f / mm | FWHM$_{pump}$ / $\mu$m | $I_{pump}$ / W/cm$^2$ | FWHM$_{probe}$ / $\mu$m | $I_{probe}$ / W/cm$^2$ |
|---|---|---|---|---|
| 250 | 160 ± 20 | $(2,3 \pm 0,7) * 10^{12}$ | 90 ± 20 | $(4,9 \pm 1,1) * 10^{13}$ |
| 300 | 280 ± 20 | $(8 \pm 2) * 10^{11}$ | 130 ± 20 | $(2,4 \pm 0,6) * 10^{13}$ |

The wavelengths used for the experiments where 600 nm and 690 nm for the pump beam (to excite the B state and A state, respectively) and the fundamental output of the Legend at 800 nm to probe the system. Spectra of these are shown in figure 2.3 (pump) and figure 2.4 (probe).

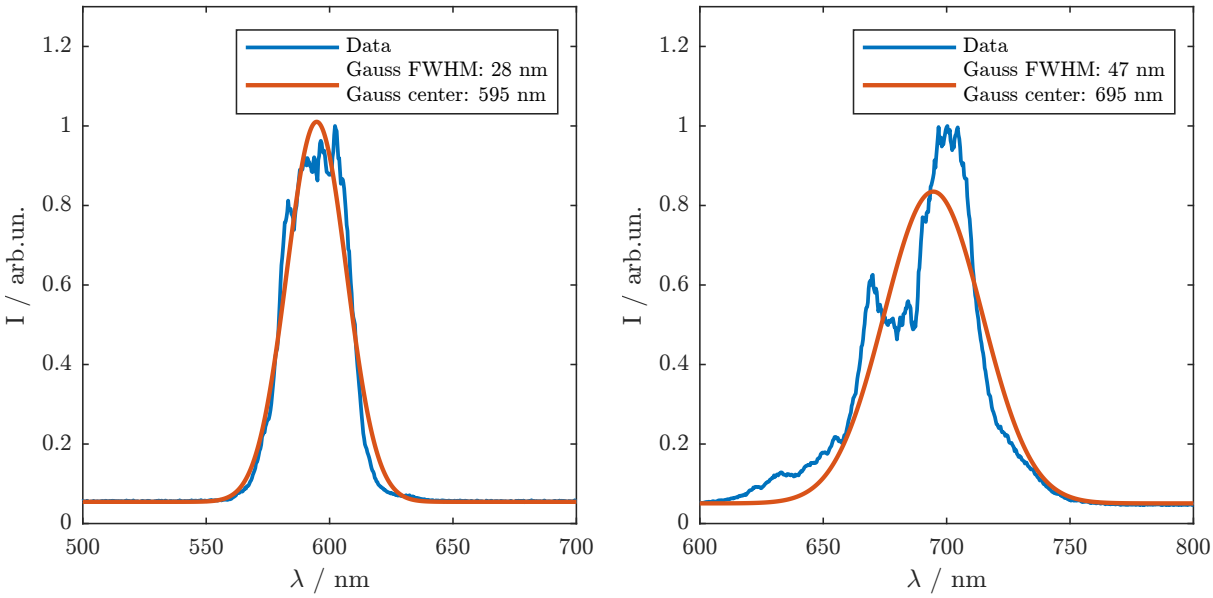


(a) 600 nm pump

(b) 690 nm pump

Figure 2.3: Laser spectra of 600 nm and 690 nm pump beam after the OPA

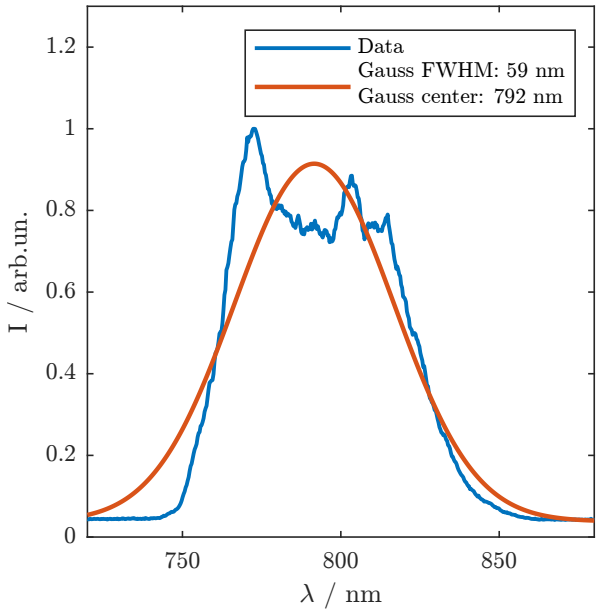


Figure 2.4: Spectrum of fundamental 800 nm Legend output (probe beam)

## 2.2 Vacuum setup

An overview of the complete vacuum setup can be seen in figure 2.5, it is divided into three separate ultra-high-vacuum (UHV) chambers, source chamber, pickup chamber, and main chamber. These three are connected with UHV valves, each pumped separately. The ToF spectrometer visible in blue at the bottom of the main chamber has been replaced by a VMI setup, this will be elaborated in section 2.3.

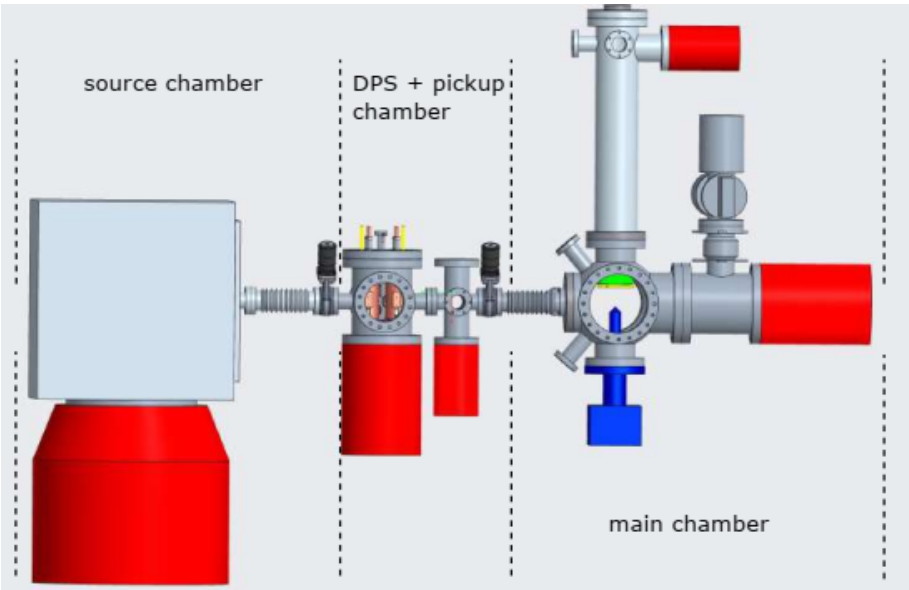


Figure 2.5: Complete Vacuum setup consisting of source chamber, pickup chamber and main chamber [35]. Differential pumping stage (DPS)

**Source chamber**
The He droplets are formed in the source chamber by supersonic expansion through a nozzle with 5 $\mu$m diameter as described in section 1.4 The nozzle is cooled by a 2-stage-compression Gifford-MacMahon process to 10 K. With a resistive heater the temperature is varied between 10-15 K, to produce different droplet sizes for a fixed He pressure of 25 bar at the nozzle. The temperature and pressure dependence of the He droplet size is shown in figure 2.6. The actual temperature of the droplets after supersonic expansion and vaporization of He atoms can be as low as 0.37 K, the superfluid phase transition to HeII taking place at 2.18 K. [5]

**Pickup chamber**
The beam of superfluid He droplets passes the pickup chamber (PUC) where the droplets are doped with effusive $I_2$. Pellets of solid iodine (VWR Chemicals) are kept in a reservoir that can be removed from the rest of the chamber for refills. The reservoir is connected to a Swagelock tubing with a valve, the tubing can be pumped separately by a rotary vane pump. This is then connected to the PUC with a dosing valve. The dosing valve controls the Iodine vapor pressure and thus the pickup by the helium droplets.

**Main chamber**
The main chamber contains the intersection between the He droplet beam and the laser beams, as well as the detection system and a Quadrupole Mass Spectrometer (QMS), model Balzers Instruments, QMG 422 Quadstar 422. This is used to monitor doping concentration and rest gases in the chamber as well as to align the He source.

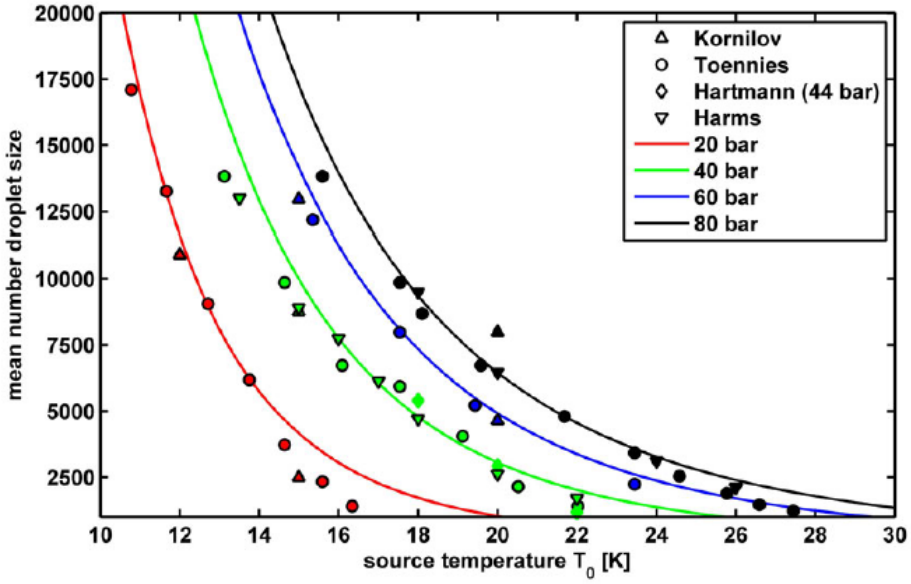


Figure 2.6: Experimental data on mean droplet sizes of superfluid helium nanodroplets generated by supersonic expansion depending on source Temperature $T_0$ for different He pressures. [5, 36, 37, 38] Image taken from [39].

## 2.3 Velocity map imaging spectrometer

The detection system located in the main chamber is made up of a velocity map imaging spectrometer, with a Micro-Channel-Plate (MCP) connected to a phosphor screen which is imaged by a CCD camera above it as shown in figure 2.7. Velocity map imaging was developed by Eppink and Parker [40], utilizing electrostatic lenses. Charged particles with the same mass-to-charge ratio (m/z) and initial velocity vector are mapped on the same spot on a position-sensitive detector. Information on the kinetic energy and angular distribution can then be extracted from the 2d image. The electric fields are set up in a way that the initial position of the particles has little to no influence on the results. The device geometry that we use has been adapted from Lutz Fechner [41] (in turn an adaptation of the Eppink and Parker electrode design). At the same time, the voltages pulses generated by ions hitting the MCP can be tapped to allow for Time-of-Flight (ToF) operation. Arrival times relative to the laser trigger are recorded, and a histogram with these times can then be transformed into an ion mass spectrum or a kinetic energy spectrum of electrons.

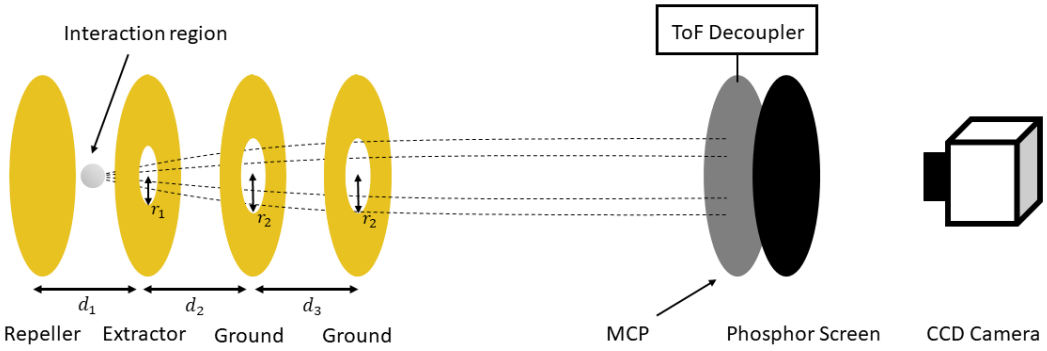


Figure 2.7: Schematic representation of the VMI detection system, an electrostatic lens composed of repelled, extractor and two ground electrodes focuses charged particles on a MCP

The laser pulses generate ions and electrons in an interaction region and depending on the sign of the applied voltages either of those can be detected. A voltage (positive if ions should be detected) is applied at the first electrode, which repels the charged particles - therefore denoted repeller. A second electrode (extractor) with an opening of radius $r_1 = 25$ mm is positioned, and the charged particles are accelerated through the hole and further accelerated by the extractor voltage (70 % of the repeller voltage). The exact ratio for a projection without distortion is found with experimental optimization. The voltages used for the measurements can be found in section 2.3.5 table 2.2. Two more electrodes connected to ground follow, both with an opening $r_2 = 30$ mm. All of the electrodes have a diameter of 100 mm, a thickness of 2 mm and are separated by a distance of $d = 14.6$ mm. The electrostatic fields then form a lens as shown in figure 2.8 which accelerates the charged particles on the detector

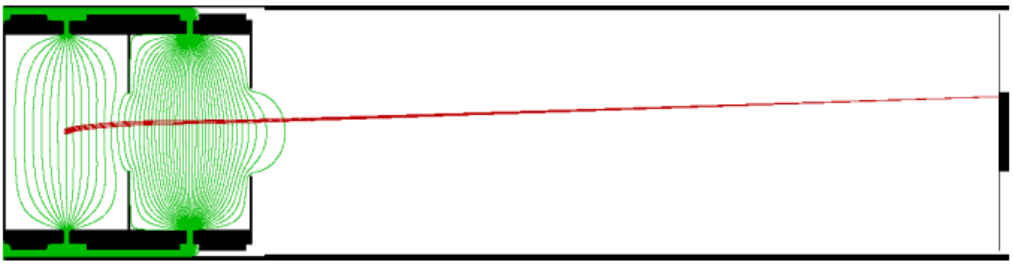

Figure 2.8: Simion simulation of the electrostatic fields forming around the VMI electrodes, equipotential lines in green and particle trajectories in red, image taken from Lutz Fechner's master thesis [41]

The relevant observables to gather 3D information on particles are the flight time $\Delta t = t - t_0$, the change in $x$ position $\Delta x = x - x_0$ and the change in y position $\Delta y = y - y_0$ in respect to a reference $x_0, y_0$ and $t_0$.[42] One can define a vector containing all these relevant observables $\vec{I} = (I_1, I_2, I_3) = (\Delta x, \Delta y, \Delta t)$ which is related to the initial product momentum vector $\vec{p} = (p_x, p_y, p_z)$

$$\vec{I} = \hat{M}\vec{p} \tag{2.2}$$

via the diagonal global momentum matrix $\hat{M}$

**Time of flight**
A conventional ToF mass spectrometer measures particles' flight times $\Delta t$ but the information on the position is lost. Therefore the flight time is only related to the momentum in the $z$ direction:

$$\Delta t = M_{tz} \cdot p_z \tag{2.3}$$

The matrix element $M_{tz}$ can be calculated with the mass of the particle $m$, the length of the acceleration field $l$, and the average ToF $t_0$:

$$M_{tz} = \frac{3t_0^2}{8ml} \tag{2.4}$$

**2D imaging**
By using a time-integrating, but position-sensitive detector (like in our setup) it is possible to calculate the momenta in the x and y directions by measuring the displacement $\Delta x$ and $\Delta y$

$$p_x = \Delta x / M_{xx} \tag{2.5}$$

$$p_y = \Delta y / M_{yy} \tag{2.6}$$

Thus establishing a linear relationship between momentum and displacement on the detector, which is later utilized in the calibration of the detector.

A 3D drawing of the setup is shown in figure 2.9. Helium droplet beam and laser beams are set up so that they intersect between repeller and extractor. To minimize influence and disturbances from external electromagnetic fields, the whole flight tube is shielded with $\mu$-metal. The charged particles are focussed on a MCP with electrostatic lensing. The electrons generated in the MCP are then accelerated onto the phosphor screen and excite fluorescence which is read out by the CCD camera.

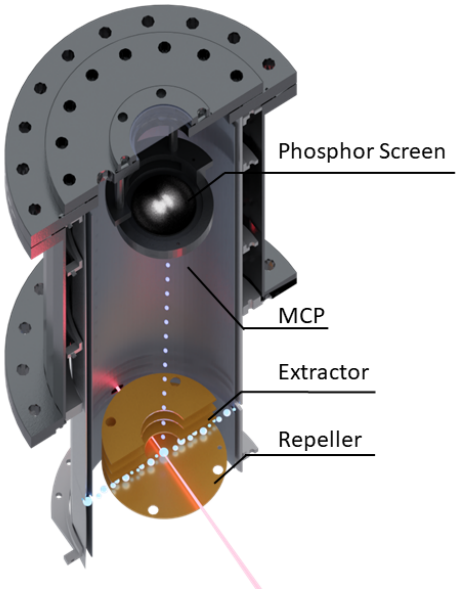


Figure 2.9: 3D drawing of the velocity map imaging (VMI) detection system, as developed by Bernhard Thaler and Leonhard Treiber - credits to Michael Stadlhofer for drawing. An electrostatic lens composed of repeller, extractor, and two ground electrodes focuses charged particles on a MCP, spatially confided electron avalanches then induce fluorescence on a phosphor screen which is read out by a CCD camera.

**Camera readout**
A CCD camera *(Flir Blackfly S BFS-U3-27S5M-C)* reads the phosphor screen and a C++ algorithm written by Michael Stadlhofer then calculates centroid coordinates for each fluorescent spot. A hit at the center of each spot is added to the final image and saved along with the size of the spot.

**Voltage gating**
A significant improvement regarding signal to noise ratio could be achieved by detecting only the fragments of the dissociation, in this case $I^+$ ions. To map only specific ion masses (or rather m/z ratios), a high-speed switch is connected to the MCP. A trigger stemming from the laser system is connected to it and allows gating at specific flight times. The MCP back voltage is reduced to 1.35 kV for this, and -800 V is applied at the MCP front if detection is desired. The voltage difference across the MCP for ions hitting the MCP outside of this time window is then too low for efficient detection. The switch gives a voltage output as shown in figure 2.10- this can be shifted in time with respect to the laser as well as the width changed by adjusting the connected delay.

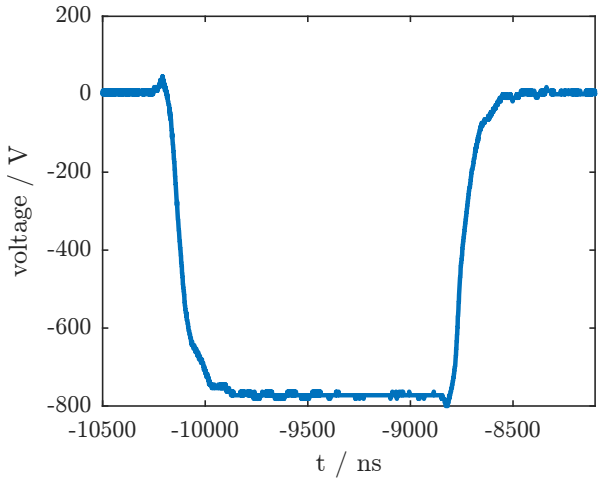


Figure 2.10: Voltage output of the high-speed switch connected to the MCP front to gate on specific masses

### 2.3.1 Characterization of the detector

The voltages set at the phosphor screen and at the back of the MCP need to be set in a way that the detector shows the following properties:

1. Minimal noise
2. High detector efficiency, to detect as many hits as possible
3. Narrow voltage pulses for individual hits to ensure little overlap of individual hits (this leads to problems in hit recognition)
4. Only hits during the gating window to detect the specific masses

To optimize the voltages, the dark counts of the detector as well as hit size distributions were measured.

**Dark counts**
Dark counts are measured without a laser present in the chamber (no generation of ions) and the voltages at repeller and extractor turned off. These false detection events need to be minimized while still maintaining high detector efficiency. Figure 2.11 shows the dark counts for varying MCP back voltage and three different phosphor voltages, -800 V are applied at the MCP front gating on the $I^+$ mass. The counts drop to nearly zero for MCP back voltages below 1.5 kV, while the phosphor voltage did not strongly influence the result.

**Hit size distributions**
The hit sizes need to be optimized so that they are small enough to not overlap and big enough to ensure efficient detection. As figure 2.12a shows, the hit sizes decrease fast with decreasing MCP back voltage, without much influence of the phosphor voltage. In figure 2.12b the hit size distributions (calculated by the camera evaluation software for each hit) for MCP back voltages ranging from 1.30 kV to 1.65 KV for a phosphor voltage of 4.2 kV displayed. The hitsizes shown here are calculated before the "prebinning" of the camera, which reduces the image size, and therefore increases the size of a single pixel.

Since the phosphor voltage did not greatly influence these measurements it was set to 4.2 kV for all measurements, as it subjectively led to best detection efficiency. MCP back voltages above 1.5 kV gave a significant proportion of counts from outside of the gating window. This was checked by shifting the gate window around the sharp effusive mass peak of $I^+$. In figure 2.12 this can

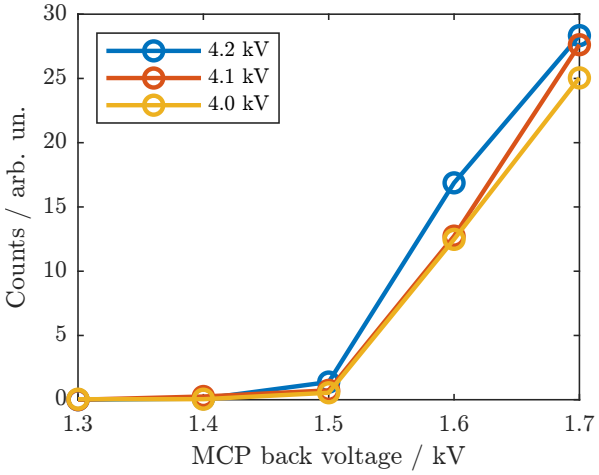


Figure 2.11: Dark count measurement, without a laser present in the chamber and the voltages at repeller and extractor turned off. Counts on the phosphor screen read out by the camera depending on MCP back voltage for phosphor voltages of 4.2 kV, 4.1 kV, and 4.0 kV. MCP front at -800 V.

be seen by the hits with very small areas, since the voltage across the MCP is lower outside of the detection window, less electrons are generated, resulting in a smaller spot on the phosphor screen. The spots are however still detectable if the MCP back voltage is too high. Moreover, large hits already began to merge together, thus complicating detection of individual counts, this shows itself in the stretched tails of the hit size distributions for higher MCP back voltages. It was set to 1.35 kV - this was a tradeoff between detector efficiency and the detection window.

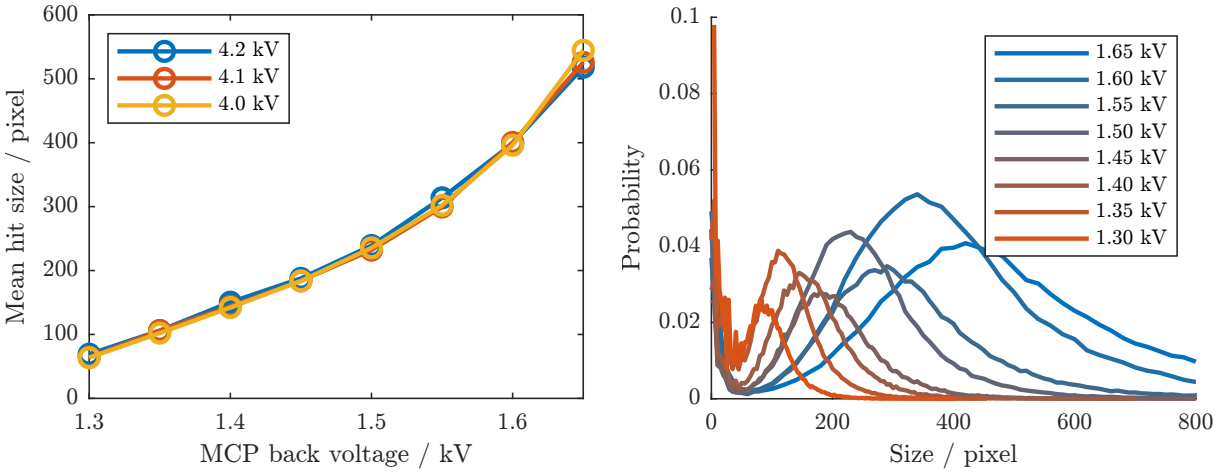


(a) Mean hit sizes depending on MCP back voltage, for phosphor voltages of 4.0, 4.1, and 4.2

(b) Hit size distributions depending on MCP back voltage at a phosphor voltage of 4.2 kV

Figure 2.12: Hit size distributions of $I^+$ ions generated by multiphoton ionization of $I_2$ molecules in the gas phase. Sizes depending on MCP back voltage and phosphor voltage with MCP front gated at -800 V on the $I^+$ mass

### 2.3.2 Energy calibration ion mode

When intense laser radiation rips away an electron at each iodine atom, these now negatively charged particles repel each other via the Coulomb potential, generating vast amounts of kinetic energy - also denoted Coulomb explosion. A probe-only measurement with 800 nm is shown in figure 2.13. The velocity map image on the left shows a distinct structure of two lobes, corresponding to the kinetic energy release from dissociation. A faint ring can be seen at higher velocities - which represents this Coulomb explosion. This can also be seen in the velocity map image integrated over all angles (figure 2.13 right) that shows a peak at high radii.

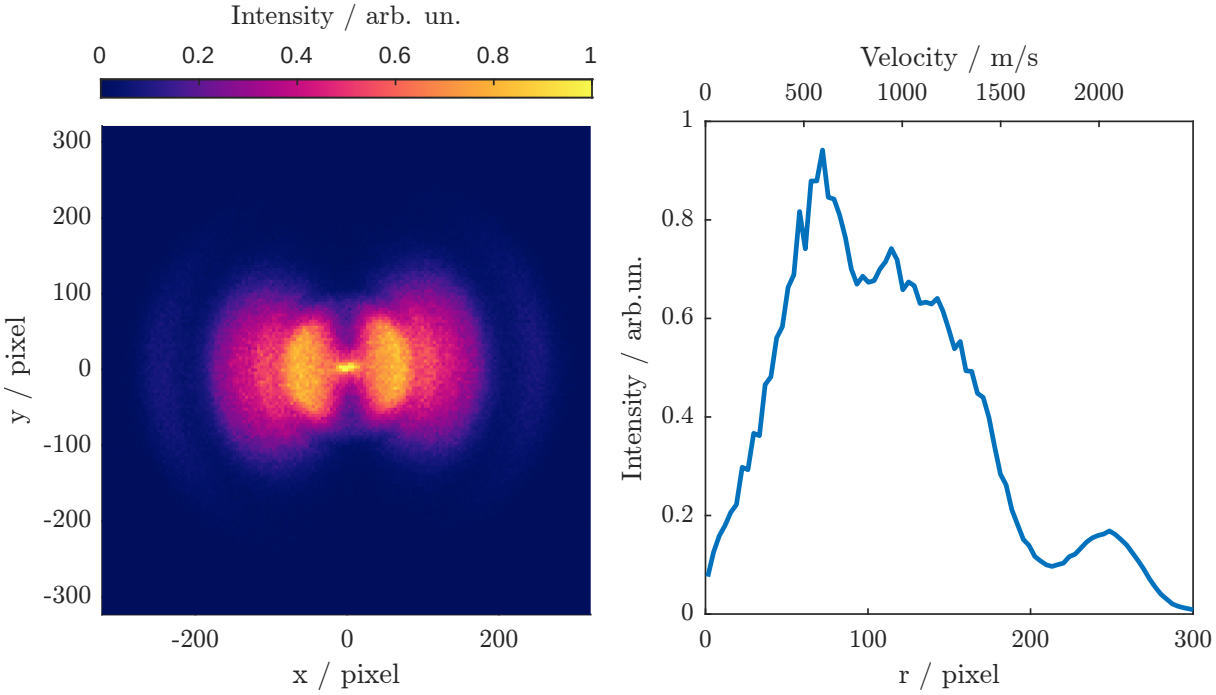


(a) Processed image

(b) Angular integrated radial plot

Figure 2.13: Velocity map image and radial distribution of $I^+$ ions generated by multiphoton ionization of effusive $I_2$ VMI molecules by the 800 nm probe pulse

Since this process releases energy given by the Coulomb potential it can be used to calibrate the detector. The force between two point charges $q_1$ and $q_2$ at locations $\mathbf{r}_1$ and $\mathbf{r}_2$ is given by the Coulomb law:

$$\mathbf{F} = \frac{q_1 q_2}{4\pi\varepsilon_0} \frac{\mathbf{r}_1 - \mathbf{r}_2}{|\mathbf{r}_1 - \mathbf{r}_2|^3} = \frac{q_1 q_2}{4\pi\varepsilon_0} \frac{\hat{\mathbf{r}}_{12}}{|\mathbf{r}_{12}|^2} \tag{2.7}$$

Where $\mathbf{r}_{12}$ is the distance between the two charges and $\varepsilon_0$ the electric constant. The electric potential U between the two point charges is then:

$$\mathbf{U} = \frac{1}{4\pi\varepsilon_0} \frac{q_1 q_2}{|\mathbf{r}_{12}|} \tag{2.8}$$

In the case of two positively charged iodine atoms with charge $+e$ this simplifies to:

$$\mathbf{U} = \frac{1}{4\pi\varepsilon_0} \frac{e^2}{|\mathbf{r}_{12}|} \tag{2.9}$$

and $\mathbf{r}_{12}$ is then assumed to be approximately the equilibrium distance of the ground state which is 2.65 $\mathring{A}$ [22]. The potential energy should then be converted directly into kinetic energies $\mathbf{E_{kin}} = \frac{\mathbf{mv}^2}{2}$ of the two atoms with mass 127 u. This leads to a dissociation velocity of $\mathbf{v_{diss}} = 2033$ m/s per atom.

The linear relationship that was established in equations 2.5 and 2.6 gives an equation of the form $v = ar$ between the velocity $v$ of the ions and the radius $r$ on the screen It is assumed the detector has the same coefficient in x and y direction. The peak that can be attributed to the Coulomb explosion for a probe-only measurement is located at $(246 \pm 5)$ pixel and its position is independent of probe power as shown in figure 2.14. This results in the coefficient for the raw data $a_{raw}$:

$$a_{raw} = (8.26 \pm 0.17)\ \frac{\text{m/s}}{\text{pixel}} \tag{2.10}$$

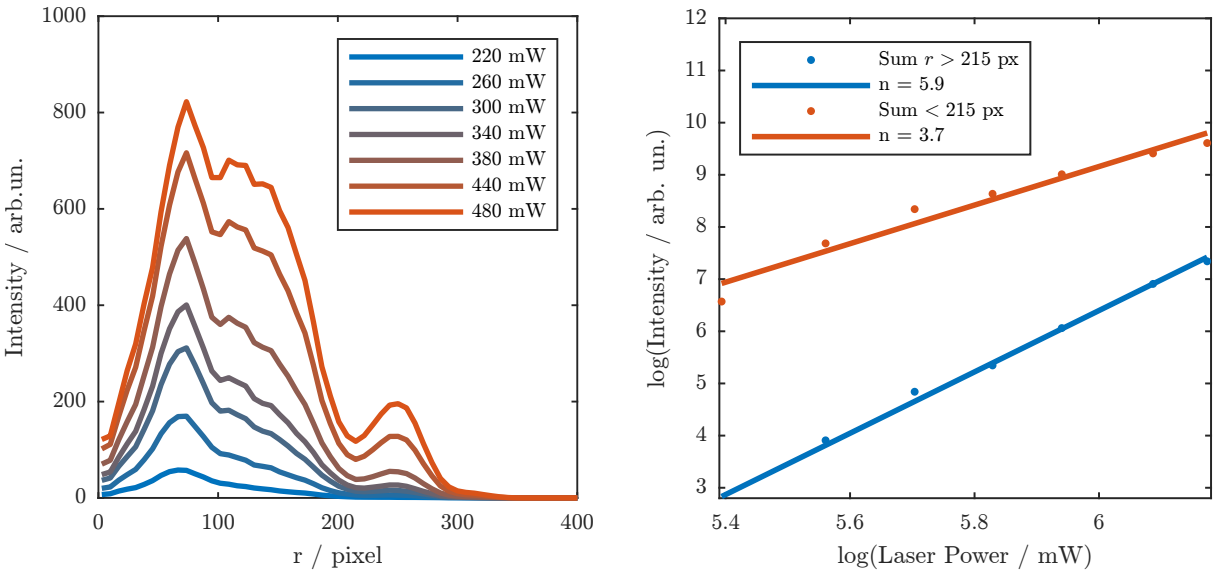


(a) Angular integrated radial plot

(b) Logarithmic power dependence

Figure 2.14: Radial probe-only velocity plot for different probe power and logarithmic power dependence (b) of Coulomb peak (r>215px) compared to the rest of the signal (r>215 px)

The logarithmic dependence of the height of the Coulomb peak for different probe powers that are shown in figure 2.14a gives information on the number of photons that this specific process requires via the relationship $I = P^n$ where I is the peak intensity, P the laser power and n the number of photons. Figure 2.14b shows such a logarithmic plot for the sum of intensities for radii $> 215$ pixel (which contains the Coulomb peak) and for the sum of radii $< 215$ pixel (the rest).

A linear fit through the data then gives $n = 5.9$ - approximately 6 photons for the Coulomb peak and n $n = 3.7$ approximately 4 photons for the rest. This verifies that this is indeed the multiple photon process associated with the Coulomb explosion, where significantly more photons are required than for the processes that generate the signal at lower radii. Ionization of $I_2$ with 800 nm requires 6 photons, the smaller slope could be due to saturation effects. This also matches well when comparing the measurement points with the line, a fit through the first three measurements would give a larger slope than for the last three.

### 2.3.3 Abel inversion

The 2d image visible in figure 2.13 a shows the raw data obtained with the VMI. As shown schematically in figure 2.15 the velocities are a 2d projection of an initial 3d velocity distribution - the Abel transform:

$$F(r') = 2\int_{r}^{'\infty} \frac{f(r)r}{\sqrt{r^2 - r'^2}} dr \tag{2.11}$$

Abel inversion is a method to reconstruct the original distribution in the ideal case of cylindrical symmetry. The inverse transformation is given by:

$$f(r) = -\frac{1}{\pi}\int_{r}^{\infty} \frac{dF}{dr'} \frac{dr'}{\sqrt{r'^2 - r^2}} \tag{2.12}$$

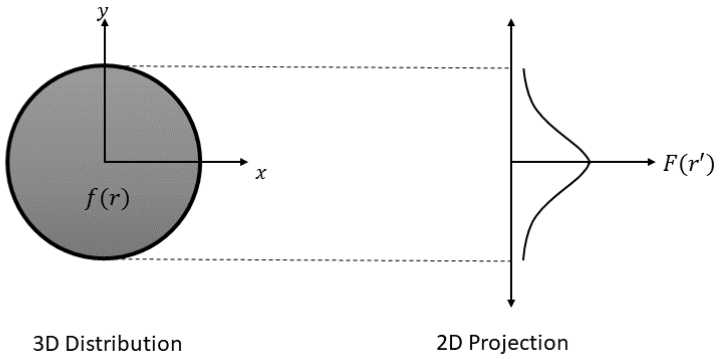


Figure 2.15: Schematic of the 2D projection $F(r')$ from an initial 3D distribution $f(r)$ (Abel inversion)

The python library 'Abel' allows to do this inverse transformation, and to take a slice out of the 3d distribution, figure 2.16a shows the Abel inverted data (bottom) of figure 2.13a compared with the raw data (top). The transformed image results in sharper features, with a slight shift to higher radii. A similar kinetic energy calibration to the raw data can be done.

Shown in the image is only the calibrated x-axis, to overlay the two radial distributions. In the radial data given by the Abel library the Coulomb peak is shifted to (260 $\pm$ 5) pixel and this results in the coefficient for the Abel inverted data $a_{Abel}$:

$$a_{Abel} = (7.79 \pm 0.2)\ \frac{\mathrm{m/s}}{\mathrm{pixel}} \tag{2.13}$$

An Abel inversion gives only good results when the data shows a low enough level of noise, as for this effusive probe only measurements. For pump-probe measurements, the noise tends to increase due to the subtraction of the pump and probe-only contributions, even more so for helium measurements (where the background is subtracted as well). For those measurements, Gaussian smoothing is applied before attempting an Abel inversion, and even then the results are not always usable. Therefore not all measurements in this work will be Abel transformed. Too noisy data will result in artifacts, mostly concentric rings.

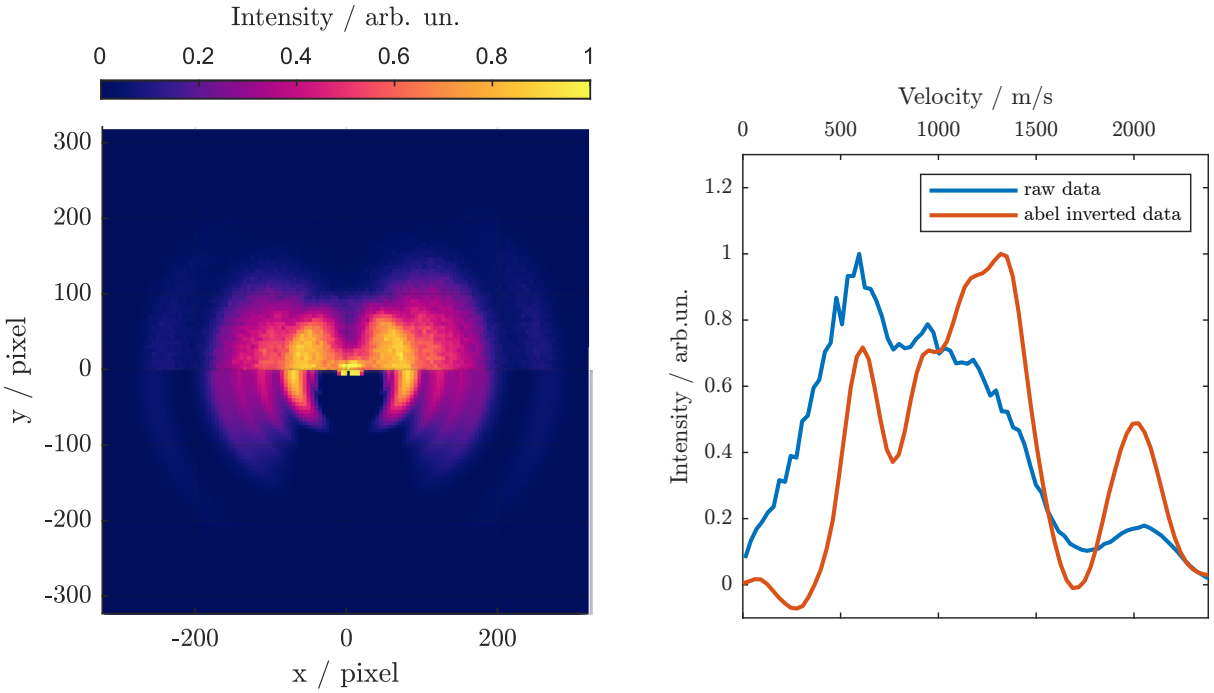


(a) raw velocity map image (top) and Abel inverted image (bottom)

(b) Velocity distributions (overlapped) of raw and Abel inverted data

Figure 2.16: Comparison of Abel transformed and raw data of $I^+$ ions generated by photodissociation of effusive $I_2$ moleculs with the 800 nm probe pulse

### 2.3.4 Energy calibration electron mode

Not only fragment ions can be detected with the VMI, but of course by reversing the sign of the electrode voltages also electrons spectra can be recorded. A voltage of -4 kV was applied at the voltage divider, 4 kV at the phosphor screen as well as 2 kV at MCP back (MCP front 0 kV). A probe-only measurement allows the calibration of the detector to electron kinetic energies.

Figure 6.3 shows a probe-only (800 nm probe) electron measurement. The data have been binned into bins of size 4x4 pixels, Gaussian smoothed, and then Abel inverted. For the raw measurements see appendix (figure 6.3). Distinct peaks in the radial distribution are visible, which can be used to calibrate according to the kinetic energy of the electrons by assuming that the structures are generated by ionization with 6,7 and 8 (800 nm) photons (one photon having an energy of 1.549 eV). The hits at the center of the image then correspond to 6 photon ionization, with an excess energy of 0.004 eV. An ionization with 7 photons gives a kinetic energy of 1.553 eV, which has been associated with a peak at 140 pixels. The second peak at 260 px can then be attributed to 8 photon ionization - with an excess energy of 3.102 eV. The calibrated x-axis on top of 6.3b has been generated by assuming a linear relationship between the kinetic energy $E_{kin}$ and the radius $r$ in pixel via a constant $b$: $E_{kin} = br$ .
By taking the mean value of the constants calculated with the two peaks the constant $b$ computes to:

$$b = (0.012 \pm 0.005)\frac{\text{eV}}{\text{pixel}} \tag{2.14}$$

The peak at 140 pixels has a linewidth $\frac{\Delta E}{E}$ of 22 %. The resolution of a ToF measurement can be as low as 4 % (not including laser bandwidth) [43], nevertheless this should suffice for most applications

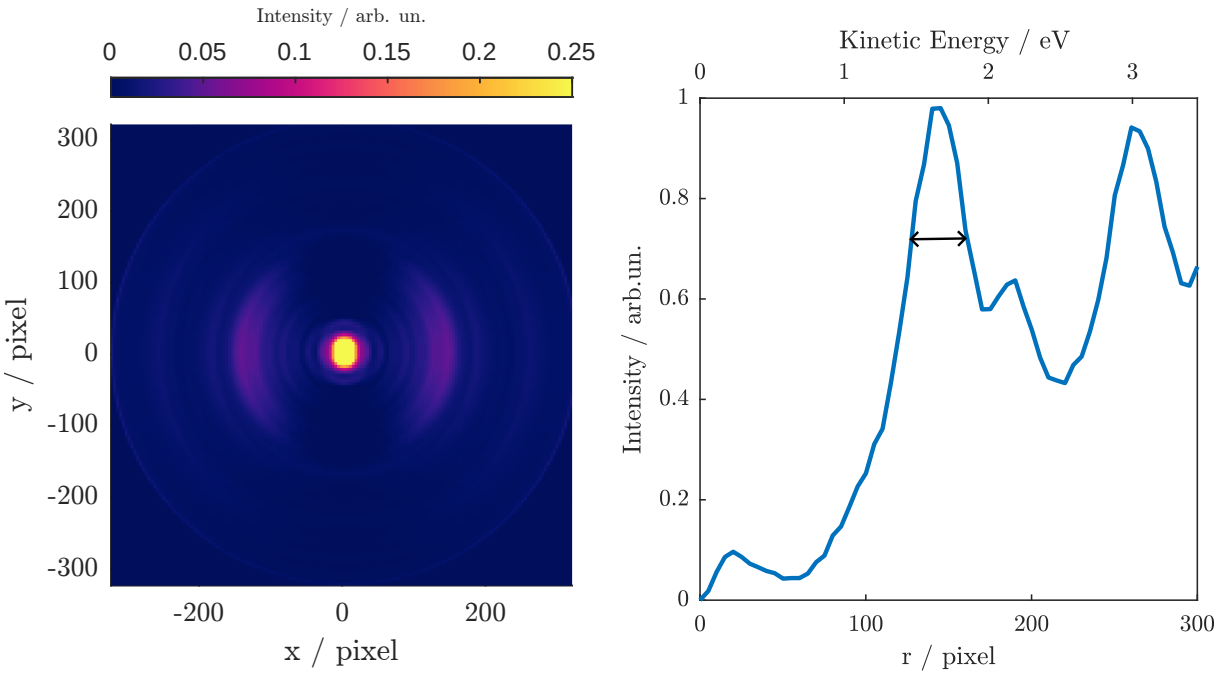


(a) Abel transformed image

(b) Radial distribution

Figure 2.17: Abel transformed 2d image and radial distribution of electrons generated by ionization of effusive $I_2$ with the 800 nm probe pulse. Arrow indicates linewidth (resolution)

### 2.3.5 VMI Parameters

To generate useful measurements with the VMI, the two laser foci need to be set up in the center of the region between the repeller and extractor, as well as the helium beam. This serves as a manual on how to operate the detector.

The laser and switch operation parameters may differ if another molecule is observed, so a thoughtful consideration of what to expect from the physical process is needed beforehand. For example, with the iodine molecule, the measurements in this work always used probe powers of 500 mW, and the gate was set on $I^+$. Afterward, it turned out that the signal was most likely generated by Coulomb explosion of molecules inside the droplets - therefore higher laser power and gating on $IHe_N$ mass peaks proved to be more effective.

The He beam is set up by maximizing the 8u signal at the QMS if the chambers are aligned correctly. For the VMI the necessary voltages need to be applied, depending on whether the switch is active or not. The values are found in table 2.2

Table 2.2: VMI voltages depending on operation mode

| | MCP front / kV | MCP back / kV | phosphor / kV |
|---|---|---|---|
| with switch | -800 | 1.35 | 4.2 |
| without switch | 0 | 2.05 | 4.2 |

Moreover, the ToF detector will not detect any hits if the MCP back voltage is too low, the minimal necessary MCP back voltage is 1.65 kV (for -800 V MCP front). Even then the GaGe card discriminator limits (these set the detection threshold of voltages generated by the ToF) need to be lowered from their usual values. Therefore simultaneous time-of-flight and VMI measurements are not recommended, since both detection methods require different voltages for

ideal operation. However, the ToF still serves to find the mass peaks of the molecules of interest and to set the gating window accordingly.

Setting up the beams is best done without the switch, detecting all masses leads to more signal. To set up the probe focus in the center of the interaction region, a voltage will only be applied at the repelled, and the extractor connected to ground. By moving the beam horizontally, the beam is set so it is centered on the VMI image, as shown in figure 2.18a. This is also dependent on the laser polarization, a polarization in the image (or optical table) plane that will give an image as shown in figure 2.18b.

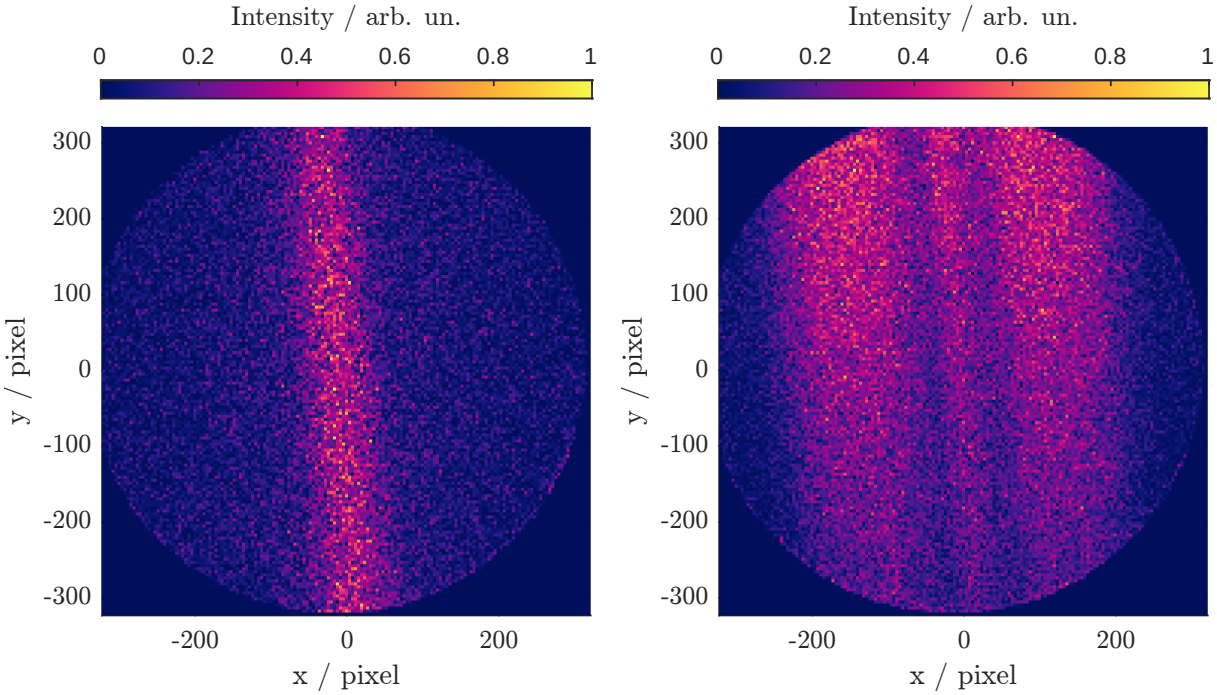


(a) Probe polarization normal to the image plane

(b) Probe polarization in the image plane

Figure 2.18: Image of ions generated by the 800 nm probe beam taken with the VMI with 0 V extractor voltage (no focusing) for different laser polarization. This is done to center the beam in the spectrometer.

Maximizing the signal stemming from inside helium droplets is done by gating on the $IHe_N$ masses (where $N = 1, 2, ..., 10$, including the first 10 peaks should suffice). Practically this is achieved by moving the beam in the z and x direction and focus in the chamber in the y direction to ensure the right focus position. As shown in figure 2.19 it is assumed that the beam of effusive molecules is wider than the helium droplet beam, and the laser focus needs to be set in the region of highest droplet density. In the case of $I_2$, this is done with the probe beam, since a high probe intensity on the He beam is required.

Adjustment of the voltage divider then focuses the image on the detector, a wrong voltage ratio will lead to a distortion of the image. To do this the MCP gate is best set so that $I_2+$ is also included, since this results in a sharp line at the center of the image which allows easier focusing. Figure 2.20 shows a focused image (a) and a distorted one (b).

The lobe-like directed structure (as shown before in figure 2.13) is only visible if the laser polarization is in the detector plane, a polarization normal to that will give 2d Gaussian distribution - see figure 2.21. This is owed to the fact that the laser will select the molecules that have their molecular axis perpendicular to the laser polarization and thus preferably dissociate in that plane.

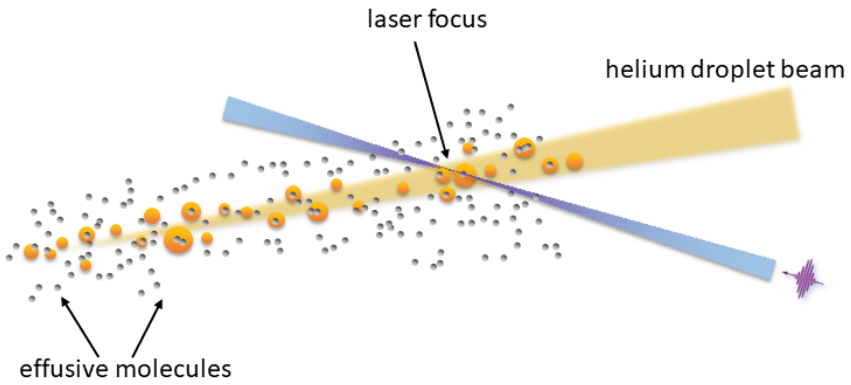


Figure 2.19: Schematic of the helium droplet beam and effusive molecule beam in the vacuum chamber. The probe beam focus needs to be set in the center of the helium droplet beam to maximize the signal originating from inside helium nanodroplets

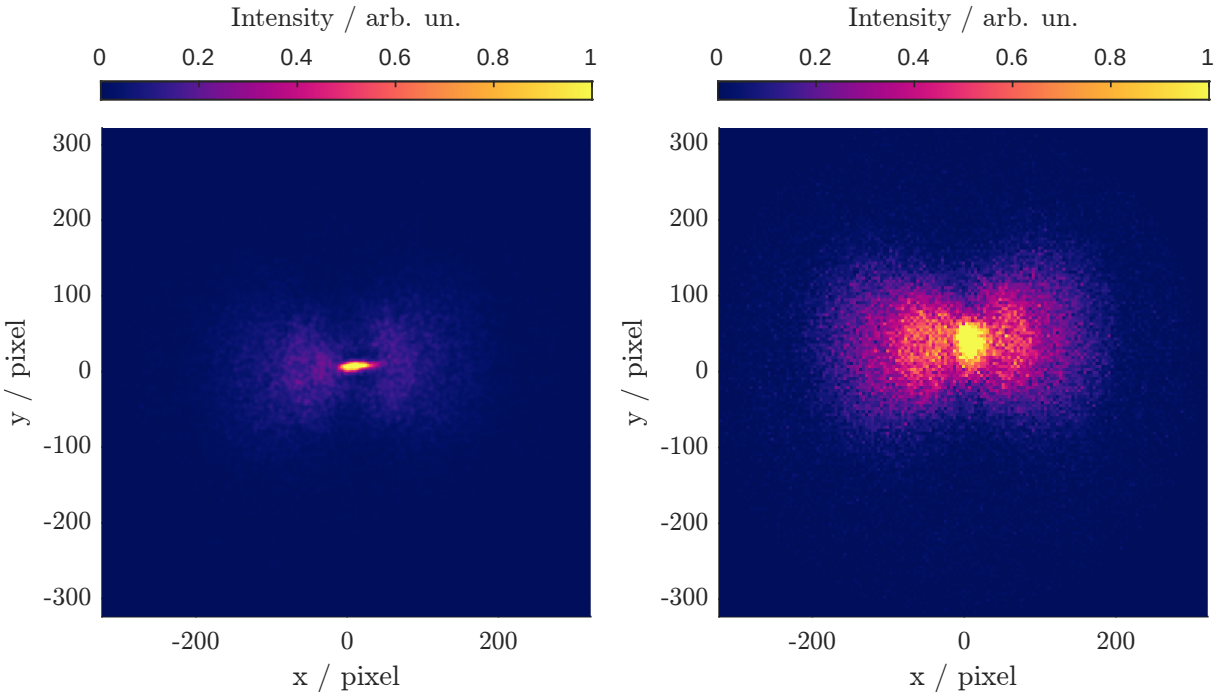


(a) Focused probe only VMI

(b) Distorted probe only VMI

Figure 2.20: 2D image of ions generated by photodissociation of effusive $I_2$ molecules with the 800 nm probe beam, comparison of focused and unfocused electrodes. The sharp line generated by ionization from the effusive molecular beam serves as an indication of the right voltage, a wrong ratio of repeller to extractor voltage will result in a distorted image (right)

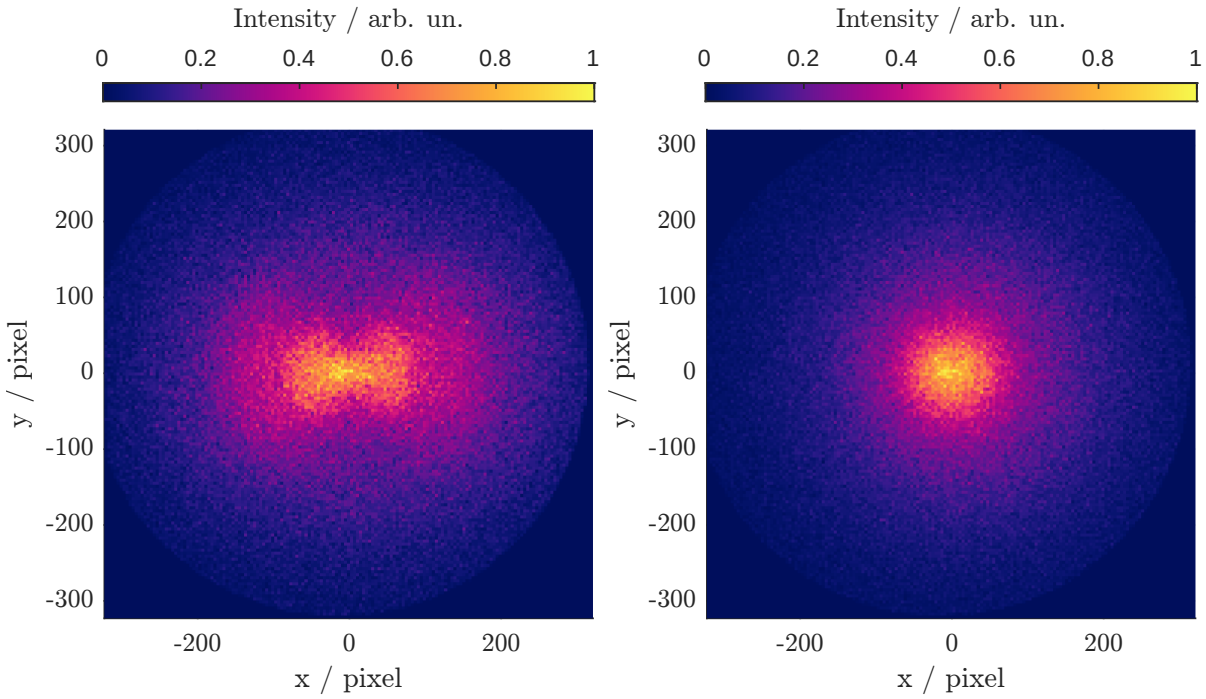


(a) Polarization in the detector plane

(b) Polarization normal on detector plane

Figure 2.21: 2D image of ions generated by photodissociation of $I_2$ molecules inside helium nanodroplets with the 800 nm probe beam. The laser polarization needs to be in the detector plane (left) to measure a conclusive velocity distribution, otherwise this results in a 2D-Gaussian distribution (right)

### 2.3.6 Pump-probe experiments

For rough spatial overlap, both pulses are focussed on the camera (camera in probe focus), and the pump beam is moved so that it is on top of the probe. The foci are set up so that the pump focus is much larger than the probe focus using a combination of the telescope in the probe path and the distance of the 25 cm focusing lens from the chamber. For finetuning the pump beam is moved while optimizing for maximum signal.

Figure 2.22 shows the temporal overlap between the 690 nm pump and 800 nm probe, effusive (a) and with He (b) as measured with the Time-of-Flight detector. At $t = 0$ the cross-correlation signal of pump and probe is visible. Figure 2.23 depicts the temporal overlap of 600 nm pump wavelength, captured with the VMI detector and integrating over 240 frames (approx 55 fps). In the effusive measurement, the step from negative to positive time delays shows the stability of the B state, this increased signal on positive delays can be observed over the whole stage - more than 200 ps. This is shown in figure 2.24, where the stage is moved over its whole range of motion, and the pump-probe signal stays at a very high level compared to the negative time delays (probe before the pump).

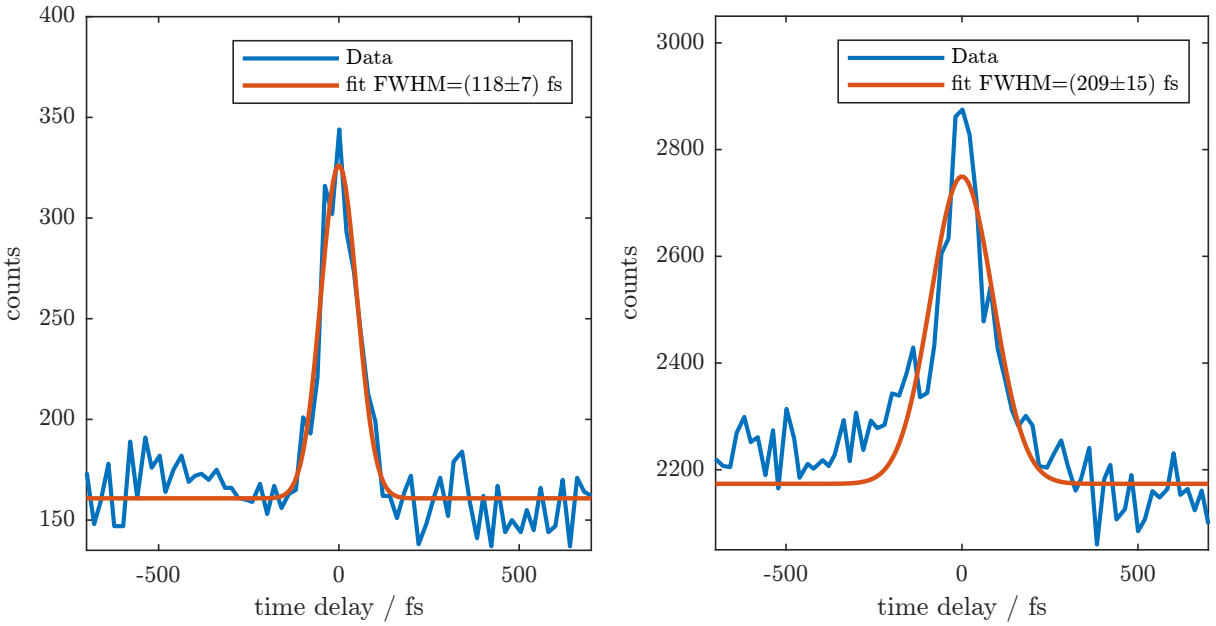


(a) Effusive $I_2$ molecules

(b) $I_2$ molecules inside helium nanodroplets

Figure 2.22: ToF detection of pump-probe generated ions of $I_2$ at 690 nm pump wavelength for effusive molecules and molecules solvated in helium nanodroplets with varying time-delay between pump and probe pulse

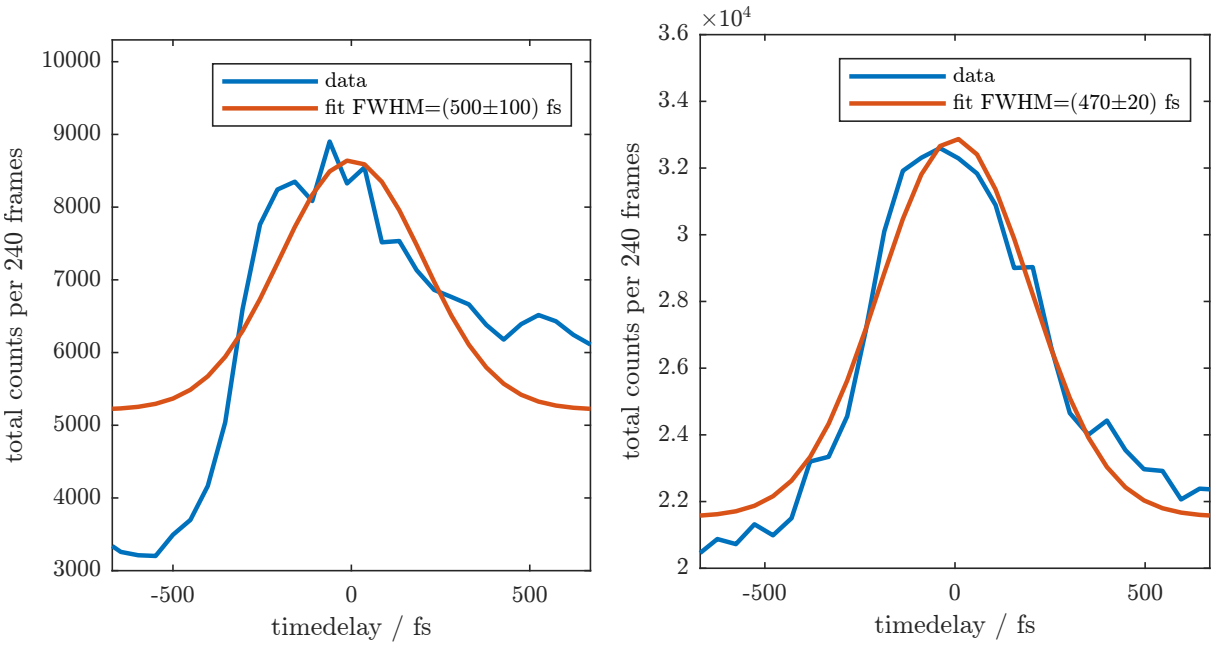


(a) Effusive $I_2$ molecules

(b) $I_2$ molecules inside helium nanodroplets

Figure 2.23: ToF detection of pump-probe generated ions of $I_2$ at 600 nm pump wavelength for effusive molecules and molecules solvated in helium nanodroplets with varying time-delay between pump and probe pulse

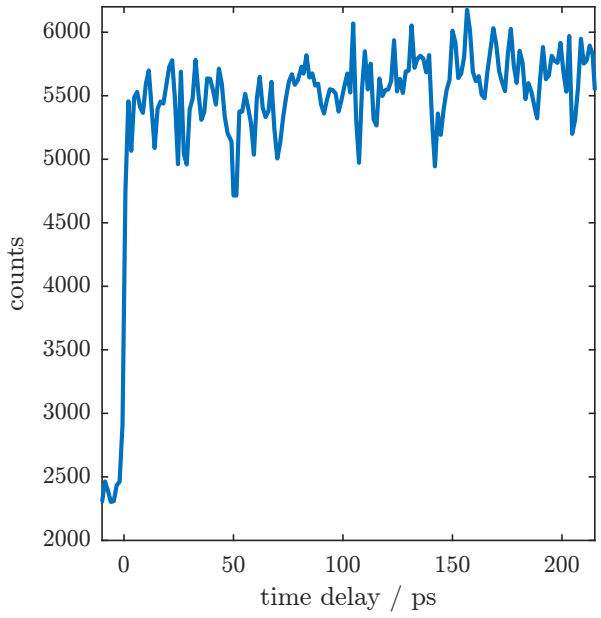


Figure 2.24: ToF detection of 600 nm pump 800 nm probe generated ions from effusive $I_2$ molecules, delay scan over the whole stage showing the stability of the B-state

# 3 Results

## 3.1 Isolated $I_2$ molecules

Before analyzing the properties of $I_2$ in superfluid helium, the photoexcitation dynamics in the gas phase were studied - both in the dissociative A-state and the bound B-state (see the potential energies in figure 1.1). By detecting the photofragments the validity of the detection can be verified - and the results compared with the literature since this process is quite well known. For these experiments the MCP gate was set up so that only $I^+$ ions are detected, and the laser polarization was in the plane of the detector.

### 3.1.1 A-state photodissociation

With an excitation wavelength of 690 nm, the dissociative A-state can be reached - the iodine molecule $I_2$ undergoes photodissociation into two ground state iodine atoms I+I. To follow the dynamics of the photodissociation, the time delay between pump and probe pulse was varied between 1 ps and 300 ps. The measurements were all taken with 12000 frames, the pump-only contribution was not measured separately since it led to a negligible signal. Probe-only measurements on the other hand were taken, and subtracted from the pump + probe measurement to show only the dynamics that are generated by a pump-probe measurement. The pump pulse power was set to 167 mW, and the probe pulse power to 1.52 W. An achromatic lens doublet with a focal length of 300 mm was inserted in the beam path. For further information on the measurements see lab book on 09.03.2023 (measurements 86-91).

The resulting images are shown in figure 3.1, the original data was reduced by binning over blocks with a size of 4x4 pixels. Within the first picosecond, a large positive signal appears in the center, and the image remains unchanged for later time-delays. A negative structure fitting the probe-only contribution can be seen at larger radii.

Figure 3.2 depicts the radial distributions with a calibrated velocity axis on top without normalization for the different time-delays, again not showing any major differences or trends. The radial distributions were smoothed with a moving mean over 8 data entries.

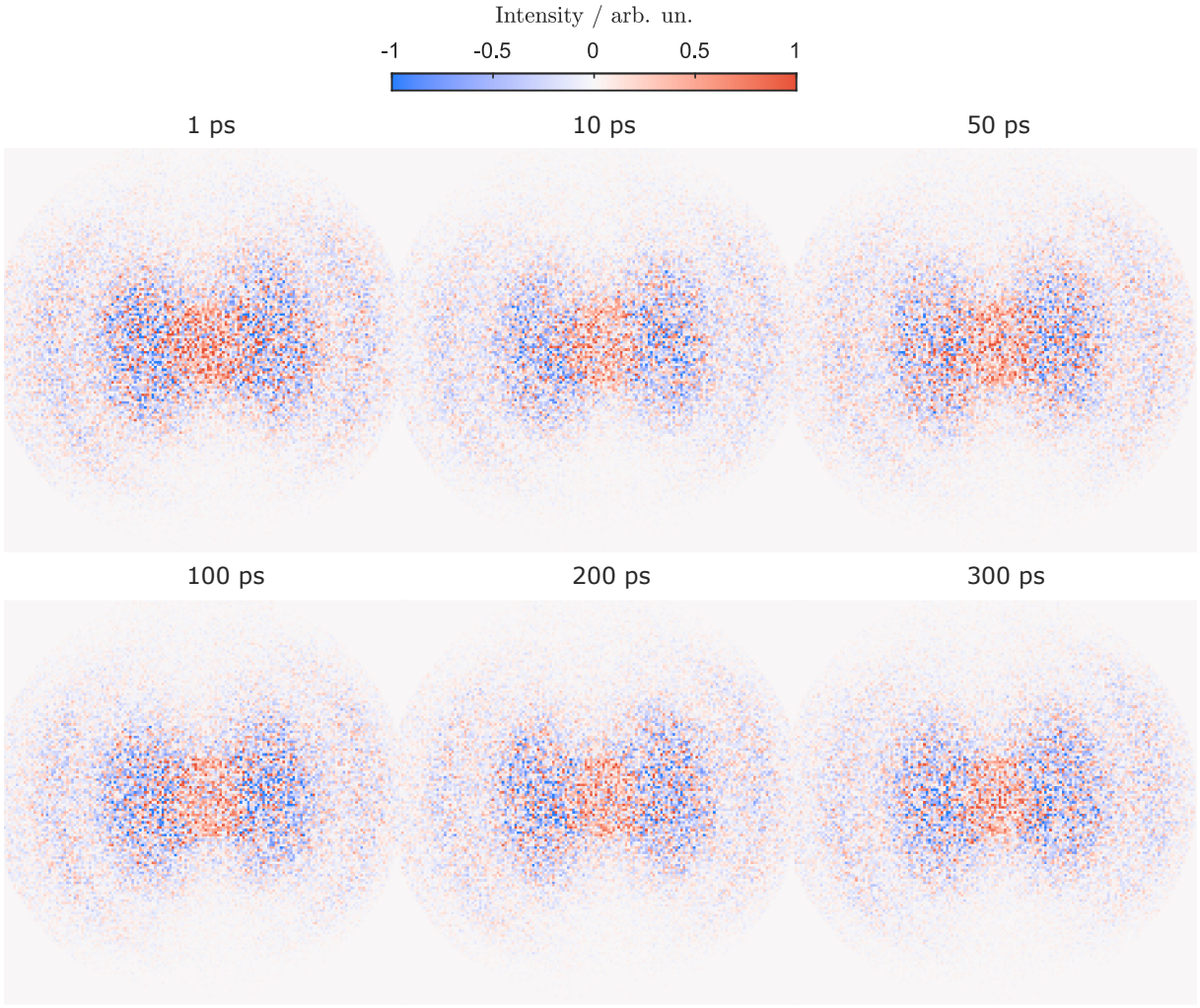


Figure 3.1: 2D velocity map images of $I^+$ ions generated by photodissociation followed by probe pulse ionization of effusive $I_2$ molecules via the A-state with varying time delay from 1-300 ps

Since the dynamics seem to happen only in the first picosecond, the images from 1 ps to 300 ps were summed up to generate a mean image (corresponding to a long measurement with 72000 frames) - see figure 3.3. The radial plot b also includes the inverted probe-only pulse (scaled so it fits the pump-probe data in the region of the Coulomb peak, 200 px to 300 px) which shows that the negative signal follows the same structure as the probe only. The pump depopulates the ground state from which the probe only normally excites, leaving less population for the probe - resulting in this ground state bleach. The orange line shows the scaled probe only added to the pump-probe signal. To the VMI image on the left the scaled probe-only image was added as well.

After normalization, the expectation value for the velocity can be calculated as 465 m/s and the most probable escape velocity amounts to 390 m/s.

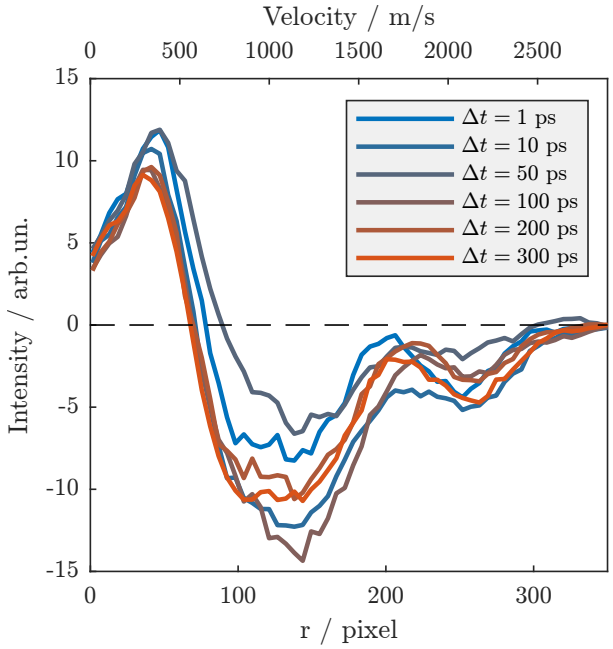


Figure 3.2: Radial distributions of $I^+$ ions generated by photodissociation followed by probe puls ionization of effusive $I_2$ molecules via the A-state with varying time delay between pump and probe from 5-300 ps

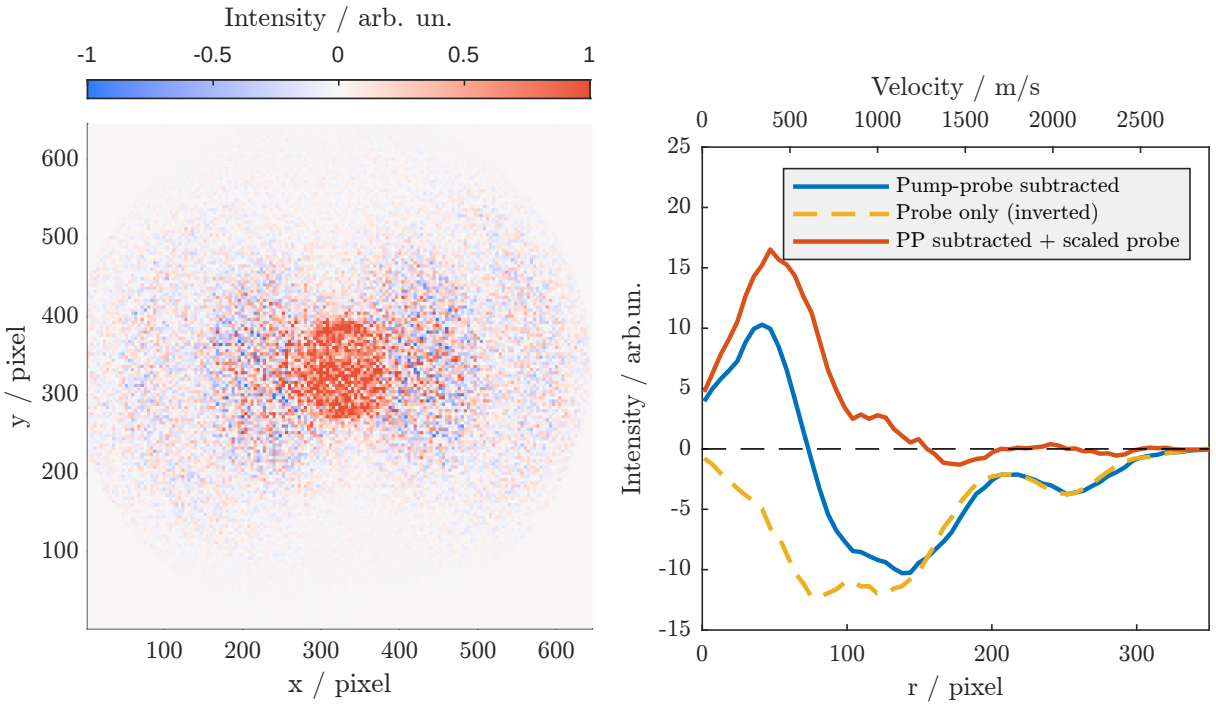


(a) Mean processed image

(b) Radial distributions

Figure 3.3: Mean velocity map image and radial distribution of $I^+$ ions generated by photodissociation followed by probe pulse ionization of effusive $I_2$ molecules via the A-state. Comparison with scaled and inverted probe only ground state ionization and addition of scaled-probe only

After applying a Gaussian smooth to the data, this mean image was Abel transformed - see figure 3.4. The generated rings on the outside are an artifact stemming from the noise in the region of the bleach. What is notable here is the structure at the center, namely the two connecting rings. These are normal to the pump and probe laser polarization, for the transition dipole moment of the A-state is normal to the molecular axis. Therefore the pump selects the molecules that are oriented vertically (when looking at the 2D image), and these molecules preferably dissociate in the y-direction.

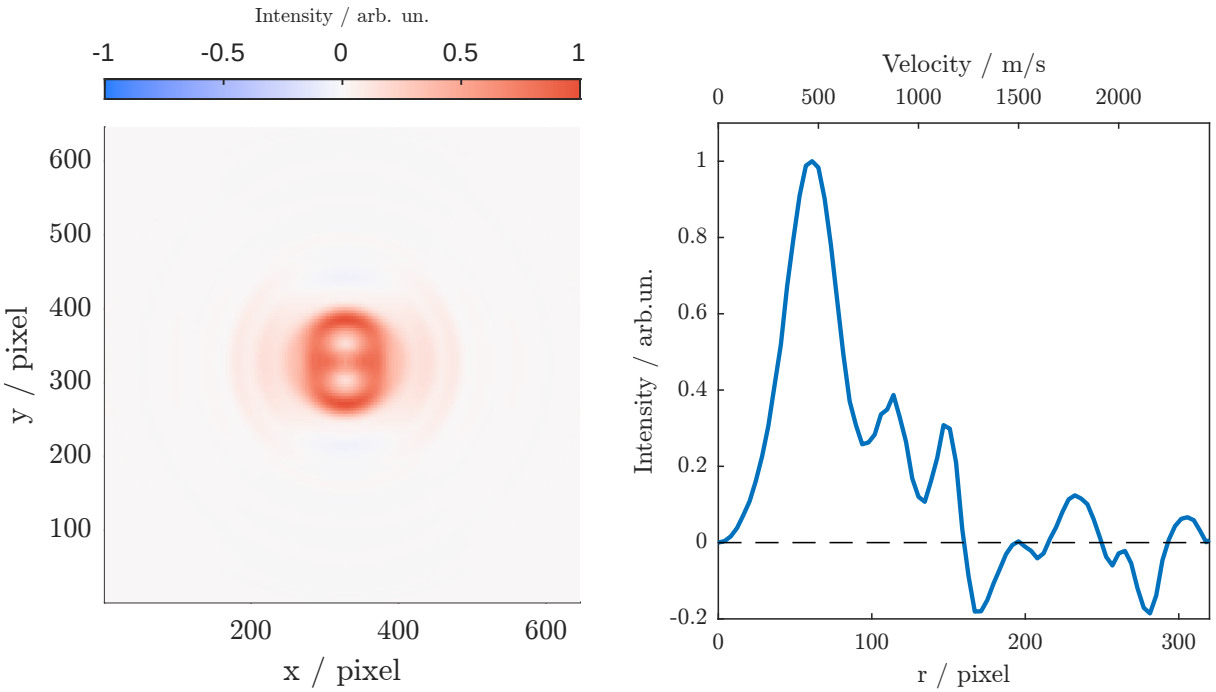


(a) Abel transformed image

(b) Abel transformed radial distribution

Figure 3.4: Abel transformed 2d velocity map image and radial distribution of $I^+$ ions generated by photodissociation followed by probe pulse ionization of effusive $I_2$ molecules via the A-state

The Abel transformed radial distribution has a peak at $(455 \pm 5)$ m/s, this matches the expected kinetic energy release upon 690 nm excitation is 0.247 eV - giving each dissociating atom a velocity of 433 m/s. The velocity map image in figure 3.3 and it's Abel transform show great similarities with a pump-probe measurement done by Lars Christiansen [23] with 680 nm pump, which is shown in figure 3.5.

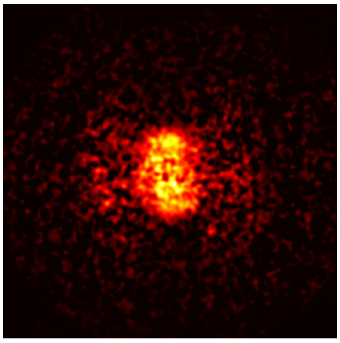

Figure 3.5: 2D image of $I^+$ ions generated by photodissociation followed by probe pulse ionization of effusive $I_2$ molecules via the A-state, 680 nm pump pulse 2.6 ns before the 800 nm probe pulse. Image taken from Lars Christiansen's dissertation [23]

### 3.1.2 B-state Coulomb peak shift

A wavepacket is generated in the B-state by pumping with 600 nm, and after a time-delay of 1 ps the high-powered probe puls can Coulomb explode the molecule from the B-state (as opposed to from the ground state as it was done for the energy calibration in section 2.3.2). Due to a larger internuclear distance of the molecule in the B-state, the ion velocities generated by Coulomb explosion will be lower compared to the ground state. The probe power was set to 445 mW and the pump power to 140 mW. For more information see lab book non 08.03.2023

Figure 3.6 shows that the Coulomb explosion peak in the radial spectrum is shifted to (230 ± 5) pixel, which corresponds to (1790 ± 30) m/s. The data has received additional Gaussian smoothing to reduce the noise before the Abel inversion.

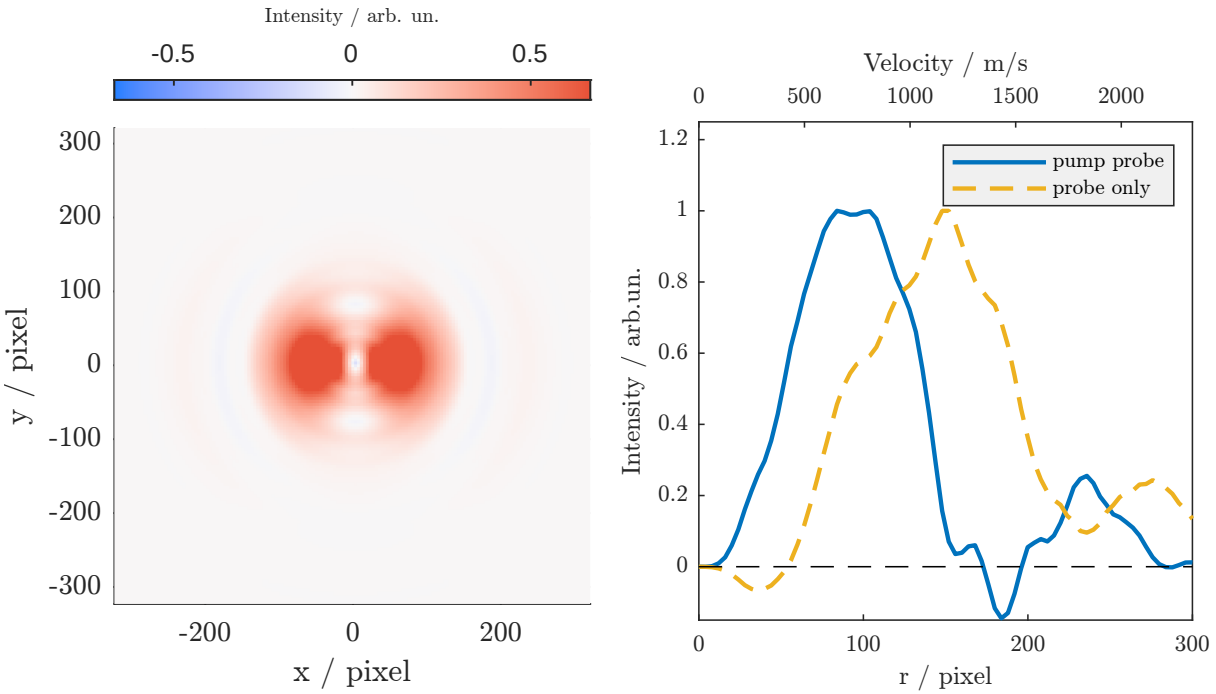


(a) Abel transformed image

(b) Abel transformed radial distribution

Figure 3.6: Abel transform 2d velocity map image and radial distribution of $I^+$ ions generated by Coulomb explosion followed by probe pulse ionization of effusive $I_2$ molecules in the B-state, radial distribution compared with ground state Coulomb explosion (probe only)

According to the potential energy surfaces shown in figure 1.1 to internuclear distance should be between 2.7 $\AA$ and 3.4 $\AA$ at the level of vibrational excitation that is reached with the 600 nm pulse.

With the same calculation as was done for the energy calibration (see equation 2.9), the mean atomic separation of the iodine molecules during Coulomb explosion can be estimated to (3.0 ± 0.2) $\AA$ by inserting the velocity at the peak of the shifted Coulomb peak ((1790 ± 30) m/s). This is the equilibrium distance of the B-state, as can be seen in figure 1.1

### 3.1.3 B-state electrons

As introduced in section 2.3.4, the VMI can also be operated in electron mode, to record kinetic energy spectra. The energies were calibrated using a probe only measurement with the fundamental 800 nm output.

When exciting the iodine molecule into the B-state with a 600 nm pump pulse, the ionization potential changes from 9.254 eV to 7.21 eV. A pump-probe measurement is shown in figure 3.7. Same as for the probe-only measurement, the data has been binned into bins of size 4x4 pixels, gaussian smoothed, and then Abel inverted. For the raw measurement see appendix (figure 6.4). An ionization with 5 (800 nm) photons gives an excess energy of 0.535 eV - thus explaining the intensity at and around the center. One photon more leads to a kinetic energy of 2.084 eV, coinciding with the peak at 2 eV . Other rings that may be visible are artifacts from the Abel inversion, and stem from the noise in the raw measurement.

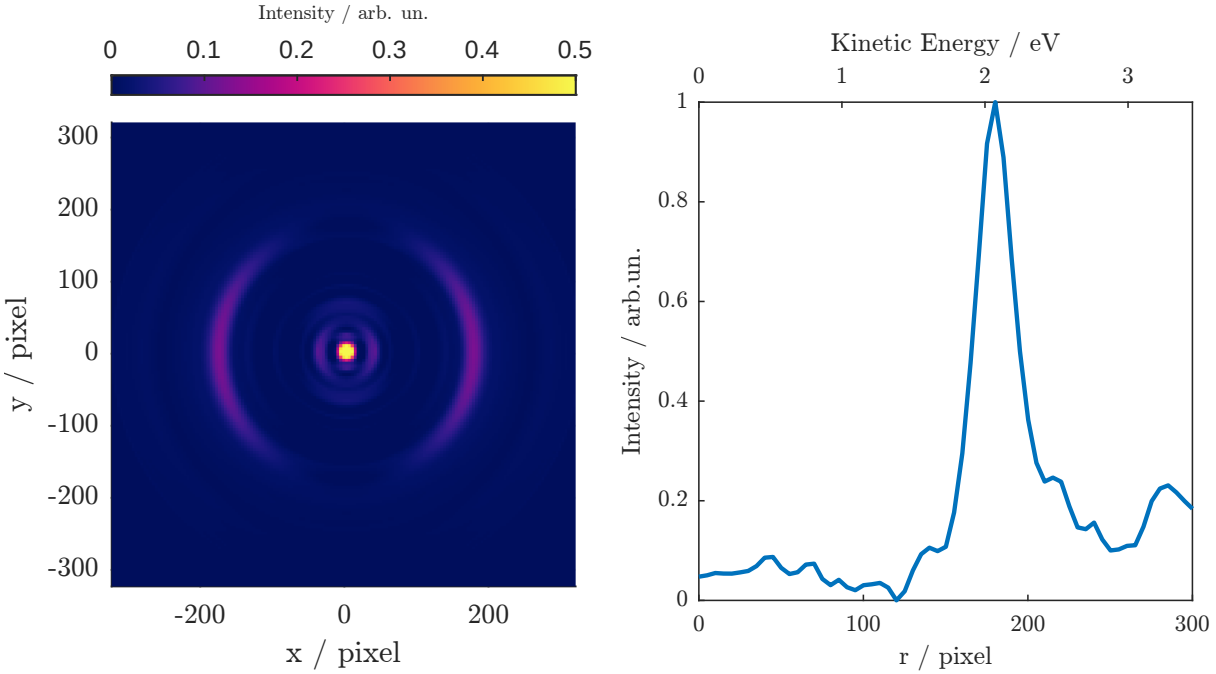


(a) Abel transformed image

(b) Radial distribution

Figure 3.7: Abel transformed 2d velocity map image and radial distribution of electrons generated by ionization of effusive $I_2$ in the B-state with 600 nm pump

## 3.2 $I_2$ molecules inside helium nanodroplets

After $I^+$ ions generated by photodissociation from gas phase $I_2$ were detected with the VMI, the next step was the analysis of ions emerging from superfluid helium nanodroplets after photodissociation. The droplets are produced by supersonic expansion through a cooled nozzle, as described in section 1.4. For these measurements, a helium pressure of 25 bar was applied - and the nozzle was always cooled to its lowest possible temperature (12.4 K at 25 bar). A significant factor for noise and background minimization was filling the cold traps with liquid nitrogen, which vastly improved the ratio between signal from inside the helium droplets to signal originating from effusive molecules. The effusive contribution was measured and subtracted for each helium measurement, showing only the dynamics of molecules solvated in helium droplets. Through optimization the best pickup conditions have been found to increase the signal from molecules inside the helium nanodroplets. A sample QMS measurement for all the relevant masses can be found in section 6.1 figure 6.1. Moreover, the probe focus is moved so that the signal from the $IHe_N$ mass peaks is maximized, which corresponds to the signal that has to come from inside the droplets since it does not exist for gas phase iodine.

### 3.2.1 A-state photodissociation

The photodissociation of molecular iodine through the A-state that was observed for isolated molecules (section 3.1.1), and the emergence of the ions from the droplets could be measured. Again the time delay between the pump and probe pulse was varied to show the dynamics between 5 ps and 300 ps. The MCP was gated on the $I^+$ mass with a window of 0.5 $\mu$s. The pump pulse power was set to 150 mW, and the probe pulse power to 500 mW. The achromatic doublet lens with a focal length of $f = 250$ mm was inserted into the beam path. For further information on the measurements see lab book on 10.03.2023 (measurements 109-114).

The resulting VMI images are shown in figure 3.8. The raw data was reduced by binning over blocks with a size of 2x2 pixels. In addition to that, due to the background noise that stems from the subtraction of effusive as well as pump and probe-only measurements, gaussian smoothing was applied to the data. The images with delays of 5 ps to 75 ps were taken by integrating over 12000 frames, the image at 300 ps time delay was integrated over 96000 frames. Pump-only and probe-only contributions were measured and subtracted from the pump + probe measurement - resulting in the images below. As introduced in section 3.1.1 the scaled probe-only contribution was added to the pump-probe data, as to compensate the probe bleach. For the helium measurement, no Coulomb peak can be observed, but it was assumed that the negative contribution for high radii ($r > 280$ pixel) is generated by Coulomb explosion with the probe beam. As shown in figure 3.9a, the individual probe data for every measurement was scaled by dividing by the sum of hits for $r > 280$ pixel. Shown in the image is only the mean inverted and scaled probe.

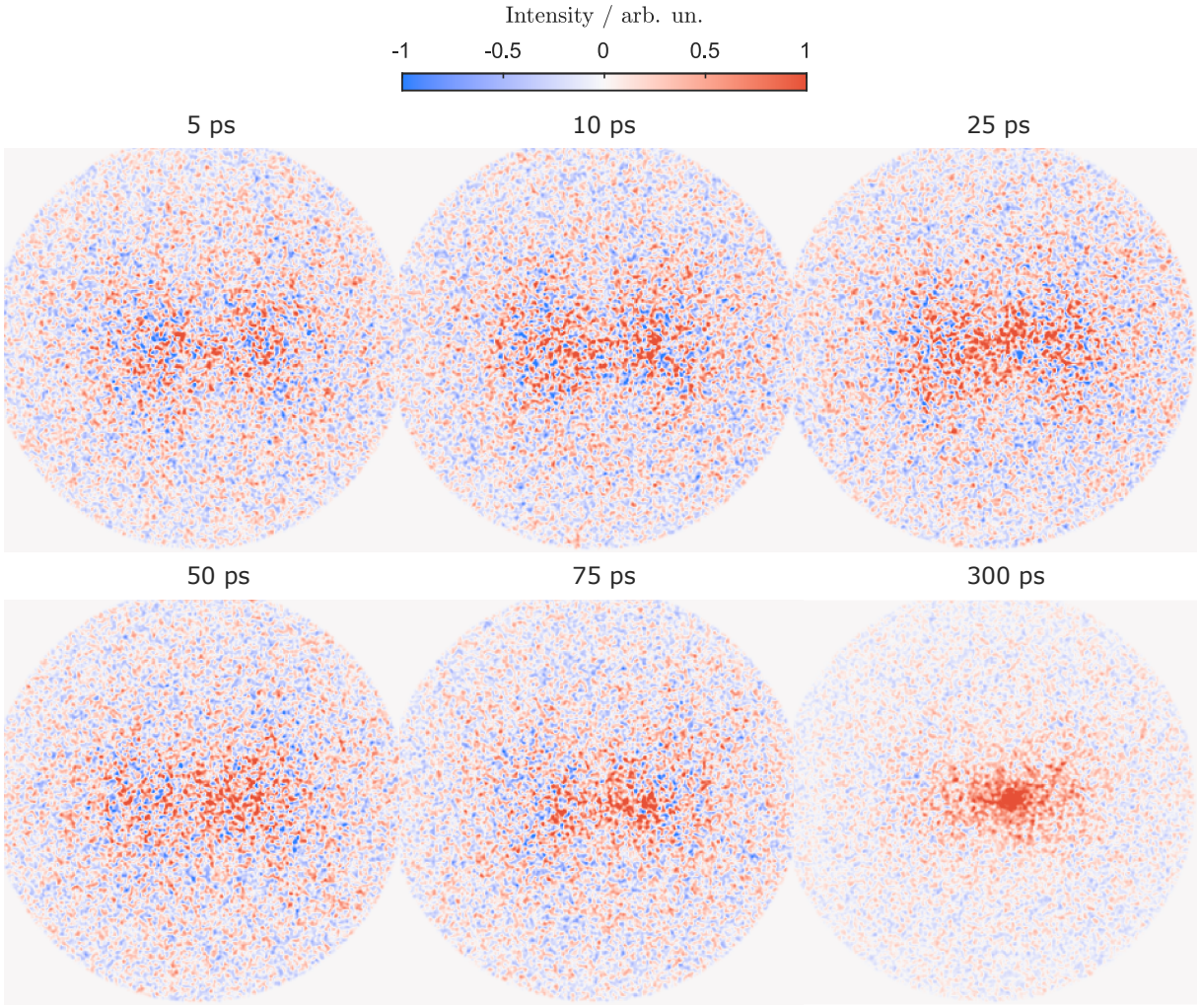


Figure 3.8: 2D velocity map images of $I^+$ ions generated by photodissociation followed by probe pulse ionization of $I_2$ molecules inside helium nanodroplets via the A-state with varying time delay from 5-300 ps

The angular-integrated data for all time delays is shown in figure 3.9a, alongside the inverted (and scaled) probe-only measurement. The data has been smoothed by applying a moving mean with a size of 20 data entries. This shows the trend of increasing ion signal at low velocities with the peak at approximately 470 m/s. This is overshadowed by the negative signal generated by the ground state bleach (similar to the result in the effusive molecules). In figure 3.9 the scaled probe has been added to the pump-probe signal to account for the ground state bleach. Scaling the probe to all radii larger than 280 pixels is not ideal here, since it does not completely eliminate the bleach without blowing the probe only up manually. Still, there can be observed that for later time delays more signal appears, and this is also shifted to lower velocities.

Figure 3.10 depicts the expectation value $E(v)$ and the mode (most probable value) of the escape velocity compared to the same values for the effusive measurement. Both values are higher in helium than for isolated molecules, independent of the time delay. What is more, there seems to be a trend to lower velocities for later times.

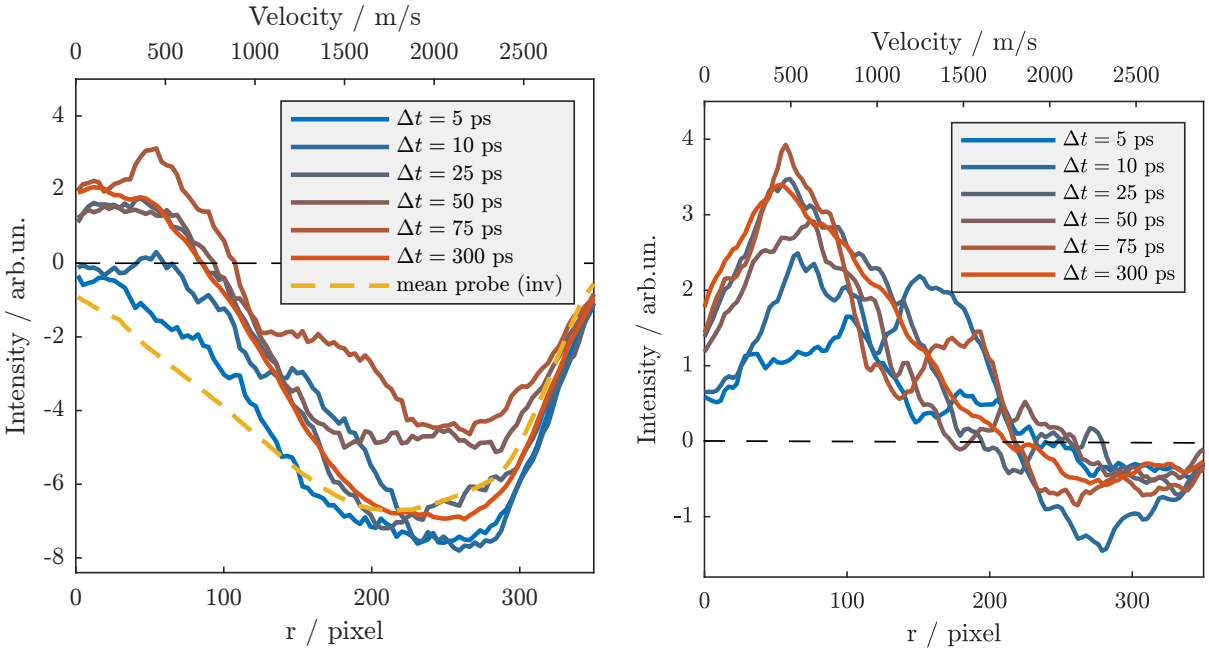


(a) Pump probe subtracted

(b) Addition of (individual) scaled probe

Figure 3.9: Radial distributions of $I^+$ ions generated by photodissociation followed by probe pulse ionization of $I_2$ molecules inside helium nanodroplets via the A-state with a varying time delay from 5-300 ps. Comparison with mean scaled and inverted probe only ground state ionization.

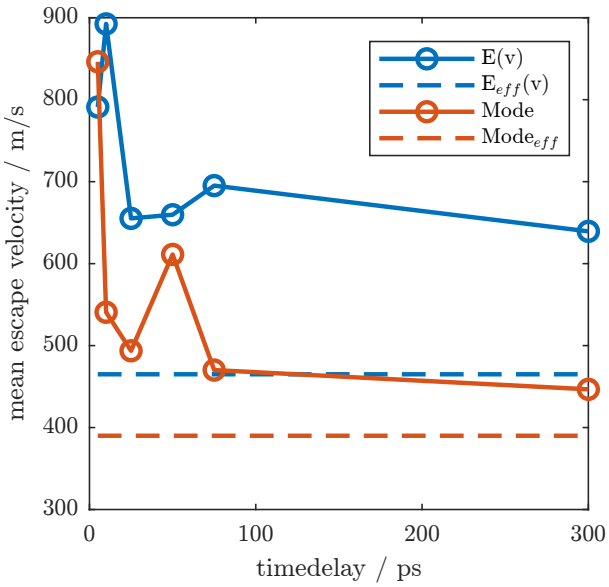


Figure 3.10: Most probable (mode) and mean escape velocity $E(v)$ of the ions generated by A-state photodissociation inside helium droplets

### 3.2.2 B-state predissociation

The B-state shows very long lifetimes in the gas phase, but this can change vastly when the molecule is in solution - as already discussed in sections 1.2 and 1.3. After the process of exciting in the dissociative A-state - which generates two iodine ions, has been observed in the gas phase as well as in superfluid helium nanodroplets, the excitation of the B-state of iodine solvated in helium could be studied. The basic measurement parameters were the same as for A-state measurements in helium. The MCP was gated on the $I^+$ mass with a window of 0.5 $\mu$s, the pump pulse power was set to 150 mW, and the probe pulse power to 500 mW. The achromatic doublet lens with a focal length of $f = 250$ mm was inserted in the beam path. The time delay between the pump and probe pulse was varied to show the dynamics between 10 ps and 200 ps. For further information on the measurements see the lab book on 10.03.2023 (measurements 116-118).
Figure 3.11 shows pump-probe velocity map images for time delays of 10, 100, and 200 ps. All images are scaled to their maximum value. The data has been binned into segments of 2x2 pixels (half the original size) and a Gaussian smooth filter applied. Again the scaled probe-only image was added in retrospect to eliminate the ground-state bleach.

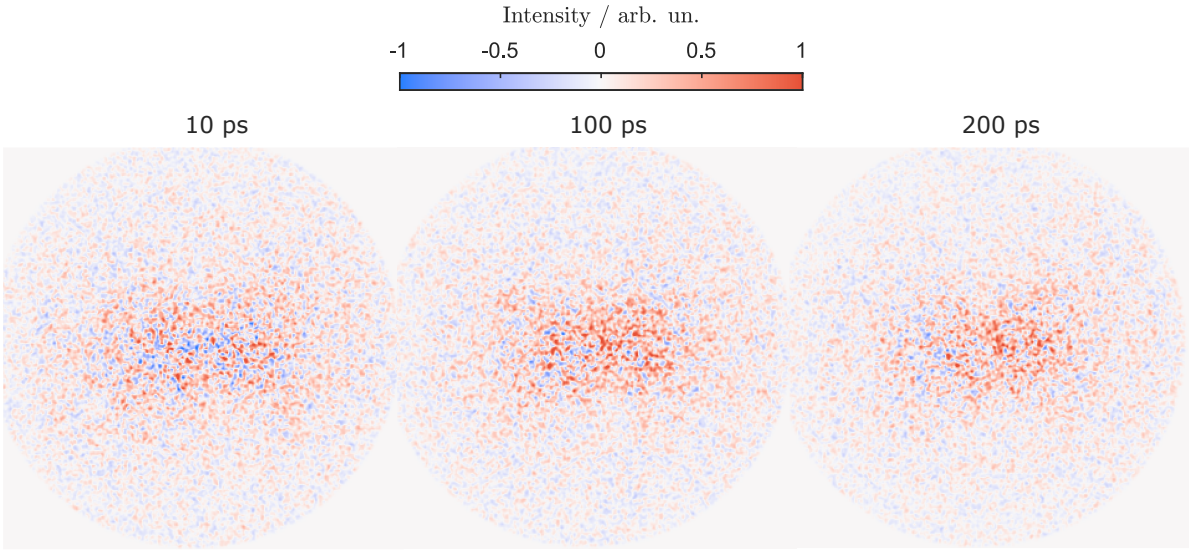


Figure 3.11: 2D velocity map images of $I^+$ ions generated by predissociation followed by probe pulse ionization of $I_2$ molecules inside helium nanodroplets via the B-state with a varying time delay from 10-300 ps. Addition of scaled probe only contribution

The radial distributions for the three time-delays are shown in figure 3.12a, in yellow the mean inverted and scaled (to radii larger than 250 pixels) probe-only measurement. In figure 3.12b the scaled probe only has been added to the pump-probe data - these distributions now correspond to the images in figure 3.11. The data has been smoothed by a moving mean with a size of 16 data points. Most probable (mode) and mean escape velocity $E(v)$ of the ions depending on time-delay are shown in figure 3.13. For a time delay of 10 ps between pump and probe, all of the subtracted signal is negative, as can be seen in figure 3.12a. After the addition of the individual scaled probe-only data the main contribution comes from higher velocities, with the expectation value at 1200 m/s. This can also be seen in the velocity map image in figure 3.11 where at the center there is mostly noise and positive contributions come mainly from a ring at around 120 pixels. This changes when increasing the time delay to 100 ps, where even for the subtracted data a small positive contribution was measured at small radii. After the addition of the scaled probe, this shows itself by a large positive signal from the center, and the expectation value of the ion velocity decreases to 960 m/s. This trend continues for longer time delays, at 200 ps the positive signal at the center further increases, and $E(v)$ is further lowered to 950 m/s.

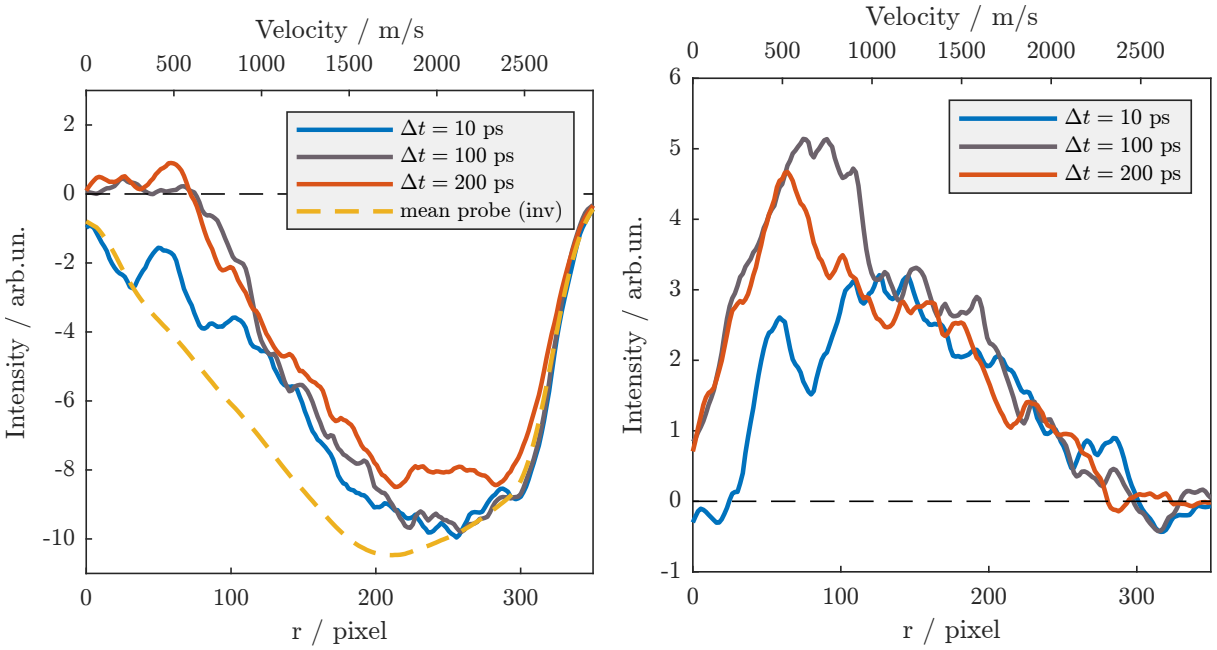


(a) Pump probe subtracted

(b) Addition of (individual) scaled probe

Figure 3.12: Radial distributions of $I^+$ ions generated by predissociation followed by probe pulse ionization of $I_2$ molecules inside helium nanodroplets via the B-state with a varying time delay from 10-300 ps. Comparison with mean scaled and inverted probe only ground state ionization.

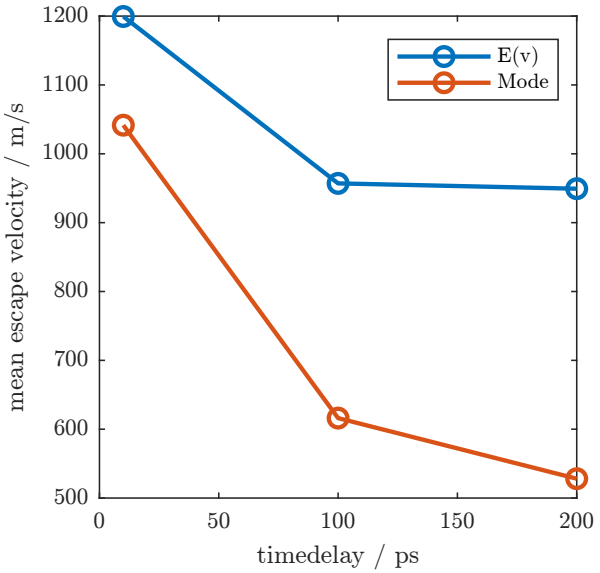


Figure 3.13: Most probable (mode) and mean velocity $E(v)$ of the ions generated by B-state predissociation inside droplets

## 3.3 Comparison

### 3.3.1 A-state for $I_2$ molecules in gas phase and inside helium nanodroplets

Figure 3.14 shows the radial distributions (with added probe only) for the mean effusive measurement in section 3.1.1 and measurements in helium droplets with time-delays of 10, 50, and 300 ps. All distributions have been called to their maximum value, a direct comparison of signal intensity is not conclusive since there is much more signal from effusive molecules. The velocity distributions inside helium nanodroplets are much broader than for isolated molecules, especially for short time-delays. With increasing time-delay the distributions of molecules inside helium droplets approach the gas phase measurement - as shows the measurement with 300 ps time-delay.

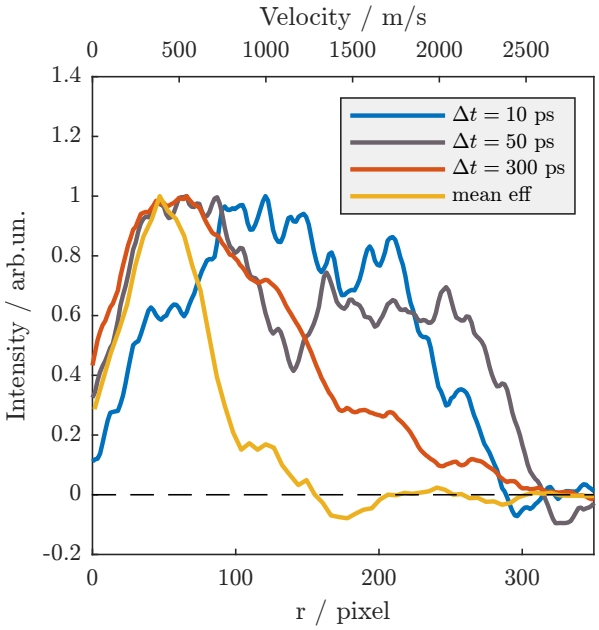


Figure 3.14: Comparison of A-state photodissociation of $I_2$ molecules in gas phase (yellow) and inside helium nanodroplets with three different time-delays (10,50 and 300 ps) between pump and probe pulse

This can be an indication of initial confinement leading to higher Coulomb repulsion, then drift and deceleration of the molecules inside the droplets reduce the observed ion velocities.

### 3.3.2 A-state and B-state inside helium nanodroplets

The results from excitation into the B-state and the A-state show similar trends but with differences in signal strength and measured ion velocities. Figure 3.15a shows the radial distribution for the A-state at 300 ps time delay and the B-state at 200 ps time delay, both scaled so that the regions with $r > 250$ pixels overlap with the mean scaled and inverted probe only. This should account for different measurement parameters like laser power and pickup conditions. In figure 3.15b the scaled probe-only contributions have been added to the subtracted data.

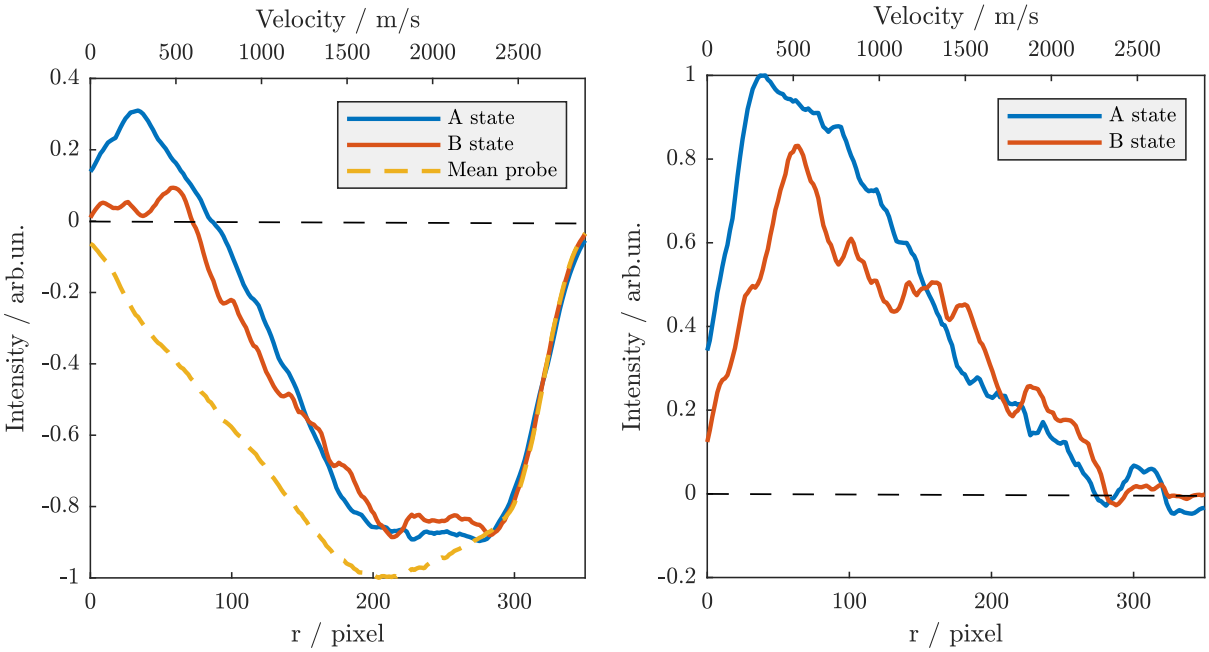


(a) Pump probe subtracted

(b) Addition of (individual) scaled probe

Figure 3.15: Comparison of A-state (300 ps time delay) photodissociation and B-state (200 ps time delay) predissociation of $I_2$ molecules inside helium nanodroplets

The spectra have a similar structure, but the total number of ions detected (amount of positive signal) is higher for the A-state photodissociation than for the B-state predissociation. Moreover, the B-state ions appear at higher velocities. The peak in the velocity distribution of the B-state is at 520 m/s, compared to 310 m/s for the A-state. This also shows itself in the comparison of figure 3.10 and figure 3.13, where both the expectation values and modes are higher for B-state measurements.

# 4 Discussion

The main objective of this master's thesis was to understand the dynamics of molecular iodine inside superfluid helium nanodroplets, in particular the predissociation of the bound B-state. Before setting up the experiments, an investigation into the existing literature regarding iodine in the gas phase and solution was conducted - ranging back to research done by Nobel prize winner Ahmed Zewail in the 1980s.

The research summarized in chapter one allows drawing the conclusion that on the one hand, an excitation in the bound B-state of isolated (gas phase) iodine molecules exhibits very long lifetimes - with little to no decay on the molecular timescales of femtoseconds to picoseconds. Although a small nonzero probability for conversion to a lower excited state exists, it takes much longer times for this to take a noticeable effect on the population in the B-state. On the other hand, this probability can (sometimes greatly) increase if the molecules are surrounded by a solvent. Iodine-solvent collisions can induce a coupling to a repulsive potential and the excited state population decays nonradiatively. This results in the dissociation of the molecule below the dissociation limit - thus termed predissociation. Experiments showed that the predissociation of iodine can happen within several hundreds of femtoseconds depending on the solvent and pressure. [13, 18, 30, 31] Theoretical descriptions including quantum mechanical hybrid strategies calculating the predissociation of various molecules underline these experiments. [12, 19, 20] Early time-of-flight measurements at our lab indicated that this could also be the case for iodine solvated in superfluid helium - an in principle low-interacting environment regarding nuclear dynamics. [6, 7]

To study these molecular dynamics, a VMI spectrometer was integrated into the existing vacuum setup of Femtolab at Graz University of Technology to apply time-resolved ion imaging spectroscopy. The spectrometer was set up and its basic measurement parameters were optimized to ensure sensible operation. Before measurements of the B-state predissociation, the dissociative A-state of iodine was examined experimentally. An excitation into this state with 690 nm pump wavelength produces two ground state iodine atoms which can be detected by the VMI detector, therefore an ideal system to verify the ion detection both for gas phase and solvated molecules.

## 4.1 Isolated $I_2$ molecules

A probe-only measurement of gas-phase iodine made the calibration of the detector possible due to the distinct dissociation velocity of ions generated by Coulomb explosion (figure 2.13). This allows us to draw more meaningful conclusions from the angular integrated radial data.

A 690 nm pump pulse followed by an 800 nm probe puls showed the dynamics (or the lack thereof) of the A-state. Varying the time-delay between pump and probe pulse from 1 ps to 300 ps showed no significant change, thus showing that the dissociation happens quickly in the first picosecond. This fits the results of a different molecule by Kobayashi et al.[44], namely the photodissociation of IBr within 150 fs. The velocity map image in figure 3.3 (and Abel inverted figure 3.4) show great similarities with measurements by Lars Christiansen (figure 3.5 [23]), a good indication that the detection works sufficiently. The negative signal in these measurements stems from a ground state bleach, which is generated by the depopulation of the ground state by

the pump pulse, resulting in less available population for the probe pulse compared to the probe only measurement. This was compensated by adding the probe only contribution scaled to the Coulomb peak (a peak in the velocity distribution attributed to Coulomb explosion). This peak serves as an indicator of the number of molecules in the ground state. The resulting velocity distribution after addition (see figure 3.3) showed the most probable ion velocity at 390 m/s, and an expectation value of 465 m/s.

Excitation into the B-state in gas phase leads to a very stable excited state population. A high-intensity probe pulse can then Coulomb explode the excited molecule. The associated peak in the radial distribution then shifts compared to the ground state Coulomb explosion, as shown in figure 3.6. This was calculated back to the atomic separation at the moment of the ionization, which fits the equilibrium distance of the B-state. What is more, the detection of electrons was demonstrated, with a kinetic energy calibration and an electron spectrum of the B-state in figure 3.7.

## 4.2 $I_2$ molecules in helium nanodroplets

After ions of dissociating isolated iodine molecules could be detected with the VMI detector, the next step was the investigation of the dynamics happening inside the superfluid helium nanodroplets. Again first the dissociation upon excitation into the A-state was analyzed, followed by the predissociation of the B-state.

A timescan from 5 to 300 ps revealed the dynamics unfolding inside the droplets on molecular timescales. Initially, only a small amount of ions are detected, mostly at larger radii. This shifts for increasing timedelay, the amount of detected ions increases and their velocity decreases (see figure 3.10). This also matches with data by Lars Christiansen [23] for measurements of the B-state above dissociation. This can be explained by two possible scenarios:

1. Ionization of the ground state atoms happens after ejection from the droplet, and fast ions are measured first followed by slow ions
2. Ionization happens inside the droplets by Coulomb explosion, more time-delay leads to bigger atomic separation (and thus smaller Coulomb explosion velocities) due to drifting of the atoms inside the droplet

Assuming the decrease in velocities due to the first of the above-mentioned reasons, the measured ion velocities are a sample of only the fastest of the original velocities inside the droplet. If this was the case, the signal yield should also increase vastly for later time delays because more and more ions exit the droplet when increasing time delay. When analyzing figure 3.9 a this appears to be the case - as the total signal at small radii increases. However in 3.9 b, after the addition of the scaled probe this is less clear. Since the trend of the increasing signal should be rather large when assuming a velocity distribution around the final escape velocity - the process of ionization inside the droplets is more likely. It fits the decreasing Coulomb energy for increasing internuclear separation.

The ion velocities (both expectation value and mode), shown in figure 3.10 are higher than for isolated iodine molecules. Following the assumption of Coulomb explosion inside the helium droplets, leads to the conclusion that the separated atoms drift more slowly inside the droplets than upon dissociation in vacuum - thus being closer together at ionization.

The results gathered for excitation into the bound B-state are quite similar to the results of the A-state dissociation - strongly suggesting that the iodine molecule undergoes predissociation induced by the superfluid helium environment. The subtracted pump-probe data in figure 3.12a indicates a similar increase in signal at low radii, addition of the scaled probe (figure 3.12b)

reveals that the velocities decrease for larger time-delays, as shown in figure 3.13. Initially at 10 ps the most probable ion velocity is 1040 m/s, which drops to 530 m/s at 200 ps. Again likely due to larger internuclear separation which results in lower Coulomb energy upon ionization of both atoms. Ions can already be detected at 10 ps, compared with the stability in the gas phase this shows the vast influence of the helium environment on electronic dynamics in the iodine molecule. The predissociation induced by the helium-iodine collision allows quick depopulation of the bound state via one of the crossing dissociative states. Excitation with 600 nm compared to 690 nm provides the system with 0.2695 eV more energy, theoretically this results in a higher velocity of roughly 450 m/s for a single ion. At early times (5 ps for A-state and 10 ps for B-state) a difference in ion velocity expectation values of around 400 m/s was measured. The difference decreases slightly to 300 m/s for 200 ps time-delay in the B-state and 300 ps time-delay in the A-state which could indicate deceleration inside the droplets.

# 5 Conclusion

This study investigates the photoexcitation dynamics of molecular iodine in superfluid helium nanodroplets using a velocity map imaging (VMI) spectrometer. To achieve this, a VMI spectrometer was integrated into the existing setup, characterized and calibrated using the measurement of Coulomb explosion by multiple 800 nm photons (figure 2.13). Furthermore, the Abel inversion of the measurement data was analyzed.

The dynamics of isolated $I_2$ molecules were studied by applying a 690 nm pump pulse to populate the dissociative A-state and probing this system with an 800 nm pulse at varying time delays between the two pulses. The results indicate that the dynamics happen within the first picosecond, and the resulting velocity map image (see figure 3.3) is comparable to other sources. [23] The B-state equilibrium distance at $(3.0 \pm 0.2)$ $\mathring{A}$ was calculated using Coulomb explosion, an electronic spectrum from the B state with a peak at 2 eV was measured and a kinetic energy calibration with 800 nm excitation was performed.

$I_2$ molecules inside helium nanodroplets with temperatures below the superfluid phase transition showed different dynamics than effusive molecules. Pumping of the A-state led to an increase in total signal and a decrease in ion velocities with rising timedelay between 5 and 300 ps as shown in figure 3.8. The influence of the superfluid helium environment is largest for the B state, where lifetimes on the order of microseconds for isolated molecules contrast with a predissociation of the molecule at timescales similar to the A-state photodissociation. This is perceivable by detecting ions upon 600 nm excitation as shown in figures 3.11 and 3.12, where timedelay was varied between 10 and 200 ps, although at a lower yield and higher velocities than for the 690 nm excitation.

The findings lead to the conclusion that the weakly interacting helium environment, regarding nuclear dynamics, can significantly impact electronic dynamics. We found that a bound state for isolated molecules behaves like a dissociative state for molecules solvated in superfluid helium. This may have significant implications for superfluid helium droplets as a universal spectroscopy matrix.

## 5.1 Outlook

A more detailed investigation of the A-state dynamics within the first picosecond would be of profound interest, also depending on the intensity of the probe beam - and its implications on the signal stemming from the coulomb explosion.

What is more, remeasuring the dynamics of the B state and further examination of the predissociation regarding droplet sizes and kinetic energy release would be the next steps in this study. Since it is assumed that the ion signal arises in part from Coulomb explosion inside the droplets, the size of these droplets should have a significant impact on the velocities of the detected ions. Also here dependence on probe power should shine more light on whether it is still Coulomb explosion that is observed here. Moreover, other research suggests, that for ionization inside the droplets, most ions have one or several helium atoms attached, so the mass gate needs to be changed accordingly in order to detect those complexes. Most of the above-mentioned points are currently under progress, and we excitedly await the results of the research.

Naturally, since the operation of the VMI has been successfully demonstrated also the study of other molecules comes into reach - further investigation of femtochemistry inside helium nanodroplets, to get a step closer to the goal of observing isolated chemical reactions at their natural timescales.

# 6 Appendix

## 6.1 Iodine pickup conditions

Figure 6.1 shows a QMS mass table for all the relevant masses during the measruements. Iodine pickup is set so that a maximum of 254 u mass (iodine molecule) and 131 u mass (iodine atom + helium atom) is achieved. The signal vastly increases when introducing the helium droplet beam in the chamber, which can be seen at 2500 s in the graph. It usually takes a few minutes until the partial pressures are stable, then the measurement can begin - here at 3200 s. Opening and closing the valve to the source chamber gives the rise and falls in helium and iodine masses after 3400 s.

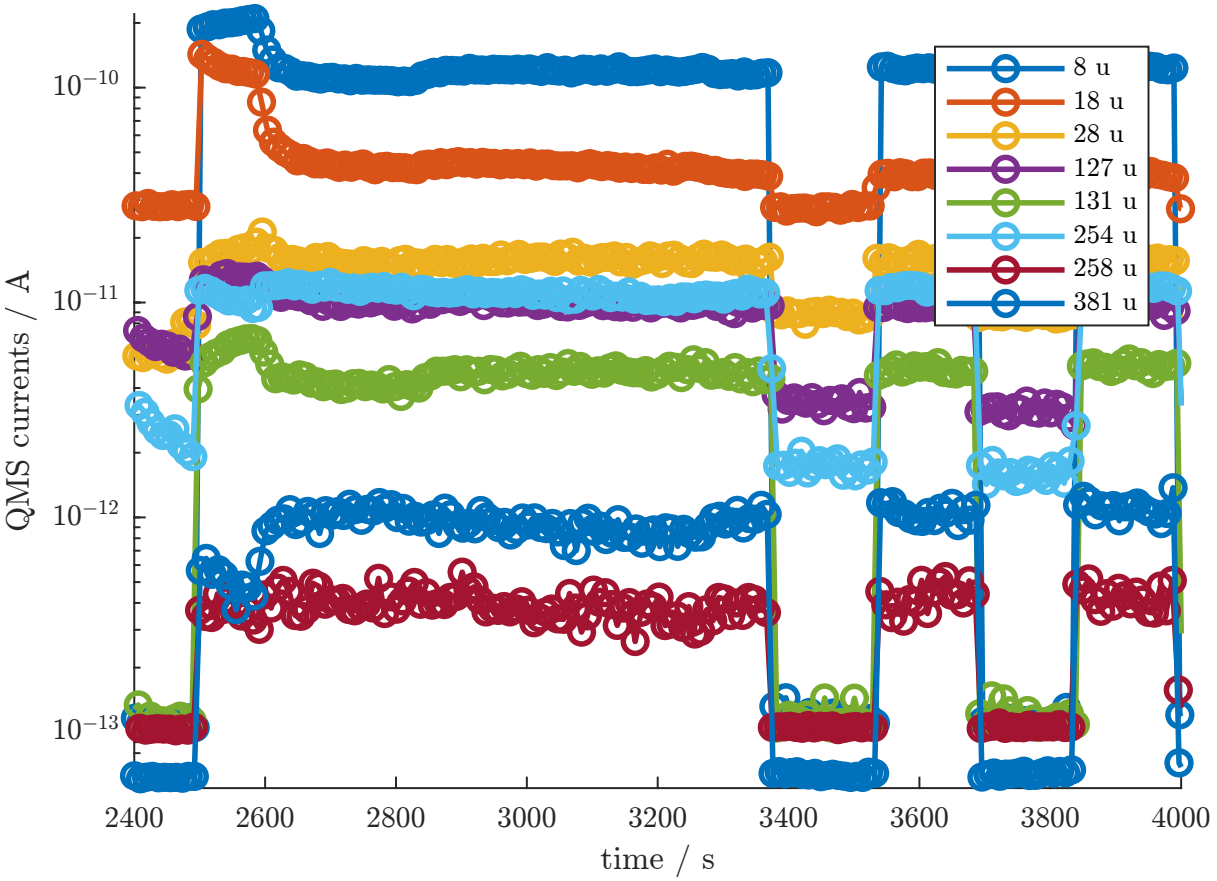


Figure 6.1: QMS mass table, time dependence of QMS current signals for relevant atomic masses during several measurements. Fast signal drop and increase is a result of closing and opening the valve to the source chamber (blocked or passing through helium beam)

## 6.2 B state coulomb peak shíft

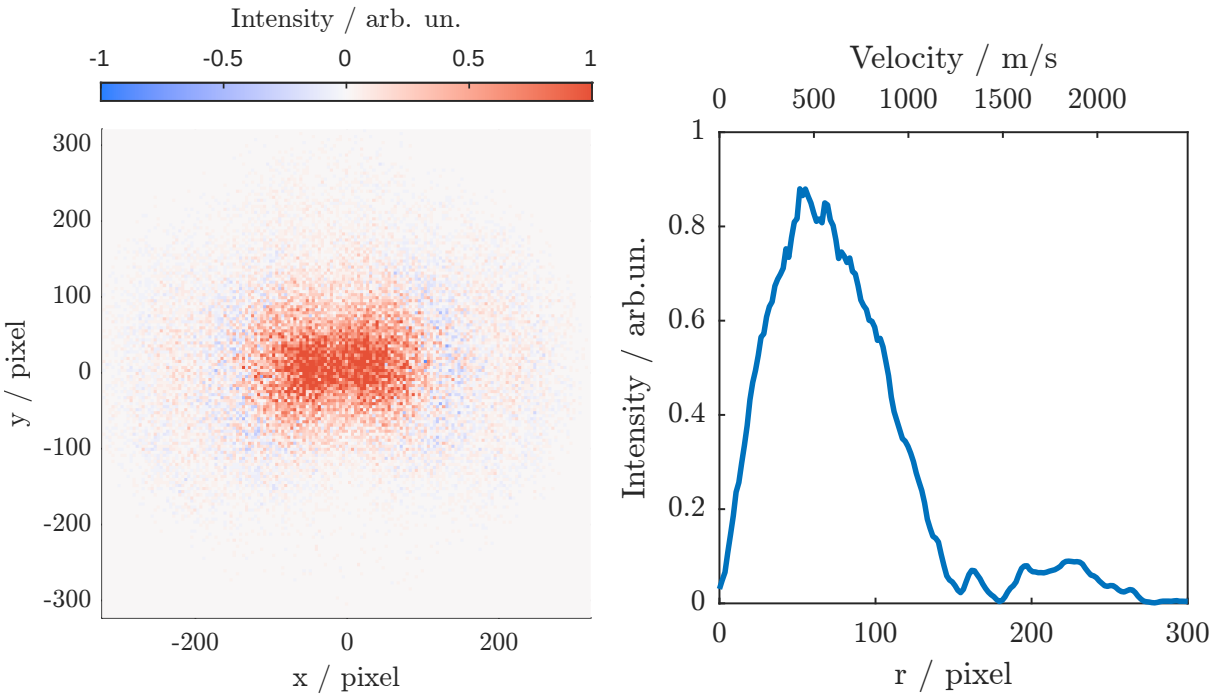


(a) 2d velocity map image

(b) Radial distributions

Figure 6.2: 2d velocity map image and radial distribution of $I^+$ ions generated by Coulomb explosion of effusive $I_2$ molecules in the B-state.

## 6.3 B state electrons

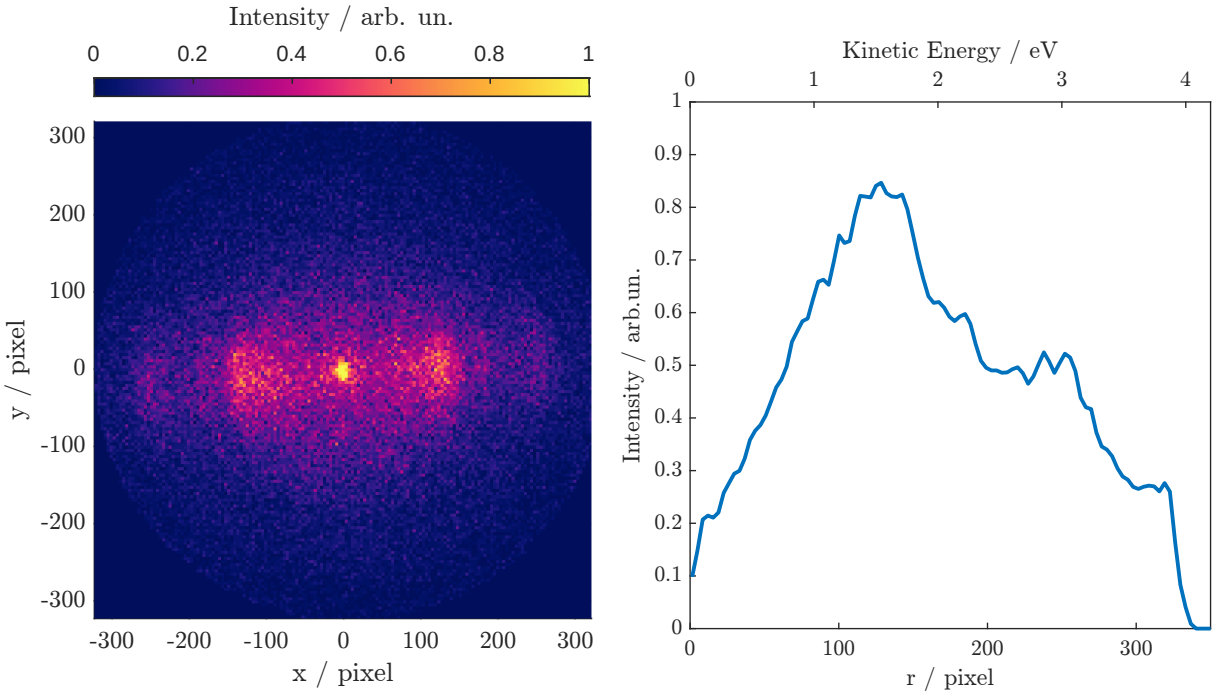


(a) 2d velocity map image

(b) Radial distribution

Figure 6.3: 2d velocity map image and radial distribution of electrons generated by ionization of effusive $I_2$ with the 800 nm probe puls

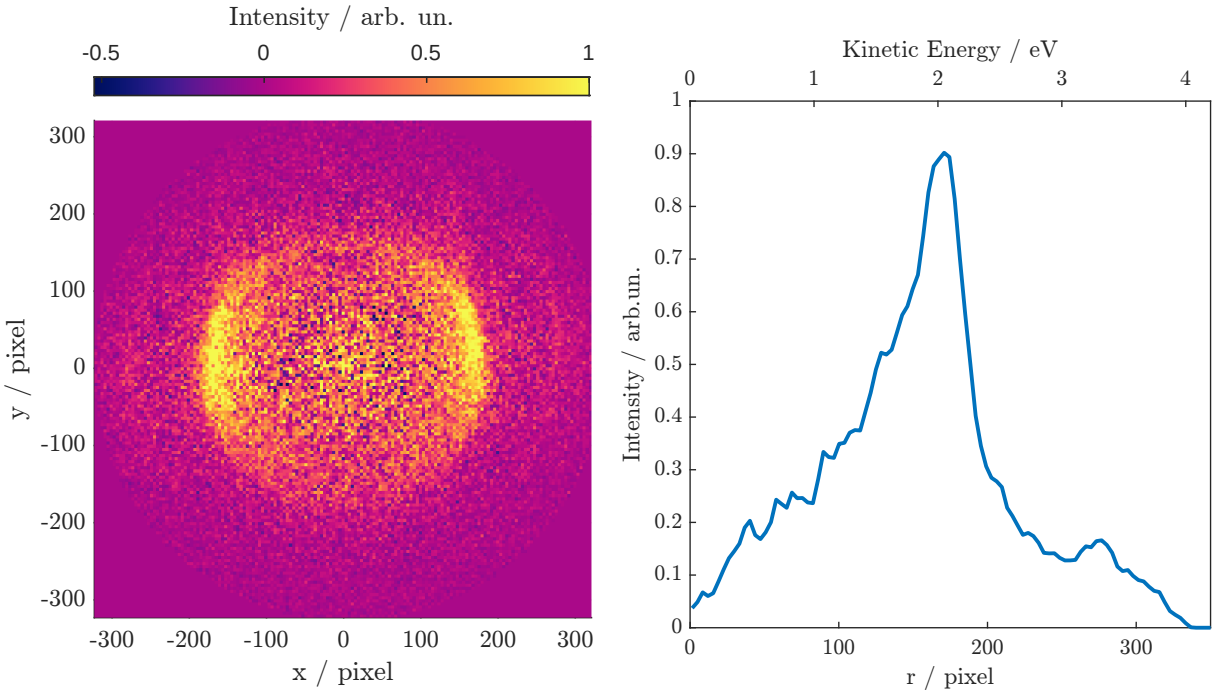


(a) 2d velocity map image

(b) Radial distribution

Figure 6.4: 2d velocity map image and radial distribution of electrons generated by ionization of effusive $I_2$ in the B-state with 600 nm pump

## 6.4 VMI goldplating

The VMI copper electrodes were goldplated with an electroless goldplating solution, to increase the workfunction and thus to lower the noise generated by electrons produced by photons hitting the surface.

The gold-plating was done in three steps:

1. 15 min ultrasonic cleaning in acetone
2. 15 min ultrasonic cleaning in Sodosil alkaline cleaner (sigma - aldrich)
3. 10 min bright electroless gold plating solution in a water bath at 70-80 degrees

Figure 6.5 shows before and after images of the electrodes.

(a) Copper plate before

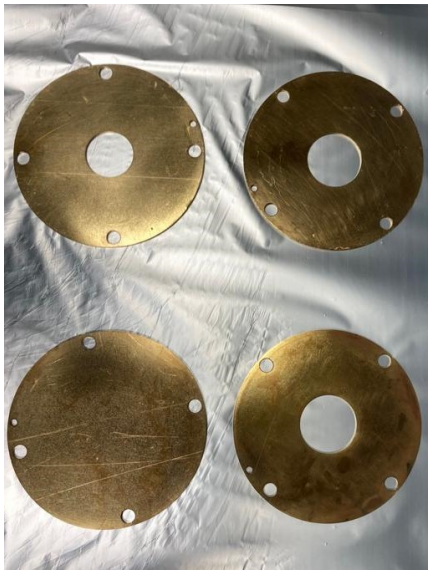

(b) After gold-plating

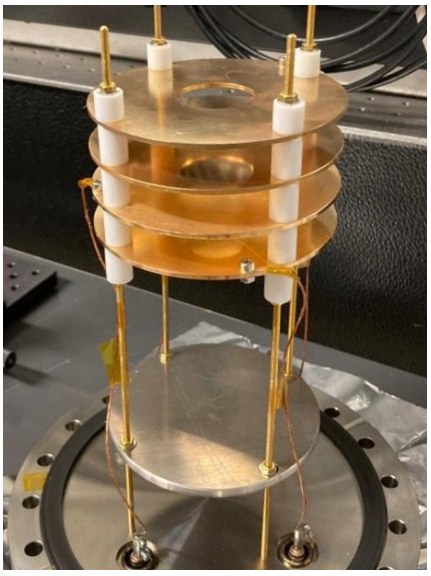

(c) Final setup

Figure 6.5: Goldplating of VMI copper electrodes

# Bibliography


[1] K. K. Rohatgi-Mukherjee. *Fundamentals of Photochemistry*. New Age International, 1978.

[2] Ahmed H. Zewail. "Femtochemistry: Atomic-Scale Dynamics of the Chemical Bond". In: *The Journal of Physical Chemistry A* 104.24 (May 2000), pp. 5660–5694. DOI: 10.1021/jp001460h.

[3] Tyler L. Cocker et al. "An ultrafast terahertz scanning tunnelling microscope". In: *Nature Photonics* 7.8 (July 2013), pp. 620–625. DOI: 10.1038/nphoton.2013.151.

[4] J. Itatani et al. "Tomographic imaging of molecular orbitals". In: *Nature* 432.7019 (Dec. 2004), pp. 867–871. DOI: 10.1038/nature03183.

[5] J.P. Toennies and A.F. Vilesov. "Superfluid helium droplets: A uniquely cold nanomatrix for molecules and molecular complexes". English. In: *Angewandte Chemie - International Edition* 43.20 (2004), pp. 2622–2648. ISSN: 1433-7851. DOI: 10.1002/anie.200300611.

[6] Bernhard Thaler et al. "Femtosecond photoexcitation dynamics inside a quantum solvent". In: *Nature Communications* 9.1 (Oct. 2018). DOI: 10.1038/s41467-018-06413-9.

[7] Bernhard Thaler et al. "Long-Lived Nuclear Coherences inside Helium Nanodroplets". In: *Physical Review Letters* 124.11 (Mar. 2020), p. 115301. DOI: 10.1103/physrevlett.124.115301.

[8] Alkwin Slenzcka ; Jan Peter Toennies, ed. *Molecules in Superfluid Helium Nanodroplets*. Springer International Publishing, May 2022. 600 pp. ISBN: 3030948951. URL: https://www.ebook.de/de/product/41965032/molecules_in_superfluid_helium_nanodroplets.html.

[9] Anna Gutberlet et al. "Aggregation-Induced Dissociation of $HCl(H_2O)_4$". In: *Science* 324.5934 (June 2009), pp. 1545–1548. DOI: 10.1126/science.1171753.

[10] R.M. Bowman, M. Dantus, and A.H. Zewail. "Reprint of: Femtosecond transition-state spectroscopy of iodine: From strongly bound to repulsive surface dynamics". In: *Chemical Physics Letters* 589 (Dec. 2013), pp. 42–45. DOI: 10.1016/j.cplett.2013.08.065.

[11] H.P.Broida K.Sakurai G.Capelle. "Measurements of Lifetimes and Quenching Cross Sections of the B State of Iodine Using a Tunable Dye Laser". In: *The Journal of Chemical Physics* (1970).

[12] M. Ben-Nun et al. "Prompt solvent-induced electronic predissociation of femtosecond pumped iodine. A computational study". In: *Chemical Physics Letters* 245.6 (Nov. 1995), pp. 629–638. DOI: 10.1016/0009-2614(95)01064-g.

[13] R. Zadoyan et al. "Predissociation dynamics of I2„B... in liquid CCl4 observed through femtosecond pump-probe measurements: Electronic caging through solvent symmetry". In: (1997).

[14] Christoph Lienau and Ahmed H. Zewail. "Solvation Ultrafast Dynamics of Reactions. 11. Dissociation and Caging Dynamics in the Gas-to-Liquid Transition Region". In: *The Journal of Physical Chemistry* 100.48 (Jan. 1996), pp. 18629–18649. DOI: 10.1021/jp962430a.

[15] Michael N. R. Ashfold et al. "Imaging the dynamics of gas phase reactions". In: *Phys. Chem. Chem. Phys.* 8.1 (2006), pp. 26–53. DOI: 10.1039/b509304j.

[16] F. Légaré et al. "Laser Coulomb-explosion imaging of small molecules". In: *Physical Review A* 71.1 (Jan. 2005), p. 013415. DOI: 10.1103/physreva.71.013415.

[17] M. Broyer, J.-C. Lehmann, and J. Vigue. "g Factors and lifetimes in the B state of molecular iodine". In: *Journal de Physique* 36.3 (1975), pp. 235–241. DOI: 10.1051/jphys:01975003603023500.

[18] J.E. Selwyn and J.I. Steinfeld. "Collision-induced predissociation by van der Waals' interaction". In: *Chemical Physics Letters* 4.4 (Nov. 1969), pp. 217–220. DOI: 10.1016/0009-2614(69)80106-5.

[19] Arnau Vilà, Miguel González, and Ricardo Mayol. "Quantum interferences in the photodissociation of $Cl_2$(B) in superfluid helium nanodroplets ($^4He_N$)". In: *Physical Chemistry Chemical Physics* 17.48 (2015), pp. 32241–32250. DOI: 10.1039/c5cp03575a.

[20] Arnau Vilà and Miguel González. "Quantum dynamics of the $Br_2$(B-excited state) photodissociation in superfluid helium nanodroplets: importance of the recombination process". In: *Physical Chemistry Chemical Physics* 24.39 (2022), pp. 24353–24361. DOI: 10.1039/d2cp02984g.

[21] L R Khundkar and A H Zewail. "Ultrafast Molecular Reaction Dynamics in Real-Time: Progress Over a Decade". In: *Annual Review of Physical Chemistry* 41.1 (Oct. 1990), pp. 15–60. DOI: 10.1146/annurev.pc.41.100190.000311.

[22] Sergey Lukashov, Alexander Petrov, and Anatoly Pravilov. *The Iodine Molecule*. Springer International Publishing, 2018. DOI: 10.1007/978-3-319-70072-4.

[23] Lars Christiansen. "Laser Induced Alignment of MoleculesEmbedded in Helium Droplets:Exploration and Potential Applications". PhD thesis. Aarhus University, 2015.

[24] A. Garcia-Vela, P. Villarreal, and G. Delgado-Barrio. "Structure and dynamics of small $I_2$...$He_N$ van der Waals clusters (n=1-9)". In: *The Journal of Chemical Physics* 92.11 (June 1990), pp. 6504–6513. DOI: 10.1063/1.458285.

[25] D.M. Willberg et al. "A simple description of vibrational predissociation by a full-collision approach". In: *Chemical Physics Letters* 201.5-6 (Jan. 1993), pp. 506–512. DOI: 10.1016/0009-2614(93)85109-2.

[26] D. M. Willberg et al. "Real-time dynamics of clusters. I. $I_2X_n(n = 1)$". In: *The Journal of Chemical Physics* 96.1 (Jan. 1992), pp. 198–212. DOI: 10.1063/1.462499.

[27] M. Gutmann, D. M. Willberg, and A. H. Zewail. "Real-time dynamics of clusters. II. $I_2X_n(n = 1; X = He, Ne,$ and $H_2)$, picosecond fragmentation". In: *The Journal of Chemical Physics* 97.11 (Dec. 1992), pp. 8037–8047. DOI: 10.1063/1.463426.

[28] M. Gutmann, D. M. Willberg, and A. H. Zewail. "Real-time dynamics of clusters. III. $I_2Ne_n(n = 2-4)$, picosecond fragmentation, and evaporation". In: *The Journal of Chemical Physics* 97.11 (Dec. 1992), pp. 8048–8059. DOI: 10.1063/1.463427.

[29] Andreas Rohrbacher, Nadine Halberstadt, and Kenneth C. Janda. "The Dynamics of Noble Gas—Halogen Molecules and Clusters". In: *Annual Review of Physical Chemistry* 51.1 (Oct. 2000), pp. 405–433. DOI: 10.1146/annurev.physchem.51.1.405.

[30] Jae Hyuk Lee et al. "Filming the Birth of Molecules and Accompanying Solvent Rearrangement". In: *Journal of the American Chemical Society* 135.8 (Feb. 2013), pp. 3255–3261. DOI: 10.1021/ja312513w.

[31] Qianli Liu, Juen-Kai Wang, and Ahmed H. Zewail. "Femtosecond dynamics of dissociation and recombination in solvent cages". In: *Nature* 364.6436 (July 1993), pp. 427–430. DOI: 10.1038/364427a0.

[32] Pavel V Zasimov et al. "Radiation-induced chemistry in the C2H2–H2O system at cryogenic temperatures: a matrix isolation study". In: *Monthly Notices of the Royal Astronomical Society* (Nov. 2019). DOI: 10.1093/mnras/stz3228.

[33] Michael Stadlhofer. "Femtosecond Photodynamics of MagnesiumMolecules and Clusters inside Helium Nanodroplets". MA thesis. Graz University of Technology, 2020.

[34] Kerstin Absenger. "Coherent Nuclear Wave PacketDynamics of Aluminum Dimers insideSuperfluid Helium Nanodroplets". MA thesis. Graz University of Technology, 2021.

[35] Bernhard Thaler. "Ultrafast Photoinduced Dynamics of Atoms and Dimer Moleculesinside Helium Nanodroplets". PhD thesis. Graz University of Technology, 2020.

[36] Matthias Hartmann et al. “High resolution infrared spectroscopy of single SF6 molecules in helium droplets. I. Size effects in 4He droplets”. In: *The Journal of Chemical Physics* 110.11 (Mar. 1999), pp. 5109–5123. DOI: 10.1063/1.479111.

[37] Jan Harms, J. Peter Toennies, and Franco Dalfovo. “Density of superfluid helium droplets”. In: *Physical Review B* 58.6 (Aug. 1998), pp. 3341–3350. DOI: 10.1103/physrevb.58.3341.

[38] Jan Harms et al. “Experimental and theoretical study of the radial density distributions of large $^3$He droplets”. In: *Physical Review B* 63.18 (Apr. 2001). DOI: 10.1103/physrevb.63.184513.

[39] Florian Lackner. “Rydberg States of Alkali-Metal Atoms on Superfuid Helium Nanodroplets”. PhD thesis. Graz University of Technology, 2012.

[40] André T. J. B. Eppink and David H. Parker. “Velocity map imaging of ions and electrons using electrostatic lenses: Application in photoelectron and photofragment ion imaging of molecular oxygen”. In: *Review of Scientific Instruments* 68.9 (Sept. 1997), pp. 3477–3484. DOI: 10.1063/1.1148310.

[41] Lutz Fechner. “Aufbau eines Velocity-Map-Imaging-Spektrometers und winkelaufgelöste Spektroskopie an Rubidium-dotierten Helium-Nanotröpfchen”. MA thesis. Albert-Ludwigs-Universität Freiburg, 2011.

[42] A. I. Chichinin et al. “Imaging chemical reactions – 3D velocity mapping”. In: *International Reviews in Physical Chemistry* 28.4 (Oct. 2009), pp. 607–680. DOI: 10.1080/01442350903235045.

[43] Paul Maierhofer et al. “Disentangling Multichannel Photodissociation Dynamics in Acetone by Time-Resolved Photoelectron–Photoion Coincidence Spectroscopy”. In: *The Journal of Physical Chemistry A* 120.32 (Aug. 2016), pp. 6418–6423. DOI: 10.1021/acs.jpca.6b07238.

[44] Yuki Kobayashi et al. “Direct mapping of curve-crossing dynamics in IBr by attosecond transient absorption spectroscopy”. In: *Science* 365.6448 (July 2019), pp. 79–83. DOI: 10.1126/science.aax0076.

# List of Figures


1.1 Relevant Electronic potentials of $I_2$ [22],[23] and schematic representation of a pump-probe experiment during predissociation. Possible process channel: A pump pulse excites the molecule from the ground state X to the excited bound state B, where a vibrational wavepacket (WP) evolves - and couples to the dissociative state a' which leads to predissociation of the molecule. After a time delay a second laser pulse (probe) ionizes the iodine atoms. Also shown are the weakly bound state A, the dissociative state a, and two ionic states. . . . . 12

1.2 Femtosecond transition-state transients of $I_2$ in gas phase. Top: Pump wavelength 620 nm and probe wavelength 310 nm, showing oscillations on a large timescale with visible decay of the envelope. Bottom: pump wavelength 620 nm and probe wavelength 390 nm, smaller timescale depicting the individual WP oscillations with a period of 300 fs. [10] . . . . . 14

1.3 Laser induced fluorescence signal for excitation below (top and center) and above (bottom) the dissociation limit of the iodine B-state. Insets show measurements of effusive iodine, image taken from [31]. . . . . 16

1.4 Different properties of helium nanodropelets droplets formed by jet expansion. Depending on the nozzle temperature different regimes form, influencing size and properties of the droplets. [5] . . . . . 17

1.5 **a** In-$He_N$ PES as function of the bubble radius and pump (violet) probe (blue) scheme depicted schematically. **b** DFT calculations for an In atom inside a $He_{4000}$ droplet showing density distributions for different times. [6] . . . . . 18

1.6 **a** Dynamics of $In_2$ in He nanodroplets - bubble expansion and dopant ejection, **b** Schematic of the PES showing a wavepacket motion of $In_2$ after photoexitation and subsequent ionization. Image taken from [7] . . . . . 19

1.7 Time-of-flight pump-probe measurement of $I_2$ in the gas phase, 600 nm excitation into the B-state. Photoelectron signal and kinetic energy depending on pump-probe time-delay. Surface plot (top) shows the energy of PEs over a time delay, and the colorbar indicates PE yield. The bottom shows signals integrated over all energies, oscillation duration of 300 fs. . . . . 20

1.8 Time-of-flight pump-probe measurement of $I_2$ in the gas phase, 600 nm excitation into the B-state. Comparison of PE yield of effusive iodine (orange) with iodine solvated in $He_N$ (blue) as a function of pump-probe time-delay $\Delta t$. . . . . 21

2.1 Optical Setup of Femtolab, the Legend laser system gives pulses of 25 fs with a wavelength of 800 nm. The beam is split in two, both pump and probe receive further manipulation before entering the vacuum chamber. Image adapted from [33] . . . . . 23

2.2 Laser beam foci with Gaussian fits as measured on *ARTCAM-UV-WOM CMOS Camera*, pixels have been calculated to $\mu$m (1 px = 10 $\mu$m ). For the FWHM values see table 2.1 . . . . . 25

2.3 Laser spectra of 600 nm and 690 nm pump beam after the OPA . . . . . 26

2.4 Spectrum of fundamental 800 nm Legend output (probe beam) . . . . . 26

2.5 Complete Vacuum setup consisting of source chamber, pickup chamber and main chamber [35]. Differential pumping stage (DPS) . . . . . 27

2.6 Experimental data on mean droplet sizes of superfluid helium nanodroplets generated by supersonic expansion depending on source Temperature $T_0$ for different He pressures. [5, 36, 37, 38] Image taken from [39]. . . . . 28
2.7 Schematic representation of the VMI detection system, an electrostatic lens composed of repelled, extractor and two ground electrodes focuses charged particles on a MCP . . . . . 28
2.8 Simion simulation of the electrostatic fields forming around the VMI electrodes, equipotential lines in green and particle trajectories in red, image taken from Lutz Fechner's master thesis [41] . . . . . 29
2.9 3D drawing of the velocity map imaging (VMI) detection system, as developed by Bernhard Thaler and Leonhard Treiber - credits to Michael Stadlhofer for drawing. An electrostatic lens composed of repeller, extractor, and two ground electrodes focuses charged particles on a MCP, spatially confided electron avalanches then induce fluorescence on a phosphor screen which is read out by a CCD camera. . . 30
2.10 Voltage output of the high-speed switch connected to the MCP front to gate on specific masses . . . . . 31
2.11 Dark count measurement, without a laser present in the chamber and the voltages at repeller and extractor turned off. Counts on the phosphor screen read out by the camera depending on MCP back voltage for phosphor voltages of 4.2 kV, 4.1 kV, and 4.0 kV. MCP front at -800 V. . . . . 32
2.12 Hit size distributions of $I^+$ ions generated by multiphoton ionization of $I_2$ molecules in the gas phase. Sizes depending on MCP back voltage and phosphor voltage with MCP front gated at -800 V on the $I^+$ mass . . . . . 32
2.13 Velocity map image and radial distribution of $I^+$ ions generated by multiphoton ionization of effusive $I_2$ VMI molecules by the 800 nm probe pulse . . . . . 33
2.14 Radial probe-only velocity plot for different probe power and logarithmic power dependence (b) of Coulomb peak (r>215px) compared to the rest of the signal (r>215 px) . . . . . 34
2.15 Schematic of the 2D projection $F(r')$ from an initial 3D distribution $f(r)$ (Abel inversion) . . . . . 35
2.16 Comparison of Abel transformed and raw data of $I^+$ ions generated by photodissociation of effusive $I_2$ moleculs with the 800 nm probe pulse . . . . . 36
2.17 Abel transformed 2d image and radial distribution of electrons generated by ionization of effusive $I_2$ with the 800 nm probe pulse. Arrow indicates linewidth (resolution) . . . . . 37
2.18 Image of ions generated by the 800 nm probe beam taken with the VMI with 0 V extractor voltage (no focusing) for different laser polarization. This is done to center the beam in the spectrometer. . . . . 38
2.19 Schematic of the helium droplet beam and effusive molecule beam in the vacuum chamber. The probe beam focus needs to be set in the center of the helium droplet beam to maximize the signal originating from inside helium nanodroplets . . . . 39
2.20 2D image of ions generated by photodissociation of effusive $I_2$ molecules with the 800 nm probe beam, comparison of focused and unfocused electrodes. The sharp line generated by ionization from the effusive molecular beam serves as an indication of the right voltage, a wrong ratio of repeller to extractor voltage will result in a distorted image (right) . . . . . 39
2.21 2D image of ions generated by photodissociation of $I_2$ molecules inside helium nanodroplets with the 800 nm probe beam. The laser polarization needs to be in the detector plane (left) to measure a conclusive velocity distribution, otherwise this results in a 2D-Gaussian distribution (right) . . . . . 40

2.22 ToF detection of pump-probe generated ions of $I_2$ at 690 nm pump wavelength for effusive molecules and molecules solvated in helium nanodroplets with varying time-delay between pump and probe pulse . . . . . 41
2.23 ToF detection of pump-probe generated ions of $I_2$ at 600 nm pump wavelength for effusive molecules and molecules solvated in helium nanodroplets with varying time-delay between pump and probe pulse . . . . . 42
2.24 ToF detection of 600 nm pump 800 nm probe generated ions from effusive $I_2$ molecules, delay scan over the whole stage showing the stability of the B-state . . 42

3.1 2D velocity map images of $I^+$ ions generated by photodissociation followed by probe pulse ionization of effusive $I_2$ molecules via the A-state with varying time delay from 1-300 ps . . . . . 44
3.2 Radial distributions of $I^+$ ions generated by photodissociation followed by probe puls ionization of effusive $I_2$ molecules via the A-state with varying time delay between pump and probe from 5-300 ps . . . . . 45
3.3 Mean velocity map image and radial distribution of $I^+$ ions generated by photodissociation followed by probe pulse ionization of effusive $I_2$ molecules via the A-state. Comparison with scaled and inverted probe only ground state ionization and addition of scaled-probe only . . . . . 45
3.4 Abel transformed 2d velocity map image and radial distribution of $I^+$ ions generated by photodissociation followed by probe pulse ionization of effusive $I_2$ molecules via the A-state . . . . . 46
3.5 2D image of $I^+$ ions generated by photodissociation followed by probe pulse ionization of effusive $I_2$ molecules via the A-state, 680 nm pump pulse 2.6 ns before the 800 nm probe pulse. Image taken from Lars Christiansen's dissertation [23] . 46
3.6 Abel transform 2d velocity map image and radial distribution of $I^+$ ions generated by Coulomb explosion followed by probe pulse ionization of effusive $I_2$ molecules in the B-state, radial distribution compared with ground state Coulomb explosion (probe only) . . . . . 47
3.7 Abel transformed 2d velocity map image and radial distribution of electrons generated by ionization of effusive $I_2$ in the B-state with 600 nm pump . . . . . 48
3.8 2D velocity map images of $I^+$ ions generated by photodissociation followed by probe pulse ionization of $I_2$ molecules inside helium nanodroplets via the A-state with varying time delay from 5-300 ps . . . . . 50
3.9 Radial distributions of $I^+$ ions generated by photodissociation followed by probe pulse ionization of $I_2$ molecules inside helium nanodroplets via the A-state with a varying time delay from 5-300 ps. Comparison with mean scaled and inverted probe only ground state ionization. . . . . 51
3.10 Most probable (mode) and mean escape velocity $E(v)$ of the ions generated by A-state photodissociation inside helium droplets . . . . . 51
3.11 2D velocity map images of $I^+$ ions generated by predissociation followed by probe pulse ionization of $I_2$ molecules inside helium nanodroplets via the B-state with a varying time delay from 10-300 ps. Addition of scaled probe only contribution . . 52
3.12 Radial distributions of $I^+$ ions generated by predissociation followed by probe pulse ionization of $I_2$ molecules inside helium nanodroplets via the B-state with a varying time delay from 10-300 ps. Comparison with mean scaled and inverted probe only ground state ionization. . . . . 53
3.13 Most probable (mode) and mean velocity $E(v)$ of the ions generated by B-state predissociation inside droplets . . . . . 53
3.14 Comparison of A-state photodissociation of $I_2$ molecules in gas phase (yellow) and inside helium nanodroplets with three different time-delays (10,50 and 300 ps) between pump and probe pulse . . . . . 54

3.15 Comparison of A-state (300 ps time delay) photodissociation and B-state (200 ps time delay) predissociation of $I_2$ molecules inside helium nanodroplets . . . . . 55

6.1 QMS mass table, time dependence of QMS current signals for relevant atomic masses during several measurements. Fast signal drop and increase is a result of closing and opening the valve to the source chamber (blocked or passing through helium beam) . . . . . 63
6.2 2d velocity map image and radial distribution of $I^+$ ions generated by Coulomb explosion of effusive $I_2$ molecules in the B-state. . . . . 64
6.3 2d velocity map image and radial distribution of electrons generated by ionization of effusive $I_2$ with the 800 nm probe puls . . . . . 65
6.4 2d velocity map image and radial distribution of electrons generated by ionization of effusive $I_2$ in the B-state with 600 nm pump . . . . . 66
6.5 Goldplating of VMI copper electrodes . . . . . 67

# List of Tables

2.1 FWHMs of the Gaussian fits for pump and probe pulse, each with two different lenses with focal lengths f and the calculated peak intensity $I$ for a pump laser power of 150 mW and a probe laser power of 500 mW (repetition rate 3000 Hz) . 25
2.2 VMI voltages depending on operation mode . . . . . 37

# Danksagung

An dieser Stelle möchte ich allen danken die mich während meines Studiums und beim Schreiben dieser Arbeit direkt und indirekt unterstützt haben. Allen voran der Betreuer meiner Arbeit Ass. Prof. Dipl.-Ing. Dr.techn. Markus Koch, der mir überhaupt die Möglichkeit geboten hat in seiner Arbeitsgruppe spannende Grundlagenforschung zu betreiben und einen Einblick in dieses interessante Themengebiet zu bekommen. Regelmäßige Diskussionen und seine Unterstützung bei jeglichen Problemen haben das Arbeiten wirklich angenehm und lehrreich gemacht. Seine Motivation für Wissenschaft ist mitreißend und hat mich auch immer aufs Neue für grundlegende Physik begeistert.

Am meisten praktische Unterstützung habe ich definitiv von Michael Stadlhofer bekommen, der mir einerseits sehr viel beigebracht hat und versucht hat alle aufkommenden Fragen zu beantworten, und andererseits als Freund den Arbeitsalltag viel abwechslungsreicher gemacht hat. Gespräche (und auch die eine oder andere Partie Schach) während den Messungen hat auf jeden Fall eine zwischenzeitliche Langeweile überbrückt. Er hat während unseren unzähligen Stunden im Labor immer für eine freundliche und entspannte Atmosphäre gesorgt, was definitiv keine einfache Aufgabe ist. Hier auch ein Dank an alle anderen Kollegen, Christian, Simon, Robert, Maximilian und Florian mit denen tratschen in der Kaffeepause immer wieder lustige Unterhaltungen zustande gebracht hat. Das Arbeitsklima in der Gruppe war einfach super, gemeinsam zu kochen und Stickstoff-Eis zu essen hat immer dazu beigetragen den Alltag aufzulockern.

Ich danke selbstverständlich auch meinen Eltern, die mich während des gesamten Studiums in jeder Weise unterstützt haben. Nicht nur finanziell, sondern auch moralisch waren sie immer eine Stütze und haben mir immer ermöglicht meinen Weg ohne Druck und selbstständig zu gehen. Gleichweise auch Dank an alle meine Freunde, insbesondere meinen Studienkollegen die meine Entscheidung Physik zu studieren im Nachhinein oft bekräftigt haben - alleine schon durch die geschlossenen Freundschaften. Sich gemeinsam durch Lehrveranstaltungen durchzukämpfen, schweißt hier sehr zusammen.

Zuallerletzt ein Danke an dich, Elena, du hast bestimmt am meisten Jammern und Klagen abbekommen, wenn mal etwas nicht so funktioniert hat wie ich es mir vorgestellt habe. Nichtsdestotrotz warst du immer an meiner Seite und hast mir geholfen auch schwierige Zeiten zu überwinden.